



## City Research Online

### City, University of London Institutional Repository

---

**Citation:** Rahman, M. E. (2015). Integrated full vectorial FEM, FDTD and diffraction integrals in characterising visible light propagation through lossy biological media. (Unpublished Doctoral thesis, City, University of London)

This is the accepted version of the paper.

This version of the publication may differ from the final published version.

---

**Permanent repository link:** <https://openaccess.city.ac.uk/id/eprint/15935/>

**Link to published version:**

**Copyright:** City Research Online aims to make research outputs of City, University of London available to a wider audience. Copyright and Moral Rights remain with the author(s) and/or copyright holders. URLs from City Research Online may be freely distributed and linked to.

**Reuse:** Copies of full items can be used for personal research or study, educational, or not-for-profit purposes without prior permission or charge. Provided that the authors, title and full bibliographic details are credited, a hyperlink and/or URL is given for the original metadata page and the content is not changed in any way.

**Integrated Full Vectorial FEM,  
FDTD and Diffraction Integrals  
in Characterising Visible Light  
Propagation Through Lossy  
Biological Media**



M. Enayetur Rahman

School of Mathematics, Computer Science and Engineering

City University London

A thesis submitted for the degree of

*Doctor of Philosophy*

October, 2015

---

I would like to dedicate this thesis to my loving wife.

## **Acknowledgements**

First I would like to thank the Almighty Allah for giving me the courage and patience to carry out and complete this work.

I would like to thank my thesis supervisor Prof. B.M.A. Rahman for his endless support and encouragement throughout the course of this research. His guidance and patience had been giving me inspirations to pass through the most difficult times. I would also like to thank my thesis co-supervisor Prof. K.T.V. Grattan for his support throughout.

I am also indebted to my family members, especially my wife and mother for understanding the difficult situations and providing me with their warm supports.

I would like to give thanks to Dr. Arti Agrawal and Dr. Kejalakshmy for their support in the research by explaining the difficult topics of Photonics in great details. I would also like to thank the members of the Photonic Modelling Group, City University London, for providing a very good and warm working atmosphere. Special Thanks to Dr. Raiyan Kabir, with whom the endless and fruitful discussions had made overcoming numerous technical difficulties and riddles easier. On several occasions discussions with Surendra Hada, Dr. Isuru, Rezaul Karim, Moseur Rahman helped to solve different problems.

I would also like to thank City University London for providing the infrastructure and supports.

## **Declarations**

The City University London Librarian is hereby granted powers of discretion to allow this thesis to be copied in whole or in part without further reference to the author. This permission is only for single copies made for the purposes of study and subject to the normal conditions of acknowledgement.

## Abstract

In this thesis, the propagation characteristics of the biological optical waveguides, considering the materials as lossy in the optical frequencies, have been analysed. It has been found that the losses present in the biological materials in optical frequencies are not negligible, and the loss values have significant effects on the propagation characteristics of these waveguides.

In biological optical waveguides, each waveguide is surrounded by parallel waveguides so that the propagation characteristics would be different from that of single waveguide present in a homogeneous material. In this thesis, the impacts of the presence of the neighbouring waveguides on the propagation characteristics of a waveguide are studied in details.

Dispersion characteristics of the waveguides have been investigated, and the effects of the material loss, presence of the neighbouring waveguides and the presence of multi-layer W-fibre like structure on the dispersion characteristics have also been studied.

The modal characteristics, the time-domain evolution of the signal and the diffraction characteristics have been integrated to explain some of the still unanswered questions in the visual systems. An attempt has been made to explain the Stiles-Crawford effect of human retina in light of the findings of this thesis.

A full-vectorial  $\mathbf{H}$ -field based finite element method (FEM) is used for the modal solutions, Finite Difference Time Domain (FDTD) is used to study the time evolution of the signals through the waveguides, and the Diffraction profiles have been obtained by Rayleigh-Sommerfeld (RS) diffraction integral.

# Contents

|   |            |
|---|------------|
| <b>Contents</b>   | <b>v</b>   |
| <b>List of Figures</b>                                    | <b>ix</b>  |
| <b>List of Tables</b>                                     | <b>xiv</b> |
| <b>1 Introduction</b>                                     | <b>1</b>   |
| 1.1 Background . . . . .                                  | 3          |
| 1.1.1 Insect eye - Compound eye . . . . .                 | 3          |
| 1.1.2 Absorbing surroundings of the Rhabdom . . . . .     | 5          |
| 1.1.3 Mammal eye . . . . .                                | 5          |
| 1.1.4 Lossy surroundings of the Glial cells . . . . .     | 8          |
| 1.1.5 Diffraction in the visual systems . . . . .         | 8          |
| 1.1.6 Challenges in modelling biological tissue . . . . . | 10         |
| 1.1.7 Mathematical treatments for lossy medium . . . . .  | 12         |
| 1.1.8 Importance of the structure . . . . .               | 12         |
| 1.1.9 Previous studies on these structures . . . . .      | 13         |
| 1.2 Overlooked problems . . . . .                         | 14         |
| 1.2.1 Presence of biological optical waveguide . . . . .  | 14         |
| 1.2.2 Impacts of lossy surroundings . . . . .             | 16         |
| 1.2.3 Impacts of neighbouring structures . . . . .        | 16         |
| 1.2.4 W-fibre structure in insect rhabdom . . . . .       | 16         |
| 1.2.5 Limitations of RAY optics based models . . . . .    | 16         |
| 1.2.6 Point source position and excited modes . . . . .   | 17         |
| 1.3 Aim of the Thesis . . . . .                           | 17         |

## CONTENTS

---

|          |   |           |
|----------|---|-----------|
| 1.4      | Tools Available . . . . .                             | 18        |
| 1.4.1    | Analytical solution . . . . .                         | 18        |
| 1.4.2    | Ray Optics . . . . .                                  | 18        |
| 1.4.3    | Numerical solutions of Maxwell's equations . . . . .  | 19        |
| 1.4.3.1  | Finite Difference based modal solutions . . . . .     | 19        |
| 1.4.3.2  | FEM based modal solutions . . . . .                   | 19        |
| 1.4.3.3  | BPM . . . . .   | 19        |
| 1.4.3.4  | FETD . . . . .  | 21        |
| 1.4.3.5  | FDTD . . . . .  | 22        |
| 1.5      | Methodology and Study steps . . . . .                 | 22        |
| 1.5.1    | Planar structure . . . . .                            | 23        |
| 1.5.2    | 3D structures . . . . .                               | 23        |
| 1.5.3    | Test cases . . . . .                                  | 24        |
| 1.5.3.1  | Drosophila Melanogaster (Fruit fly) Compound Eye      | 24        |
| 1.5.3.2  | Glial cells of Human Retina . . . . .                 | 24        |
| 1.5.3.3  | Integrated Diffraction integral and Modal solutions   | 25        |
| 1.6      | Thesis organization . . . . .                         | 26        |
| <b>2</b> | <b>Simulation Environment</b>                         | <b>27</b> |
| 2.1      | Maxwell's Equations . . . . .                         | 27        |
| 2.1.1    | Variational Formulation . . . . .                     | 31        |
| 2.1.2    | Scalar Approximation . . . . .                        | 31        |
| 2.1.3    | Vector Formulation . . . . .                          | 31        |
| 2.1.4    | Natural Boundary Condition . . . . .                  | 33        |
| 2.2      | Numerical Solution of Maxwell's equation . . . . .    | 33        |
| 2.2.1    | Finite Element Method (FEM) . . . . .                 | 33        |
| 2.2.1.1  | Discretisation . . . . .                              | 34        |
| 2.2.1.2  | Shape Function . . . . .                              | 35        |
| 2.2.1.3  | Global and Element Matrices . . . . .                 | 39        |
| 2.2.1.4  | Spurious Solution . . . . .                           | 42        |
| 2.2.2    | Finite Difference Time Domain Method (FDTD) . . . . . | 42        |
| 2.2.3    | FDTD algorithm . . . . .                              | 44        |
| 2.2.4    | Numerical Stability . . . . .                         | 50        |

|          |  |           |
|----------|--|-----------|
| 2.3      | Perfectly Matched Layer (PML) . . . . .  | 50        |
| 2.3.1    | Uniaxial PML Implementation . . . . .  | 53        |
| 2.4      | Diffraction . . . . .  | 54        |
| 2.4.1    | Kirchoff’s Diffraction Integral . . . . .  | 54        |
| 2.4.2    | Rayleigh-Somerfeld Diffraction Integral . . . . .  | 56        |
| 2.5      | Summary . . . . .  | 57        |
| <b>3</b> | <b>Simulation of the Visual System</b>   | <b>58</b> |
| 3.1      | Planar Structure . . . . .   | 58        |
| 3.2      | Introducing loss . . . . .   | 68        |
| 3.3      | Importance of Evanescent Fields . . . . .  | 74        |
| 3.4      | Waveguide Loss Calculation . . . . .   | 81        |
| 3.5      | Planar guide as a limiting case of rectangular guide . . . . .                               | 82        |
| 3.6      | Selection of Wavelength Range . . . . .  | 83        |
| 3.7      | Selection of Methods . . . . .   | 84        |
| 3.8      | Rectangular guide . . . . .  | 87        |
| 3.9      | Circular guide . . . . .   | 89        |
| 3.10     | Hexagonal guide . . . . .  | 91        |
| 3.11     | Irregular guide . . . . .  | 93        |
| 3.12     | Comparisons about the mode profiles of waveguides with different<br>cross-sections . . . . . | 96        |
| 3.13     | Summary . . . . .  | 98        |
| <b>4</b> | <b>Results and Discussion</b>  | <b>99</b> |
| 4.1      | Planar Waveguide . . . . .   | 99        |
| 4.2      | Waveguides with Lossy Materials . . . . .  | 100       |
| 4.3      | Waveguide Array . . . . .  | 114       |
| 4.4      | Multi-layer Waveguide Structures . . . . .   | 120       |
| 4.5      | Drosophila Melanogaster Ommatidium . . . . .   | 123       |
| 4.6      | Glial Cells of Human Retina . . . . .  | 129       |
| 4.7      | Stiles-Crawford Effect . . . . .   | 131       |
| 4.8      | Summary . . . . .  | 132       |

## CONTENTS

---

|                            |            |
|----------------------------|------------|
| <b>5 Conclusions</b>       | <b>134</b> |
| 5.1 Future works . . . . . | 138        |
| <b>References</b>          | <b>139</b> |

# List of Figures

|      |  |    |
|------|--|----|
| 1.1  | Image of a Drosophila, source: en.wikipedia.org . . . . .  | 4  |
| 1.2  | Insect Compound Eye Cross-section source: en.wikipedia.org . . . . .   | 4  |
| 1.3  | Ommatidium Cross-section <a href="#">Smith [2013]</a> . . . . .  | 4  |
| 1.4  | A typical Mammal Eye, source: wikimedia commons . . . . .  | 5  |
| 1.5  | Retina Layers and Cross-section <a href="#">Reichenbach et al. [2012]</a> . . . . .  | 6  |
| 1.6  | Photoreceptors in Mammal Retina, source: www.bioteaching.com . . . . .   | 7  |
| 1.7  | Retinal Glial or Muller Cell, Original Drawing by Muller <a href="#">Müller [1851]</a> . . . . .   | 7  |
| 1.8  | Schematics of a single slit diffraction . . . . .  | 8  |
| 1.9  | Diffraction by a Finite Aperture, source: wikipedia . . . . .  | 9  |
| 1.10 | Electron Microscope Image of Biological Tissue, Cells . . . . .  | 10 |
| 1.11 | Optical waveguide . . . . .  | 14 |
| 1.12 | Snell's law . . . . .  | 15 |
| 2.1  | Boundary between two media having refractive indices $n_1$ and $n_2$ ,<br>$\mathbf{n}$ being the unit vector normal to the interface . . . . . | 30 |
| 2.2  | Finite Elements in 2D . . . . .  | 34 |
| 2.3  | FEM discretisation of a 2D domain using triangular elements . . . . .  | 35 |
| 2.4  | Pascal's triangle . . . . .  | 35 |
| 2.5  | Representation of a first order triangular element . . . . .   | 36 |
| 2.6  | Yee's lattice source: wikipedia . . . . .  | 45 |
| 2.7  | Space-time diagram for 1D wave propagation in FDTD, source:<br><a href="#">Taflove and Hagness [2005]</a> . . . . .                            | 46 |
| 2.8  | Structure of a 2D PML . . . . .  | 52 |
| 2.9  | Geometric arrangements for Kirchhoff's diffraction integral . . . . .  | 55 |

## LIST OF FIGURES

---

|  |    |
|--|----|
| 2.10 Geometric arrangements for evaluating RS diffraction formula . . .  | 56 |
| 3.1 Planar Waveguide Schematics . . . . .  | 58 |
| 3.2 Planar Field profiles at XZ plane for TE . . . . .   | 59 |
| 3.3 Propagation angle and the corresponding field profiles . . . . .   | 60 |
| 3.4 Mode angles vs normalised height ( $d/\lambda$ ) of a Planar waveguide,<br>NA = 0.15 . . . . .                           | 64 |
| 3.5 qd/2 vs hd/2 curves for the detrimental equation of planar struc-<br>ture, $d = 2\mu m$ , NA = 0.15 . . . . .            | 67 |
| 3.6 FDTD simulations of the incident angles and the supported modes  | 67 |
| 3.7 Planar Waveguide with lossy cladding . . . . .   | 69 |
| 3.8 Lossy Guide Parameters . . . . .   | 71 |
| 3.9 Confinement factor and Loss vs $\tan \delta$ . . . . .   | 72 |
| 3.10 Field along guide dimension for lossy cladding . . . . .  | 73 |
| 3.11 Field profile for lossy cladding . . . . .  | 73 |
| 3.12 Sinc function plot . . . . .  | 74 |
| 3.13 Point source in single mode guide . . . . .   | 75 |
| 3.14 Point source in a multi-mode guide . . . . .  | 76 |
| 3.15 Plane wave in a multimode guide . . . . .   | 77 |
| 3.16 Plane wave incident at an angle to excite the higher order modes .  | 77 |
| 3.17 Mode input - mode output; multimode . . . . .   | 78 |
| 3.18 Gaussian input - mode output; multimode guide . . . . .   | 79 |
| 3.19 Lossy Mode input - mode output . . . . .  | 80 |
| 3.20 Rectangular guide - mode along dimension; planar guide field along<br>dimension . . . . .                               | 82 |
| 3.21 $n_{eff}$ changes with b/a ratio; NA=0.15, $\lambda = 550$ nm . . . . .   | 82 |
| 3.22 Sun spectra on the Earth surface source: . . . . .  | 83 |
| 3.23 Visible spectrum source: . . . . .  | 84 |
| 3.24 Approximating irregular geometries with FE and FD based methods   | 85 |
| 3.25 Examples of approximating some complicated geometries in FE<br>based mesh ( <a href="#">Burkardt [2011]</a> ) . . . . . | 86 |
| 3.26 First 20 modes of a rectangular waveguide, dimension $2\mu m \times 2\mu m$ ,<br>NA=0.15 . . . . .                      | 87 |

## LIST OF FIGURES

---

|   |     |
|---|-----|
| 3.27 The first and the second modes of the rectangular waveguide with fields along the axis . . . . .   | 88  |
| 3.28 Circular Optical Waveguide structure . . . . .   | 89  |
| 3.29 First 20 modes of a Circular waveguide, core diameter $2\mu m$ , NA=0.15   | 90  |
| 3.30 Comparisons of the field profile of mode 1 and mode 4 of a circular optical waveguide . . . . .  | 91  |
| 3.31 Hexagonal Optical Waveguide Structures . . . . .   | 92  |
| 3.32 First 20 modes of a Hexagonal waveguide, side-side distance $2\mu m$ , NA=0.15 . . . . .   | 93  |
| 3.33 First 20 modes of a Elliptical waveguide, major axis $2.2\mu m$ , minor axis $1.8\mu m$ , NA=0.15 . . . . .  | 94  |
| 3.34 Guide having irregular cross-section Structure . . . . .   | 95  |
| 3.35 First 20 modes of a irregular cross-section waveguide, approximate dimension $2\mu m$ NA=0.15 . . . . .  | 95  |
| 3.36 Structures and the propagation characteristics of the first and the second modes for the first mode of Rectangular, Hexagonal, Circular and irregular cross-sections with similar dimensions . . . . .   | 96  |
| 3.37 $H_{32}^x$ field profiles for a rectangular waveguide . . . . .  | 97  |
| 3.38 Different types of symmetries present in the field profiles of a Hexagonal guide . . . . .   | 97  |
| 4.1 Schematics of a planar waveguide . . . . .  | 100 |
| 4.2 Schematic diagram of the XY plane cross-section of a rectangular guide with lossless core and lossy cladding materials . . . . .  | 101 |
| 4.3 Normalised $n_{eff}$ vs normalised frequency of $H_x^{11}$ mode ( $v$ ) for a $2 \times 2\mu m$ rectangular waveguide for different $\tan \delta$ , $n_{core} = 1.347$ , $n_{cladding} = 1.339$ . . . . . | 102 |
| 4.4 Effective index vs Loss tangent for Rectangular guide with $2 \mu m \times 2 \mu m$ dimension, $n_{core} = 1.347$ , $n_{cladding} = 1.339$ , $\lambda = 550$ nm FEM simulation . . . . .                  | 103 |
| 4.5 Propagation characteristics vs Loss tangent for $d=2\mu m$ , $\lambda=550$ nm, Rectangular guide . . . . .  | 104 |

## LIST OF FIGURES

---

|      |   |     |
|------|---|-----|
| 4.6  | Loss vs Guide Width ( $d$ ) for Different Loss Tangents, $n_{core} = 1.347$ ,<br>$n_{cladding} = 1.339$ , $\lambda = 550$ nm . . . . .  | 105 |
| 4.7  | Real $n_{eff}$ vs $\tan \delta$ for different wavelengths for a $2 \mu\text{m} \times 2 \mu\text{m}$ rectangular waveguide, $n_{core} = 1.347$ , $n_{cladding} = 1.339$ . . . . .       | 106 |
| 4.8  | Imaginary $n_{eff}$ vs $\tan \delta$ , for a $2 \mu\text{m} \times 2 \mu\text{m}$ rectangular waveguide, $n_{core} = 1.347$ , $n_{cladding} = 1.339$ at different wavelengths . . . . . | 107 |
| 4.9  | $H_x$ along dimension for Different Loss Tangents, for a $2 \mu\text{m} \times 2 \mu\text{m}$ rectangular waveguide, $n_{core} = 1.347$ , $n_{cladding} = 1.339$ . . . . .              | 108 |
| 4.10 | Field intensity along guide width for Rectangular guide with $2 \mu\text{m} \times 2 \mu\text{m}$ dimension . . . . .   | 109 |
| 4.11 | Dispersion vs Frequency for a $2 \mu\text{m}$ Rectangular guide for different $\tan \delta$ . . . . .   | 110 |
| 4.12 | Effective index for the first 2 modes with different loss tangents . . . . .  | 112 |
| 4.13 | Confinement factor and Loss vs $\tan \delta$ . . . . .  | 113 |
| 4.14 | Effective index for the first 2 modes with different Guide separation, $d$ . . . . .  | 115 |
| 4.15 | Field intensities of a Rectangular Guide along Guide axis for Different Per, $d$ ; loss-less cladding is considered . . . . .   | 117 |
| 4.16 | Mode 2 cutoff comparison with single guide and periodic guides with different periodicity . . . . .   | 118 |
| 4.17 | Schematics of a Directional Coupler . . . . .   | 119 |
| 4.18 | Coupling Length of a Directional Coupler with lossy cladding . . . . .  | 119 |
| 4.19 | Schematics and the Refractive index ( $n$ ) profiles of a W-fibre like waveguide . . . . .  | 120 |
| 4.20 | Dispersion for Circular insect ommatidium with 3 layers and scattering boundary condition . . . . .   | 121 |
| 4.21 | Dispersion for Circular insect ommatidium with 3 layers and Dirichlet boundary condition . . . . .  | 122 |
| 4.22 | Dispersion for Circular insect ommatidium with 3 layers and Periodic boundary condition . . . . .   | 122 |
| 4.23 | Cross section of a <i>Drosophila melanogaster</i> Ommatidium source: Photobiology . . . . .   | 124 |
| 4.24 | Impact of diffraction on the field profile at the Rhabdom entrance . . . . .  | 124 |
| 4.25 | FDTD simulation of insect ommatidium, 3 layers, loss-less . . . . .   | 126 |

## LIST OF FIGURES

---

|   |     |
|---|-----|
| 4.26 FDTD simulation of insect ommatidium, 3 layers, conductivity<br>$\sigma = 5000$ for the first cladding, the second cladding is loss-less . . .     | 126 |
| 4.27 FDTD simulation of insect ommatidium, 3 layers, conductivity<br>$\sigma = 0$ for the first cladding, $\sigma = 5000$ for the second cladding . . . | 126 |
| 4.28 FDTD simulation of insect ommatidium, 3 layers, loss-less . . . .  | 127 |
| 4.29 Schematics of the position of the point source and the excited<br>modes in rhabdom of compound insect eye . . . . .                                | 128 |
| 4.30 Muller Glial cell of Human retina source: <a href="#">Franze et al. [2007]</a> . . . .   | 129 |

# List of Tables

|     |   |    |
|-----|---|----|
| 1.1 | Permittivities of some Biological Tissues at 100 GHz . . . . .  | 11 |
| 3.1 | Relationship between confinement factor and $n_{eff}$ . . . . .   | 60 |
| 3.2 | TE and TE modes with their respective field components . . . . .  | 61 |
| 3.3 | Mode angles for various normalised heights ( $d/\lambda$ ) of a Planar waveguide, $NA = 0.15$ . . . . . | 64 |

## List of Symbols and Abbreviations

| Symbol        | Description                              |
|---------------|--|
| EM            | Electromagnetic                          |
| FEM           | Finite Element Method                    |
| RS            | Rayleigh-Sommerfeld Diffraction Integral |
| FDTD          | Finite Difference Time Domain            |
| BPM           | Beam Propagation Method                  |
| TE            | Transverse Electric Polarised Mode       |
| TM            | Transverse Magnetic Polarised Mode       |
| $\epsilon'$   | Real part of the Permittivity            |
| $\epsilon''$  | Imaginary part of the Permittivity       |
| $n_{eff}$     | Effective Index                          |
| $\tan \delta$ | Loss Tangent                             |
| $n'$          | Real part of the Refractive Index        |
| $n''$         | Imaginary part of the Refractive index   |

# Chapter 1

## Introduction

It is of considerable interest and importance about the Electromagnetic Wave (EM) propagation through the biological media, and over the last few decades several landmark studies such as by [Johnson and Guy \[1972\]](#), [Sebbah \[2012\]](#), [Ishimaru \[1977\]](#), have conducted to assess the various aspects of the propagation characteristics of EM radiation and interactions. In the rise of the applications in wireless communications to evaluate the impacts of EM wave, especially in Microwave range, on various human tissue have been studied in great details [A Peyman, S Holden \[2000\]](#). In the advent of interest in Vision Research, Biophotonics Research, Biomedical Imaging, Optoelectronics Retinal Prosthesis Systems, Computer Vision and some other similar fields have encouraged the researchers to study interactions of EM wave in the other frequency ranges, especially in the Visible spectrum and IR wavelengths. EM wave penetration, reflection, refraction, absorption, and scattering through various biological structures have been studied by various research groups over a wide frequency range. The advances in optical waveguide technologies have seen a rapid development in methods and techniques in analysing EM wave-material interactions. It has been reported that some biological micro-structures can work as waveguides for Visible and IR radiations. Evolution over millions of years has perfected the engineering designs of some of these structures to a point where it is very likely that studying them in greater details might provide us with some novel designs as well as give us deeper insights into the functionalities of these systems.

Although more than 100 years have been passed for the vision research, many

---

questions remained unexplained. A recent study by [Franze et al. \[2007\]](#) showed that the Glial cells of Human retina act as an optical waveguide that helps to increase the visual acuity, which earlier was considered has no impacts on vision other than providing the mechanical support to the retinal layers. There is still an ongoing debate amongst the researchers whether the Glial cells are acting as optical waveguides or not. Unavailability of the detailed material profiles of the system makes it tough to draw a well-accepted conclusion. Retinal photoreceptors were shown by [Biernson and Kinsley \[1965\]](#) to have waveguide properties. However, the relationship between the Glial cells waveguide and the photoreceptor waveguide has not been established to date. Rhabdom present in the Ommatidium of Insect compound eye was shown by [Stavenga \[1975\]](#) to have waveguide properties. The supported mode shapes of these structures and the roles played by them in vision have not been studied in great details.

The materials used in various waveguide devices are mostly have known material properties with homogeneous material profiles. Most of the materials such as  $SiO_2$ , Silicon, Ge and Quartz have known refractive indices and loss values over a broad range of operating frequencies. The loss values of these materials are usually minuscule ( $\tan \delta \approx 10^{-4}$  or less) and the propagation characteristics obtained by ignoring these losses produce results with the reasonable level of accuracies. Unlike the materials used in the waveguide devices, the materials present in the biological structures are found to have a material loss that cannot be ignored. Studies on these structures ignoring the lossy material might have provided results that are probably inaccurate to some extent. It is thus worth studying the impacts of the lossy materials on the propagation characteristics of these structures in greater details that has the potential to give us new insight into the systems as well as the potential to explain some unexplained phenomena.

The presence of finite apertures (Lens) makes most of the optical instruments diffraction limited. Diffraction sets a fundamental limit to the achievable resolution by any optical instrument. The waveguide nature of the structures present on the back of the biological optical instrument (eye) is receiving the input from the projected image by the diffraction producing element (Lens), indicating that a study relating the fundamental operating blocks might be necessary. Unfortunately, to date, a study that addresses the relationships between Diffraction and

---

the optical waveguides and its impact on the visual process is not available in the literature. It is thus worth studying the biological waveguide structures in visible frequencies and their relationship with the Diffraction present in these systems. The focus of this thesis will be on investigating in determining the impacts of material loss present in the biological structures on their propagation characteristics and relate the presence of diffraction with it. As a test case, Ommatidium of insect (*Drosophila melanogaster*, Fruit fly (Fig. 1.1)) and the Glial cells of the human retina will be considered.

## 1.1 Background

### 1.1.1 Insect eye - Compound eye

Most of the insect species have a compound eye. A compound eye of most of the insects is composed of Ommatidium, the basic building blocks of the system. Figure 1.2 shows the cross-section of a *Drosophila Melanogaster* Compound eye. Each ommatidium, as shown in Fig. 1.3 is composed of a lens, crystalline cone, rhabdom and at the end of the rhabdom the photoreceptors are located. The Rhabdom is surrounded by layers containing pigments that act as an absorbing medium for light. Light is focused by the lens and the crystalline cone on the rhabdom and then the light has to be guided by the rhabdom to be absorbed by the photoreceptors. It was shown in some studies by Neumann [2002] and Land [1997] that they can work as a light guide as the refractive index of the rhabdom was found to be higher than that of it surrounding materials. These studies considered the rhabdom and its surrounding materials to be loss-less, which is not accurate.

The presence of the tiny ( $\approx 20 \mu m$ ) Lens at the beginning of the Ommatidium section and the distance between the lens and the Rhabdom entrance ( $\approx 20 \mu m$ ) makes the system to show strong Diffraction effects. Besides being a Diffraction limited system, the rhabdom entrance is in the Fresnel's zone or near field. In analysing the system's performance thus requires that the roles played by Diffraction and the possible implications of the lossy surroundings of the Rhabdom be taken into account.



Figure 1.1: Image of a Drosophila, source: en.wikipedia.org

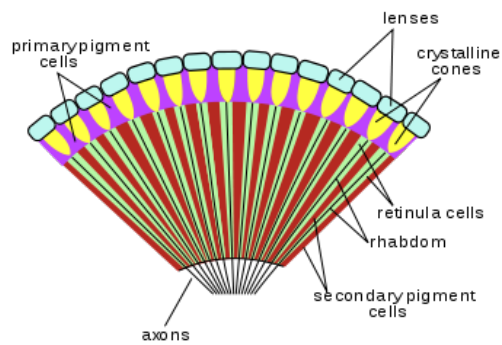


Figure 1.2: Insect Compound Eye Cross-section source: en.wikipedia.org

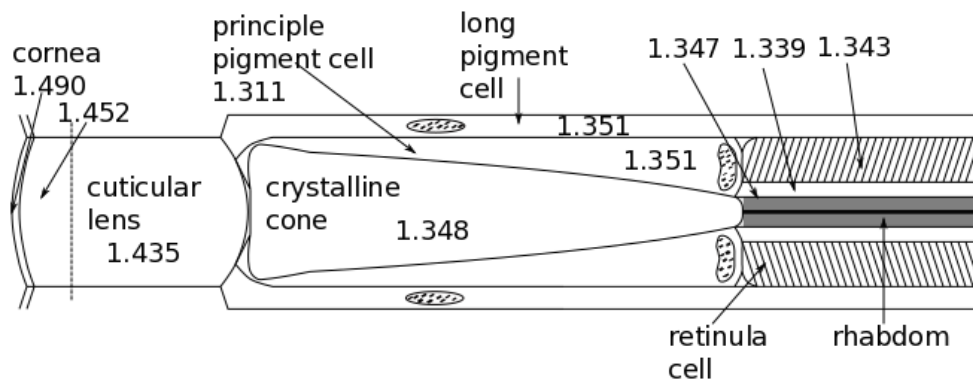


Figure 1.3: Ommatidium Cross-section Smith [2013]

---

### 1.1.2 Absorbing surroundings of the Rhabdom

It is believed that each rhabdom is surrounded by light absorbing layers, pigment layers so that any light tries to escape from the rhabdom can be absorbed by them. It is also believed that the long and short pigment layers, surrounding the Rhabdom as shown in Fig. 1.3 absorbs light that tries to escape the Rhabdom, that means the surrounding materials cannot be loss-less as were considered by the previous studies.

### 1.1.3 Mammal eye

A typical Mammal eye cross-section is shown in Fig. 1.4. The light passes through the cornea, the anterior chamber filled with Aqueous Humor, Pupil, Lens, and the Interior chamber filled with Vitreous Humor to reach the photosensitive layer known as the Retina.

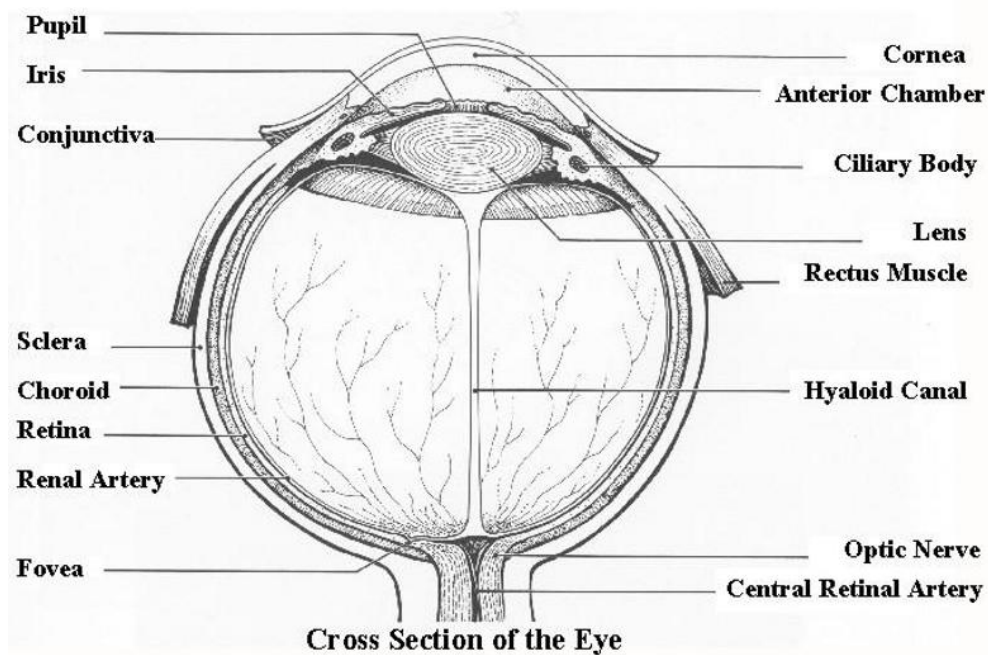


Figure 1.4: A typical Mammal Eye, source: wikimedia commons

Figure 1.6 shows the microstructure of the Retina and its various cell types. The photoreceptors (Cone for colour vision in bright light and the rod for monochro-

---

matic vision in dim light) are located at the back of the Retinal layers just before the pigment cell layer. The light must pass through the different layers of the retina, such as Horizontal cells, Bipolar Cells, Amacrine Cells and Ganglion Cells to reach the photoreceptors. Photoreceptor cells convert the light into electricity and then the electric current is transferred by the Horizontal, Bipolar and Amacrine cells to the Ganglion cells. Ganglion cells are in fact the neurons whose axons form the optic nerve that transfers the visual information acquired by the Retina to Brain for further processing and interpretations.

The seemingly inverted design of the Mammal retina had been a riddle for the vision science researchers as the photoreceptors present at the back of the Retinal layers receive optical stimulations that are passing through the different layer and is expected to suffer severely scattering by them. Muller Cell or the Glial cells, as shown in Fig. 1.7, present in the Retina that spans from the Ganglion cell layer up to the photoreceptor layer were previously considered to provide structural support to the Retinal different layers. It was shown by [Reichenbach et al. \[2012\]](#) that the glial cells work as a light guide between the top surface and the photoreceptor layer and, in fact, enhances the visual acuity to some extent. The Glial cell matrix thus transfers the image information projected by the Eye-Lens on the top surface of the Retina to the Photoreceptor layer, where it is being guided and absorbed by the Photoreceptors. The presence of Bragg grating like optical filter makes the cones sensitive to a certain colour of lights and makes the rods exhibit a broadband response.

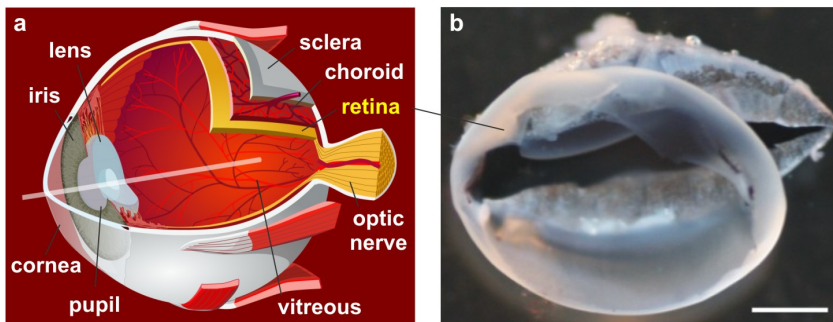


Figure 1.5: Retina Layers and Cross-section [Reichenbach et al. \[2012\]](#)

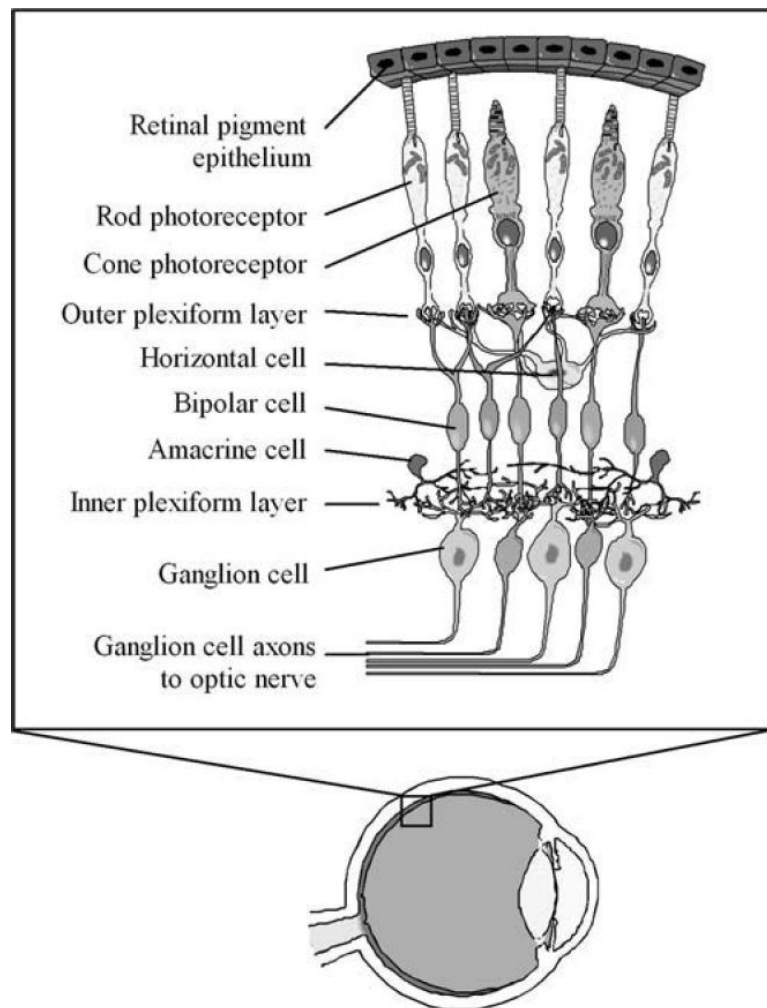


Figure 1.6: Photoreceptors in Mammal Retina, source: [www.bioteaching.com](http://www.bioteaching.com)



Figure 1.7: Retinal Glial or Muller Cell, Original Drawing by Muller Müller [1851]

---

### 1.1.4 Lossy surroundings of the Glial cells

Photocurrent goes in the upward direction through the Human retina, indicating the presence of finite conductivities of the material, thereby lossy for EM wave. The photoreceptors are surrounded by lossy materials as well. Freshly dissected retina in aqueous solution, as shown in Fig. 1.5, shows that it is not transparent, in contrast to the previous belief that the retina is mostly transparent in the visible spectrum. So, the Glial cells are providing a safe passage for the light through the seemingly non-transparent Retinal layers and it can be concluded that the Glial cell surroundings are lossy in visible frequencies.

### 1.1.5 Diffraction in the visual systems

Diffraction occurs when a wave encounters an object or a finite aperture. In classical physics, the phenomenon of diffraction can be described as the interference of waves according to Huygens-Fresnel principle (Papas [2014]). According to this principle, each point on the wavefront acts as a new point source.

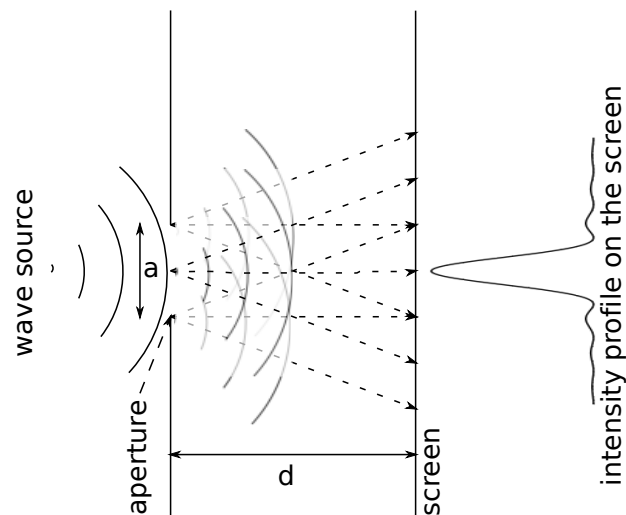


Figure 1.8: Schematics of a single slit diffraction

Figure 1.8 shows a scenario where, a finite aperture of width ' $a$ ' is placed in front of a propagating wave; a screen is located at a distance ' $d$ ' from the aperture.

---

When the wave encounters the aperture, each point on the aperture now acts as a new wave source and they interfere with each other as they propagate.

On the screen, the waves from different points reach with different phases, and at some point when the wavefronts are in phase, constructive interference produces higher intensities, where at some other points the destructive interference produces lower intensities. A typical intensity profile on the screen is shown on the right-hand side of Fig. 1.8.

The intensity profiles generated due to diffraction can be obtained from the scalar solution of the Helmholtz wave equation. There are several methods available in the literature to compute the diffraction profiles, i.e. Kirchoff's Diffraction Integral [Marchand and Wolf \[1966\]](#), Rayleigh-Sommerfeld Diffraction Integral [Osterberg and Smith \[1961\]](#), Fresnel's Diffraction Integral [Mendlovic et al. \[1997\]](#), Fraunhofer's Diffraction Integral [Mendlovic et al. \[1997\]](#), etc. In diffraction theory, the terms 'near-field' and 'far-field' are used that can be described by Fresnel's distance to characterise the properties of diffraction. The Fresnel's distance is given as,

$$d_f = \frac{2D^2}{\lambda} \quad (1.1)$$

where,  $d_f$  is the Fresnel's distance,  $D$  is the aperture size, and  $\lambda$  is the operating wavelength. 'Near-field' refers to the region where the distance is less than  $d_f$ , the region with distance higher than  $d_f$  refers to the 'far-field'.

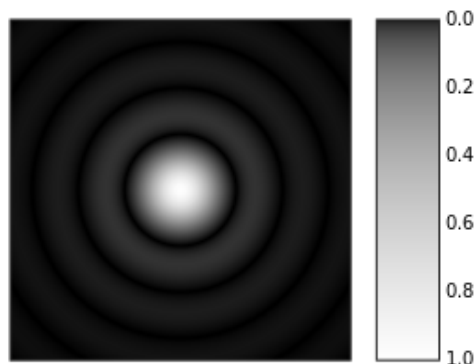


Figure 1.9: Diffraction by a Finite Aperture, source: wikipedia

---

Due to the presence of finite apertures in the visual systems, the quality of the image produced by them are limited by diffraction. The lens present at the beginning of the insect ommatidium and the finite size of the pupil present in mammal eye act as a finite aperture and produce diffraction. Figure 1.9 shows the impact of Diffraction by a finite aperture (For the insect Ommatidium the Lens, for the Mammal eye the pupil) produces airy patterns for a point source.

### 1.1.6 Challenges in modelling biological tissue

Treatment of biological tissue mathematically is a challenging task. Unlike the dielectrics, where no moving charge is present thereby no conduction, biological tissues can conduct electricity. Although they can conduct electricity, the charge carriers are not electrons or holes like metals and semiconductors, but ions are the charge carriers.

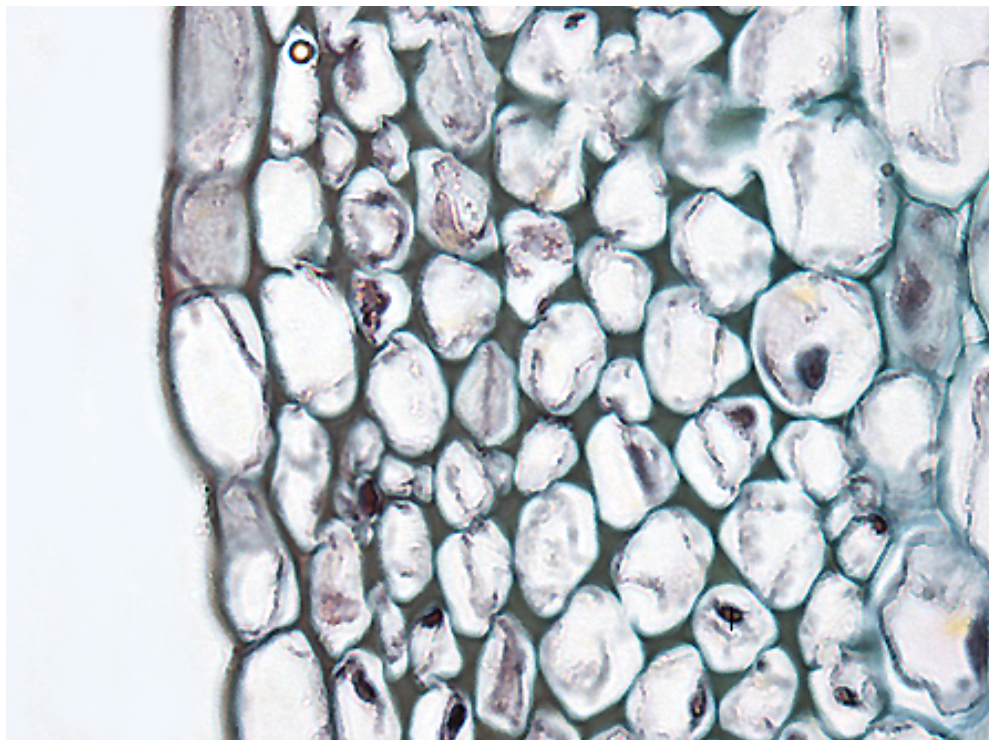


Figure 1.10: Electron Microscope Image of Biological Tissue, Cells

For a living tissue where the metabolism is present, should have different char-

---

acteristics than that of a dead tissue. Incorporating the impacts of the presence of metabolism is a difficult task. The biological tissues can be considered as lossy dielectrics having finite conductivities mathematically to work with the Maxwell's equations. As long as the conductivity is not as high as good conductors, the assumptions should produce reasonably accurate results. Figure 1.10 (source: en.wikipedia.org) shows the electron microscope image of a typical biological tissue that shows that the structure is highly inhomogeneous and full of scattering particles.

Table 1.1 (source: <http://niremf.ifac.cnr.it/>) displays the material properties of some of the biological tissues at 100 GHz frequency that shows that at this frequency most of the materials are lossy. Here  $\epsilon'$  is the real part of the permittivity of the material and  $\tan \delta = \frac{\epsilon''}{\epsilon'}$  is the loss tangent of the material where  $\epsilon''$  is the imaginary part of the material permittivity. For the visible range of frequencies, most of these tissues are opaque thus highly lossy, some of the tissues such as Retina is considered to be loss-less at visible frequencies, that is why the exact values of losses present are not available in the literature.

Table 1.1: Permittivities of some Biological Tissues at 100 GHz

| Specimen       | $\epsilon'$ | $\tan \delta$ |
|----------------|-------------|---------------|
| Blood          | 8.29        | 1.37          |
| skin           | 5.59        | 1.26          |
| Brain          | 6.71        | 1.10          |
| Bone           | 4.10        | 0.70          |
| Liver          | 6.87        | 1.12          |
| Lungs          | 4.00        | 0.96          |
| Retina         | 8.10        | 1.30          |
| Eye Sclera     | 8.11        | 1.30          |
| Cornea         | 7.99        | 7.99          |
| Vitreous Humor | 7.00        | 1.99          |

---

### 1.1.7 Mathematical treatments for lossy medium

The absorbing material can be considered as a lossy dielectric having a permittivity of  $\epsilon = \epsilon_r + j\epsilon_i$ , where  $\epsilon_r$  and  $\epsilon_i$  are the real and imaginary parts of the complex permittivity  $\epsilon$ . For a lossless dielectric material  $\epsilon_i \rightarrow 0$ . Here the dielectric and conduction losses both are combined into  $\epsilon_i$  (Ramo et al. [2008]). In this thesis, the notations  $\epsilon_r = \epsilon'$  and  $\epsilon_i = \epsilon''$  have been used, and the similar notations for the refractive indices ( $n$ ) have also been used. As long as the material under consideration is not metal or plasma, the treatment of losses in this manner produces results within an acceptable level. The refractive index is given by  $n = \sqrt{\epsilon} = n_r + jn_i$ , where  $n_r$  and  $n_i$  are the real and imaginary parts of the refractive index. For most of the structures found in biological tissue the imaginary part of the refractive index  $n_i$  are not available in the literature at optical frequencies. The impacts of losses for these structures has largely been ignored.

Unfortunately, the previous researchers did not pay sufficient attention to the fact that the loss of the material could be (of any use) valuable in characterising their optical properties of these biological structures. That might be the reason the imaginary parts of the refractive indices are so scarce while the real parts are often available in the literature. The presence of loss in the materials of a light guide can change the propagation characteristics to a great extent. It is thus worth investigating the impacts of the material losses of biological structures on the propagation characteristics.

As the imaginary parts of the refractive indices are not available, the computational analysis can be carried out with a range of assumed values for the  $n_i$ .  $n_r$  of the different components of rhabdom of *Drosophila*, Human Glial cell and Photoreceptors of Human retina are however available.

### 1.1.8 Importance of the structure

Insect eye where, the abundance of the processing power of the brain is absent, the structure must be playing a very crucial and important role. For the flying insects, it requires to navigate, avoid an obstacle, searching for a particular object (i.e. flower) in the field, track and avoid attacks, tracking moving objects; all requires

---

a considerable amount of visual processing. The total amount of energy at their disposal is very limited. For the nocturnal flying insects, the amount of available light is very limited as well.

Despite having all these limitations of smaller available energy, lower computational power, lower available light (nocturnal); their visual system must perform very well to survive in nature. A Huge number of well-survived insect species suggests that they are performing very well indeed. The image capturing and projection system (Insect compound eye) must be producing acceptable quality images for the accurate representation of the visual scene, provide sufficient information for motion detection, navigation and tracking. Unavailability of a high-performance processing unit behind the eye imposes the responsibility on the physical structure of the eye so that it reduces the burden on the processing to a great extent and less amount of further processing is required. Hence, the structure of their eye must be playing a very vital role in insect's visual system.

### **1.1.9 Previous studies on these structures**

The refractive indices of the interior materials of Rhabdom, Glial cells and Photoreceptors in the retina, are higher than their surrounding materials. Hence, all these structures can guide EM wave and some studies [Land \[1997\]](#), [Neumann \[2002\]](#) found that these structures can guide light in the visible spectrum.

Propagation characteristics of these tissue structures have been investigated in the literature. In most of these studies, the fact that the biological tissues are lossy in optical frequencies have been ignored. Human retina is considered to be transparent in the visible spectrum, but a freshly dissected human retina in salt water seems to be not transparent that indicate the retinal layers are not lossless in optical frequencies as is assumed frequently. The rhabdom is surrounded by absorbing materials, so undoubtedly the surrounding materials are lossy. The same is true for the retinal photoreceptors.

---

## 1.2 Overlooked problems

### 1.2.1 Presence of biological optical waveguide

A medium (core) can act as a light guide if it is embedded in another medium (cladding) having a lower value of refractive index. Light is being guided by the inner material if the condition  $n_{core} > n_{cladding}$  is satisfied.

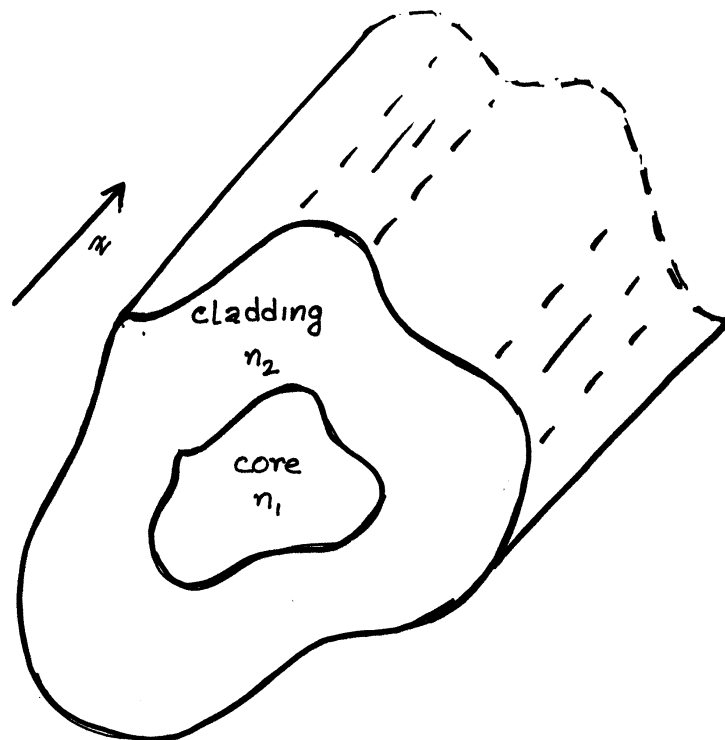


Figure 1.11: Optical waveguide

where,  $n_1$  and  $n_2$  are as shown in Fig. 1.11. If the incident angle is more than the critical angle, then the light or the electromagnetic wave in medium 1 experiences total internal reflection and unable to escape the core material, thereby guided in the core material. By using Snell's law the critical angle,  $\theta_c$  is defined as,

$$\theta_c = \sin^{-1} \frac{n_1}{n_2} \quad (1.2)$$

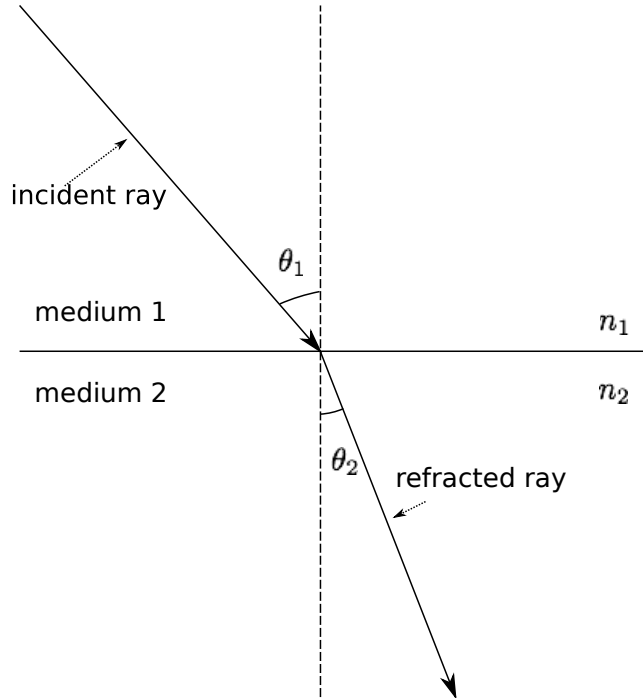


Figure 1.12: Snell's law

For a light guide,  $V = \frac{\pi d}{\lambda} \sqrt{n_1^2 - n_2^2}$ , if  $n_1 > n_2$ ,  $n_1$  is core refractive index,  $n_2$  is cladding refractive index,  $d$  is the diameter of the core,  $V$  is the normalised frequency,  $V \leq 2.405$  ensures single mode condition [Senior \[1992\]](#), it has been found that for the other waveguide types the value is around 2.4. Any material surrounded by a lower index material exhibits properties similar to the waveguide for EM wave.

In biology similar structures are available; [Katz and Minke \[2009\]](#) showed that Rhabdom of insect ommatidium works as an optical waveguide, [Baker \[2010\]](#), [Franze et al. \[2007\]](#) showed the waveguide nature of glial cells present in the human retina and [Labin and Ribak \[2010\]](#), photoreceptors of mammal retina was shown to exhibit waveguide properties that were shown by [Bass et al. \[2001\]](#). The propagations characteristics of these biological waveguides at optical frequencies were shown before. Why these guides are present - are not entirely explained. Lossless materials have been considered in these studies.

---

### 1.2.2 Impacts of lossy surroundings

Propagation characteristics would be different from that of lossless case [Balanis \[1989\]](#). Potentially it could answer some of the unanswered riddles in the visual system.

### 1.2.3 Impacts of neighbouring structures

The previous studies [Neumann \[2002\]](#) treated the structures as that of a single core optical fibre, where it has been considered that the cladding material is extended to infinity. In reality, each of the photo guides is embedded into a photo-guide matrix. The propagation characteristics of a single guide are not only determined by its structure and the material profiles but also the surrounding structures present. These photoguide matrix structures are very similar to that of multi-core optical fibres [Nagashima et al. \[2013\]](#). By choosing appropriate boundary conditions, we can address the presence of the surrounding guides.

### 1.2.4 W-fibre structure in insect rhabdom

Impacts of a 3-layer structure of rhabdom are yet to be explored - dispersion flattening effects, cutoff wavelength shift due to the multi-layered structure needs to be addressed.

### 1.2.5 Limitations of RAY optics based models

Some RAY optics based models of Human eye are presented by [Navarro et al. \[1986\]](#), [Neumann \[2002\]](#), [Navarro \[2009\]](#), and [Talu \[2011\]](#). At smaller retinal eccentricities the impacts of diffraction and spherical aberration can be determined, but the paraxial approximation based calculations cannot be used for larger eccentricities, at the peripheral regions. What intensity profile is present at the guide entrance cannot be explained by these models that are necessary for modal analysis. RAY optics-based methods use the paraxial approximation, makes them useful in determining intensity profiles in the Fraunhofer's zone or far field.

Rhabdom entrance and Glial cell entrance both are in Fresnel's zone or near field region. Paraxial approximation based methods are not suitable for these

---

cases. Even if we can determine the intensity profiles - would only valid for the central 1-5 degrees in the visual field. If we go beyond that angle, the image screen becomes curved.

RAY optics-based methods give us acceptable results when the propagation distance is much large compared to the wavelength ( $r \gg \lambda$ ) and the propagation angle remains small (paraxial approximation). Although, apart from the foveal region of human eye, large angles are required to address the peripheral retina, distance between the lens and the retina that is approximately 22 mm, makes it suitable for the RAY optics based analysis, at the same time makes it computationally too expensive to employ any Time Domain-based numerical methods.

### **1.2.6 Point source position and excited modes**

A point source directly ahead of the ommatidium should excite the fundamental mode for the rhabdom. The other point sources in the surroundings would try to excite the higher order modes that should be blocked by the ommatidium unit to preserve the clarity of the transferred image by the ommatidium mosaic. The exact mechanism of how these higher order modes are being attenuated highly needs more in-depth study.

For the diurnal insects, it has been found that they have apposition eye, where the nocturnal insects most commonly have superposition eye. In superposition eye, each rhabdom takes excitations not only from the points directly ahead of it but also excitations from the neighbouring points. As the light from the neighbouring points fall at a higher angle, they would excite higher order modes in them. Angle dependence of the modes is necessary but not was not explored in details in the previous studies.

## **1.3 Aim of the Thesis**

The prime objective of the thesis is to study the effects of the lossy surrounding materials on the optical modal profiles of the biological structures that work as optical waveguides (i.e. Rhabdom of Insect Ommatidium, Glial cells of Human

---

Retina) in the visible spectrum. The study will characterize not only the individual waveguides but also the impacts of the surrounding waveguides on the characteristics. A link between the RAY optics based analysis and the modal analysis of the optical waveguides will be studied. The angle dependence of the excited optical mode within a waveguide and their consequences will be studied in greater details.

## 1.4 Tools Available

### 1.4.1 Analytical solution

The scalar solution of Helmholtz equation can be obtained as presented by [Balanis \[1989\]](#). As the solution is scalar, the phase information cannot be obtained. As human eye is not phase sensitive, so a scalar solution can be acceptable. All these methods work well for regular geometries. Working with the inhomogeneous material is tough. This solution is suitable for large propagation distance. Fraunhofer's diffraction integral works in the Fraunhofer's ([Manakov \[1973\]](#)) region, for the far field. This method is not suitable for large propagation angles. Fresnel's diffraction integral works well at near field with Fresnel's approximation. However, it is not suitable for the large angles. Kirchhoff's diffraction integral works well for the large angle, but the formula is mathematically inconsistent. The Rayleigh-Sommerfeld diffraction integral(RS) formula is suitable for large propagation angles, and the integral is mathematically consistent. As the analysis of biological structures requires analysis over a large propagation angles, the Kirchhoff's diffraction integral or the RS diffraction integral can be used.

### 1.4.2 Ray Optics

Paraxial approximation ([Lax et al. \[1975\]](#)) makes the RAY optics based models unsuitable for larger angles, and it is very difficult to address irregular geometries with this method. Most of the biological materials have an inhomogeneous material distribution that's hard to simulate with the method. Incorporating materials with a loss in the RAY optics based model is not available in the literature.

---

However, for a brief insight into the system, it might be helpful but not suitable for analysis at sub-wavelength scale with irregularities.

### **1.4.3 Numerical solutions of Maxwell's equations**

#### **1.4.3.1 Finite Difference based modal solutions**

Regular grids used in this method makes the method not suitable where irregular boundaries are present. The inhomogeneous material profile can be handled with this method, and it is computationally less expensive than the finite element based methods. However, the Cartesian grids used to approximate irregular boundaries would produce results with higher numerical errors.

#### **1.4.3.2 FEM based modal solutions**

Finite element based mode solver, as they can use FE meshes, are excellent at approximating structures with irregular boundaries. Inhomogeneous material profiles can be addressed well, but the 2D FEM considers the structure and the materials to be uniform in the direction of propagation, so a structure that has variations in the direction of propagation is difficult to analyse using this method. If it is required to obtain the mode profile at a 2D cross-section, this method can provide us with reasonably accurate results although computationally it is more expensive than the FD based method.

#### **1.4.3.3 BPM**

The research on integrated optical circuits (IOC) and planar optical devices, has emerged from the necessity of calculating the propagation of a light wave in an optical circuit having an arbitrary refractive index distribution. This type of field propagation can be simulated numerically by the beam propagation method (BPM), an approach that was developed in underwater acoustics and seismology before it was adapted to optical waveguide problems by [Feit and Fleck \[1980\]](#). Since then, it has been widely used for analyzing the performance of a light beam propagated in a planar optical circuit that has a nearly stripelike waveguiding structure and in which the refractive index varies smoothly compared with the

---

wavelength. The main features of the BPM are that the electromagnetic fields are Fourier transformed about the direction normal to that of light propagation and that a stepwise method is used for successively calculating the electromagnetic field along the axial direction.

In the BPM, the optical field is transported within one propagation step, from the transverse plane at the longitudinal coordinate  $z$  to the transverse plane at  $z + \Delta z$ . Calculations are performed, to relate the optical fields at the input and the output planes, which are based on the assumption that the dielectric profile within one step,  $\Delta z$ , remains unchanged [Nolting and März \[1995\]](#). As the optical field propagates through the medium, it is subject to diffraction due to its wave nature, and the light rays of the wave experience a certain amount of phase shift, depending on their  $x$  and  $y$  positions. The above influence can be applied one at a time, provided that the space along the path be subdivided into tiny sections,  $\Delta z$ . By doing so, the continuous medium can then be realized as a series of lenses separated by short sections of homogeneous space, where the contribution of the lenses in the phase shift is expressed in the solution of the wave equation. For computational purposes, the wave between the lenses can be decomposed into its spectrum of plane waves by applying a Fast Fourier Transform (**FFT**) algorithm, and then it is reconstructed halfway,  $(\Delta z/2)$ , before the next lens, by applying the inverse FFT. The above process is repeated for each section along the whole propagation path. The propagation step size  $\Delta z$ , which must be at most one wavelength of the light beam, must ensure that the contribution of evanescent waves, which are part of the plane wave, is negligible, and that the rays associated with the wave, travel parallel to the  $z$ -axis, with minimum phase shift.

The BPM is widely accepted as the most powerful method for the analysis of non-uniform structures, but it is not as efficient as the methods specially developed for the analysis of uniform structures, where discretizations in both the transverse and the longitudinal plane are required [Chiang \[1994\]](#). To handle the discretization in the transverse plane, two-dimensional methods can be employed, such as the FDM [Yevick and Hermansson \[1989\]](#) and the FEM [Buah et al. \[1997\]](#). The latter can be used in many devices, such as directional couplers, optical fibres, bent optical waveguides, Bragg and Diffraction gratings, tapered waveguides and optical Y-junctions. It can also be used in conjunction with other numerical

---

techniques such as the Fresnel approximation [Yevick and Hermansson \[1989\]](#).

Beam Propagation Method (BPM) makes paraxial approximations (although non-paraxial approximation is possible as well), so it is not suitable for an abrupt change in field envelopes. It can address inhomogeneous material profiles in the direction of propagation as well as in the cross-section but steps. Computationally the method is much more expensive than the modal analysis but cheaper than the time domain methods. BPM is unable to address reflections from the interfaces, although its Bi-directional variation can do that, more expensive computationally.

#### 1.4.3.4 FETD

The Finite Element (FE) based approaches are better for representing an arbitrarily shaped structure frequently found in the biological structures. To analyze a structure that has an irregular structure, an irregular material profile, and discontinuities are present from where the wave can experience reflections, a Finite Element Time Domain Method (FETD) would have been the ideal choice. The FEM was introduced for the electromagnetic analysis during the 1970's [Silvester \[1969\]](#) to solve primarily the frequency domain problems [Rahman and Davies \[1984\]](#), [Hayata et al. \[1986\]](#). Researchers also tried FEM for time domain analysis [Cangellaris et al. \[1987\]](#); [Feliziani and Maradei \[1994\]](#); [Hesthaven and T \[2001\]](#); [Koshiba et al. \[2000\]](#); [Lee et al. \[1997\]](#); [Songoro et al. \[2010\]](#). Although these methods are sometimes more accurate in structural representation, however some of them may require an implicit solution of the computational domain in each time step [Gedney and Navsariwala \[1995\]](#), some require the solution of the large matrices [Lee et al. \[1997\]](#) and some require higher order solution of the Maxwell's equations [Cangellaris et al. \[1987\]](#); [Hesthaven and T \[2001\]](#); [Songoro et al. \[2010\]](#). However, the methods are computationally slightly more expensive than the FDTD methods, but a well-tested code that is computationally less expensive is not yet available to date that can address the irregular boundaries ([Raiyan Kabir et al. \[2013\]](#)).

---

#### 1.4.3.5 FDTD

In 1966 [Yee et al. \[1966\]](#) proposed a finite difference based technique to solve Maxwell's equations over time to analyze time evolutions of Electromagnetic waves. His proposed method is widely known as the Finite Difference Time Domain (**FDTD**) method. The method uses a rectangular Cartesian grid in 2D and cuboid grid in 3D to discretize the computational domain and solves Maxwell's equations over the domain.

The method is numerically stable and robust. Explicit formulation and the data-parallel nature of the method makes it very fast making it computationally less expensive. For a computational domain with inhomogeneous material profiles and with a geometry that can produce strong reflections, FDTD method has been found to be very useful in dealing with it. Scattering, if present in the system, can be analyzed by using this method. So, for analyzing biological structures, where the inhomogeneous material and irregular structures can produce strong reflections and scattering, the FDTD method can be very useful in analyzing the characteristics of such systems. The method has, however, some disadvantages when deployed in analyzing the biological structures. Due to the use of rectangular or cuboid grids in representing the structures, the method approximates the curved or slanted boundaries with stair-casing, which in turn produces numerical errors. The biological structures, as we know, are most of the cases irregular or semi-irregular in nature; that is why the method is not the optimum choice for biological applications. The method is not suitable for simulations over large distances ( $d \gg \lambda$ ) due to numerical dispersions. So, this method can be considered as the candidate by which the time domain evolution can be analyzed for the irregular structures with the irregular material profiles with less computational power sacrificing the numerical errors due to the FD grid.

## 1.5 Methodology and Study steps

FEM mode solver presented in [Rahman and Davies \[1984\]](#), [Rahman et al. \[1991\]](#) and [Ng and Ooi \[2006\]](#) will be used in the study. COMSOL 4.3 will be used to obtain some of the modal solutions. The study focuses on the study of light propa-

---

gation and guidance through biological optical waveguides having lossy materials. Mode profiles, dispersion characteristics, impacts of losses on various characteristics will be explored. The study will start with a simple structure and move towards a complicated biological structure.

### **1.5.1 Planar structure**

As a beginning, the study will be focused on a planar optical waveguide. The reason behind choosing a planar waveguide is that the Analytic modal solution is available for such waveguides that can be used to benchmark the algorithms. As a planar structure can be considered as a limiting case of a rectangular structure, the characteristics found by analysing a planar structure can be extrapolated to get an approximate idea of the similar characteristics of the rectangular structure. The study on this structure will focus on the following topics,

- Theoretical derivations for modal solutions
- Obtain Mode profiles
- FDTD simulations of these structures

### **1.5.2 3D structures**

Propagation characteristics of 3D optical waveguides with lossy surrounding will then be studied extending the knowledge acquired from planar waveguide studies. The 3D waveguides with the following cross-sections will be explored,

- Rectangular waveguides
- Circular waveguides
- Hexagonal waveguides
- Irregular shaped waveguides

Two types of layered structures are studied

- 2 layers

- 
- 3 layers

The following boundary conditions for each of these case will be tried,

- Dirichlet boundary condition - field zero at the computational domain
- PML boundary condition
- Periodic boundary conditions - considering the array of guides

### **1.5.3 Test cases**

After analysing different types of optical waveguides with various parameters, the study will focus on analysing two biological structures that are known to work as optical waveguides. The first case being the Rhabdom of the Ommatidium of the compound eye of the *Drosophila Melanogaster* (Fruit Fly), and the second being the Glial cells of the Retina of Human Eye.

#### **1.5.3.1 *Drosophila Melanogaster* (Fruit fly) Compound Eye**

The study will analyse the Rhabdom on the following key points,

- Mode profiles
- Single mode operating wavelength range
- 2 layers and 3 layers
- Periodic boundary conditions and its impact
- Coupling amongst the surrounding guides
- How loss is exploited

#### **1.5.3.2 Glial cells of Human Retina**

The characteristics of the Glial cells of Human Retina will be analysed focusing on the following points,

- Mode profiles

- 
- Directional sensitivity - leading to an explanation of Stiles-Crawford effect of first and second kind
  - Impacts of lossy surroundings

### 1.5.3.3 Integrated Diffraction integral and Modal solutions

Rayleigh-Sommerfeld diffraction integral is used to determine the field intensity profile at the glial cell entrance of the retina of the human eye. The field profile at the entry of the rhabdom of the Ommatidium of insects' compound eyes is determined. Field profiles found from the modal solutions are compared with the diffraction patterns. FDTD is used to assess the propagation characteristics of such field profiles. The relationship between the field profiles found by the RS diffraction integral and field patterns for the supported mode profiles of these guides will be analysed.

The following topics are included in the step by step study,

1. RS diffraction integral to evaluate the field profiles from the pupil to the glial cell entrance of Human eye; Lens to rhabdom entrance of the compound eye of insect (*Drosophila*).
2. Ray optics to determine the angle of incidents over the retinal eccentricities.
3. Theoretical derivations for planar structures with lossy medium and their numerical evaluations.
4. FEM to determine the mode profiles for rectangular, square, circular, hexagonal and irregular shaped guides with as well as without losses.
5. Test cases: *Drosophila* rhabdom and Glial cells of human retina.
6. Relate the ray optics, RS, FEM and FDTD findings.
7. Impacts of loss on mode profiles, dispersion and cutoff wavelength.
8. Single mode cutoff wavelengths for different structures.
9. Periodic boundary conditions on mode profiles, dispersion, and cutoff wavelengths.

- 
10. Coupling amongst the neighbouring guides.
  11. Stiles-Crawford effect.

## **1.6 Thesis organization**

The thesis is organised into five chapters. Chapter 2 gives detailed account of the theories required to perform the simulations, such as Maxwell's equation, Finite Element Method (FEM), Finite Difference Time Domain Method (FDTD), Beam Propagation Method (BPM), Rayleigh-Somerfield (RS) diffraction integral, and RAY optics fundamentals. The theoretical development of the simulation environment is given in Chapter 3. The necessary derivations are also included in that chapter. Chapter 4 contains the results found and their implications for vision. An explanation of the Retinal Stiles-Crawford effect is given in light of the findings of the thesis is also provide in Chapter 4. Concluding remarks and the scopes for the future research after this study is found in the last chapter of this thesis.

# Chapter 2

## Simulation Environment

### 2.1 Maxwell's Equations

The Maxwell's equations can characterise the propagation of Electromagnetic wave. Maxwell's equations comprise a set of four electromagnetic field vectors that describe the governing laws of electromagnetic wave propagation. The vectors are electric field intensity  $\mathbf{E}$  (Volts/meter), the magnetic field intensity  $\mathbf{H}$  (Amperes/Meter), the electric flux density  $\mathbf{D}$  (Coulombs/ $m^2$ ) and the magnetic flux intensity  $\mathbf{B}$  (Tesla). For a source-free region, time-dependent equations can be expressed in differential and integral forms. In FEM, we formulate the problem as a boundary value problem with a set of differential equations. The differential form of Maxwell's equations can be given as follows,

$$\nabla \times \mathbf{E} + \frac{\partial \mathbf{B}}{\partial t} = 0 \quad (2.1)$$

$$\nabla \times \mathbf{H} - \frac{\partial \mathbf{D}}{\partial t} = 0 \quad (2.2)$$

$$\nabla \cdot \mathbf{D} = \rho \quad (2.3)$$

$$\nabla \cdot \mathbf{B} = 0 \quad (2.4)$$

---


$$\mathbf{D} = \epsilon \mathbf{E} \quad (2.5)$$

$$\mathbf{B} = \mu \mathbf{H} \quad (2.6)$$

Here,  $\rho$  is the electric charge density (Coulombs/ $m^3$ ). The permittivity  $\epsilon$  and the permeability  $\mu$  of the medium can be given as,

$$\epsilon = \epsilon_0 \epsilon_r \quad (2.7)$$

$$\mu = \mu_0 \mu_r \quad (2.8)$$

where,  $\epsilon_0$  is the permittivity of the free space ( $8.854 \times 10^{-12}$  Farads/meter),  $\epsilon_r$  is the relative permittivity of the medium,  $\mu_0$  is the permeability of the free space ( $4\pi \times 10^{-7}$  N/ $A^2$ ) and  $\mu_r$  is the relative permeability of the medium. When we consider a material in optical frequencies another parameter, refractive index  $n$  is very often used that can be expressed in terms of  $\epsilon_r$  and  $\mu_r$  as follows,

$$n = \sqrt{\epsilon_r \mu_r} \quad (2.9)$$

for a non-magnetic material  $\mu_r = 1$ , in this case,

$$n = \sqrt{\epsilon_r} \quad (2.10)$$

### Boundary Conditions

At the material interface between two media, a set of conditions must be met by the field equations, these are known as the boundary conditions. Figure 2.1 shows a structure with two mediums, Medium 1 with a refractive index  $n_1$  and Medium 2 with a refractive index  $n_2$ , and the unit normal vector  $\mathbf{n}$  is the normal to the interface directed from Medium 1 to Medium 2. For a medium with no surface charge ( $\mathbf{J} = 0$ ) and no charges ( $\rho = 0$ ), the boundary conditions are as follows,

- 
1. The tangential components of the electric fields must be continuous

$$\mathbf{n} \times (\mathbf{E}_1 - \mathbf{E}_2) = 0 \quad (2.11)$$

2. The tangential components of the magnetic fields must be continuous

$$\mathbf{n} \times (\mathbf{H}_1 - \mathbf{H}_2) = 0 \quad (2.12)$$

3. The normal components of the electric flux density must be continuous

$$\mathbf{n} \cdot (\mathbf{D}_1 - \mathbf{D}_2) = 0 \quad (2.13)$$

4. The normal components of the magnetic flux density must be continuous

$$\mathbf{n} \cdot (\mathbf{B}_1 - \mathbf{B}_2) = 0 \quad (2.14)$$

If one of the media is a perfect conductor, at the interface the following conditions must be met to ensure the continuity of the fields. Such a boundary is known as the electric wall boundary condition.

$$\mathbf{n} \times \mathbf{E} = 0 \quad \text{or} \quad \mathbf{n} \cdot \mathbf{H} = 0 \quad (2.15)$$

If one of the media is a perfect magnetic conductor, the magnetic wall boundary condition can be given as,

$$\mathbf{n} \times \mathbf{H} = 0 \quad \text{or} \quad \mathbf{n} \cdot \mathbf{E} = 0 \quad (2.16)$$

In analysing optical waveguide devices at the boundary of the waveguide, additional boundary conditions are considered. The boundary conditions are as follows,

$$\Phi = 0 \quad \text{Homogenous Dirichlet} \quad (2.17)$$

$$\Phi = k \quad \text{Inhomogenous Dirichlet} \quad (2.18)$$

---


$$\frac{\partial \Phi}{\partial \mathbf{n}} = 0 \quad \text{Homogenous Neuman} \quad (2.19)$$

Here the  $\phi$  can be the electric or the magnetic field,  $k$  is a constant and  $\mathbf{n}$  is the unit normal to the interface. In Homogeneous Dirichlet the field value at the computational boundary is considered to be 0, in Inhomogeneous Dirichlet it is considered that constant valued field specified by the constant  $k$  is present at the border and in Neumann boundary condition considers that the rate of change of the field with respect to the surface normal  $\mathbf{n}$  is 0.

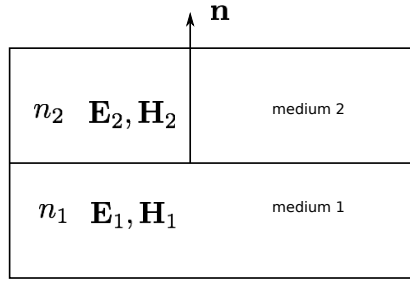


Figure 2.1: Boundary between two media having refractive indices  $n_1$  and  $n_2$ ,  $\mathbf{n}$  being the unit vector normal to the interface

### Wave Equation

For an isotropic, loss-less ( $\mathbf{J} = 0$ ,  $\rho = 0$ ) and non-magnetic ( $\mu = \mu_0$ ) material with a permittivity  $\epsilon$  the Maxwell's equation for the 3-D case can be written as follows,

$$\nabla^2 \mathbf{E} + k^2 \mathbf{E} = 0 \quad (2.20)$$

$$\nabla^2 \mathbf{H} + k^2 \mathbf{H} = 0 \quad (2.21)$$

where the  $k$  (rad/m) being the wavenumber that is given as,

$$k = \omega \sqrt{\epsilon \mu_0} \quad (2.22)$$

when  $\epsilon = \epsilon_0$  (free space), the free space wavenumber  $k_0$  is given by,

$$k_0 = \omega \sqrt{\epsilon_0 \mu_0} \quad (2.23)$$

---

Equations 2.20 and 2.21 are known as Helmholtz wave equations in 3-D.

### 2.1.1 Variational Formulation

The finite-element formulation can be based on the variational or Raleigh-Ritz approach. These can be in scalar form, where only one electric or magnetic field component is considered; or in vector form where the electric or magnetic field is expressed in terms of at least two components. Most of the formulations applied to FEM gives us a standard eigenvalue problem of the following form,

$$[\mathbf{A}]\{x\} - \lambda[\mathbf{B}]\{x\} = 0 \quad (2.24)$$

where  $[A]$  and  $[B]$  are real symmetric sparse matrices, and  $\mathbf{B}$  is positive definite. The eigenvalue  $\lambda$  can be chosen as  $\beta^2$  or  $k^2$ , depending on the formulations and the eigenvector  $\mathbf{x}$  represents the nodal field values of the finite elements.

### 2.1.2 Scalar Approximation

The scalar approximation can be applied in the situations where the fields can be describes as TE (Transverse Electric) or TM (Transverse Magnetic) modes. For the quasi-TE modes over a region  $\Omega$  with  $E_x$  being the dominant field component, the formulation describes by Mabaya et al. [1981] as follows,

$$L = \int \int_{\Omega} \left[ \left( \frac{\partial E_x}{\partial x} \right)^2 + \left( \frac{\partial E_x}{\partial y} \right)^2 - k_0^2 n^2 E_x^2 + \beta^2 E_x^2 \right] d\Omega \quad (2.25)$$

For the quasi-TM mode with dominant  $H_x$  component, the formulation can be written as follows,

$$L = \int \int_{\Omega} \left[ \frac{1}{n^2} \left( \frac{\partial H_x}{\partial x} \right)^2 + \frac{1}{n^2} \left( \frac{\partial H_x}{\partial y} \right)^2 - k_0^2 H_x^2 + \frac{1}{n^2} \beta^2 H_x^2 \right] d\Omega \quad (2.26)$$

### 2.1.3 Vector Formulation

The scalar formulation is inadequate to handle waveguides with inhomogeneous or non-isotropic material profiles. For waveguides with 3-D geometry (2-D cross-

---

section), where all 6 components of the fields (Electric :  $E_x$ ,  $E_y$  and  $E_z$  ; Magnetic  $H_x$ ,  $H_y$ , and  $H_z$ ) can be present, cannot be analysed by using a scalar formulation. Although vector  $\mathbf{E}$  field based formulations have been used earlier, but the vector  $\mathbf{H}$  field based formulation is found to be more suitable for analysing dielectric optical waveguides, because the magnetic field is continuous everywhere, as long as the material is non-magnetic for which  $\mu = \mu_0$ , and the natural boundary conditions correspond to that of an electric wall, therefore no enforced boundary conditions are required. The formulation is as follows,

$$\omega^2 = \frac{\int (\nabla \times \mathbf{H})^* \cdot \hat{\epsilon}^{-1} \cdot (\nabla \times \mathbf{H}) d\Omega}{\int \mathbf{H}^* \cdot \hat{\mu} \cdot \mathbf{H} d\Omega} \quad (2.27)$$

here,  $\omega$  is the angular frequency in radians,  $\Omega$  is the waveguide cross-section,  $\hat{\epsilon}$  is the permittivity tensor and  $\hat{\mu}$  is the permeability tensor. In order to obtain a stationary solution for the function in equation 2.27, the expression is minimised with respect to the components  $H_x$ ,  $H_y$  and  $H_z$ . This minimization leads to the matrix eigenvalue equation as of equation 2.24, where  $[\mathbf{A}]$  is a complex Hermitian matrix and  $[\mathbf{B}]$  is a real symmetric and positive-definite matrix. The eigenvalue  $\lambda$  is proportional to  $\omega^2$  and the eigenvectors  $\{x\}$  are the  $\mathbf{H}$  field values at the node points of the elements. The iterative solution starts with an initial guess of the propagation constant  $\beta$  for a given wavelength, equation 2.24 is then used to determine a value of the eigenvector  $\{x\}$ , the obtained eigenvectors  $\{x\}$  is then used to determine a new value for the propagation constant  $\beta$ ; the process continues until the values of  $\beta$  and  $\{x\}$  converges to a stable state. By choosing different values of the initial guess  $\beta$ , it is possible to find out all the supported modes for a given wavelength. By varying the operating wavelengths, the dispersion characteristics can be determined. Although the formulation is based on  $\mathbf{H}$  fields, by using the coupled Maxwell's equations, it is possible to calculate the  $\mathbf{E}$  field components.

If the divergence condition,  $\nabla \cdot \mathbf{H} = 0$ , is not satisfied with the iterative solution might produce non-physical solutions referred to as spurious solutions. Special care must be taken to eliminate the spurious solutions that will be discussed in another section of this Chapter.

---

### 2.1.4 Natural Boundary Condition

The boundary condition that is automatically satisfied when left free in variational methods is known as the 'natural boundary condition'. The scalar formulation of equation 2.25 has the continuity of  $\frac{\partial E_x}{\partial \mathbf{n}}$  as the natural boundary condition, and equation 2.26 has  $\frac{1}{n^2} \frac{\partial H_x}{\partial \mathbf{n}}$  as the natural boundary condition. Here,  $\mathbf{n}$  is the outward normal unit vector to the interface. The vector formulation in equation 2.27 has  $\mathbf{n} \cdot \mathbf{H} = 0$  (Electric wall) as the natural boundary condition. Therefore, for conducting guide wall, it is not necessary to enforce any boundary condition as the natural boundary condition is automatically satisfied. However, for a guide with regular geometry, exploiting the boundary condition can lead us with reduced matrix problem size. Proper use of symmetry and boundary condition can be useful in cases where mode degeneration is present.

## 2.2 Numerical Solution of Maxwell's equation

For three dimensional waveguides that are more commonly used in today's photonics systems, the analytical solutions in closed form are not always obtainable. Whenever exact analytical solutions are not available, the approximate solutions are sought. Finite Element Method (FEM) is used in modal analysis of optical waveguides by solving Maxwell's Equations numerically and FDTD is used to study the time evolution of electromagnetic fields within the waveguides. These two numerical methods and various technical aspects of them are described in the following sections.

### 2.2.1 Finite Element Method (FEM)

The finite element method tries to solve a complicated problem by replacing it with several simpler ones. The physical problem described by the differential equations are replaced by an appropriate functional  $J$  that is the variational formulation for the desired result. The problem can be considered as obtaining the solution of  $\mathbf{H}$  over a region in the transverse plane satisfying the boundary conditions. The axial dependence is assumed as  $e^{-j\beta z}$ , and the discretization is performed in the transverse plane.

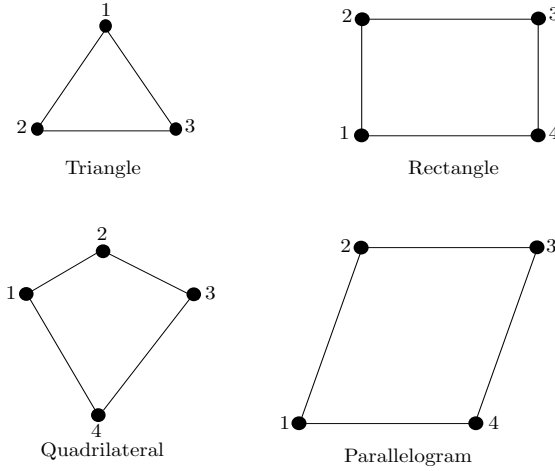


Figure 2.2: Finite Elements in 2D

### 2.2.1.1 Discretisation

The initial step of a finite element method is to discretise the domain into sub-regions (finite elements). The shapes, sizes, number and configurations of the elements have to be chosen carefully so that the domain under consideration is approximated well without increasing the computational requirements too much. Each element is a unit where the unknown quantities are described in a simple manner. There are various types of elements available; one, two or three dimensional. When the geometry and the material profiles can be described in terms of only one spatial coordinate, then one-dimensional elements can be used. For a two-dimensional case, the elements were shown in Fig. 2.2 can be used. The most commonly used two-dimensional element is the triangular element. The accuracy of the solution depends on the size and the order of the elements used, where in general a smaller sized element produces more accurate results, however, smaller element size means increased number of elements and increased computational cost. Higher order elements tend to produce more accurate results at the expense of increased computational load. A domain with an arbitrary cross-section in 2D is discretised using first order triangular elements has been shown in Fig. 2.3. After dividing the waveguide cross-section into many triangular elements, the unknown  $\mathbf{H}$  is discretised into the corresponding sub-regions. The nodal points

after the discretization are the vertices of the elements, and the  $\mathbf{H}$  field values in these nodes are the unknown values of the method. Figure 2.3

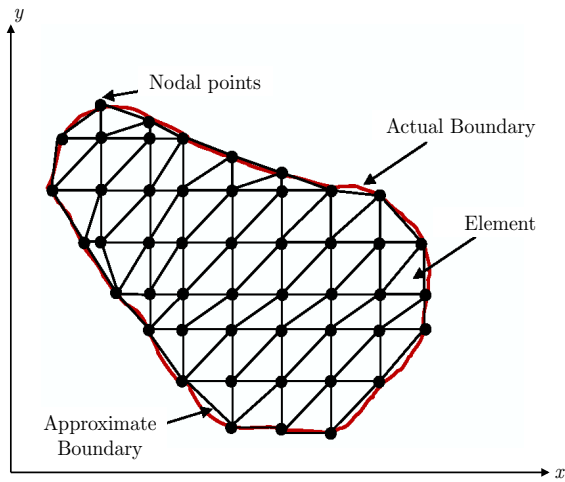


Figure 2.3: FEM discretisation of a 2D domain using triangular elements

### 2.2.1.2 Shape Function

In the two-dimensional problem, the field value within the element is found by linear interpolation of the field values of the nodes. Within each element the unknown field  $\mathbf{H}$  is approximated by a suitably chosen polynomial. These polynomials are known as the ‘shape function’. The polynomials of different degrees can be formed according to Pascals triangle as shown in Fig. 2.4.

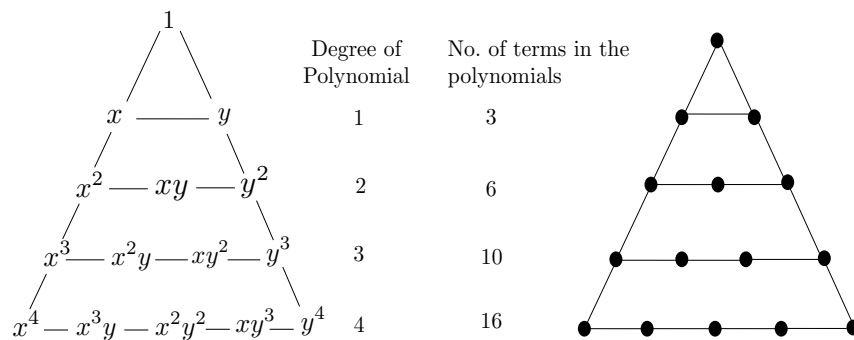


Figure 2.4: Pascal's triangle

The first-degree polynomial involves three coefficients and can be expressed in terms of three nodal values at the triangular vertices. The second-degree polynomial requires six coefficients and can be expressed in terms of values of six nodes as shown in Fig 2.4.

The continuous field function  $\phi(x, y)$  can be replaced with a set of discrete values  $(\phi_i, \quad i = 1, 2, 3, \dots, m)$ , where  $m$  is the total number of nodes. A typical first order triangular element used in these methods is shown in Fig. 2.5.

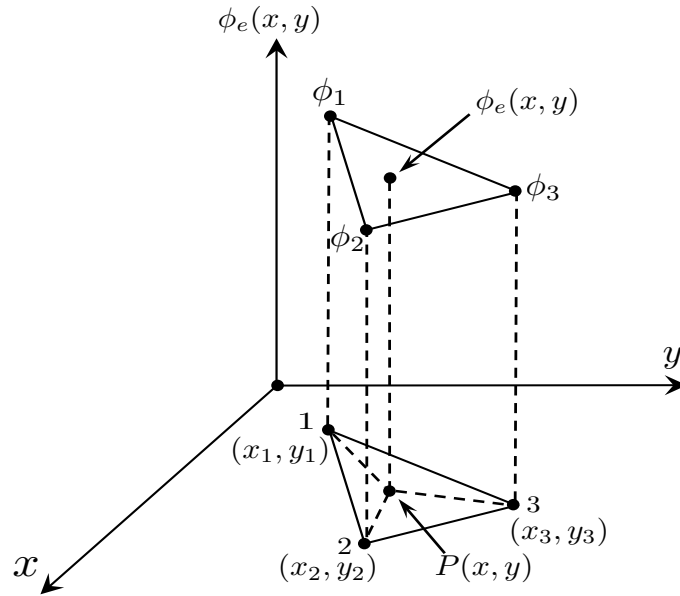


Figure 2.5: Representation of a first order triangular element

Inside the element the element field value  $\phi_e(x, y)$  can be found by interpolation, and an interpolation function  $N_i(x, y)$  is used in this regard. Using the interpolations function, the element field value can be written as follows,

$$\phi_e(x, y) = \sum_{i=1}^3 N_i(x, y) \cdot \phi_i \quad (2.28)$$

where,  $\phi_i$  are the nodal field values. The functions  $N_i(x, y)$  are known as ‘shape

---

functions'. In matrix form the equation 2.28 can be written as follows,

$$\phi_e(x, y) = [N_1 N_2 N_3] \begin{Bmatrix} \phi_1 \\ \phi_2 \\ \phi_3 \end{Bmatrix} \quad (2.29)$$

$$\phi_e(x, y) = [N] \{\phi_e\} \quad (2.30)$$

where,  $[N]$  is the shape function matrix and the  $\{\phi_e\}$  is a column vector whose components are the field values at the three vertices of the triangular element. In order to obtain the shape function  $N_i(x, y)$ ,  $i = 1, 2, 3$ , the fields inside the elements can be approximated as,

$$\phi_e(x, y) = \alpha_1 + \alpha_2 x + \alpha_3 y \quad (2.31)$$

here,  $\alpha_1$ ,  $\alpha_2$  and  $\alpha_3$  are the constants. By rewriting the above relations we get,

$$\phi_e(x_i, y_i) = \phi_i \quad i = 1, 2, 3 \quad (2.32)$$

where,  $(x_i, y_i)$  ( $i=1, 2, 3$ ) are the global coordinates of the vertices of the triangular elements. The nodal field values  $\phi_i$  can now be expressed as,

$$\begin{aligned} \phi_1 &= \phi_e(x_1, y_1) = \alpha_1 + \alpha_2 x_1 + \alpha_3 y_1 \\ \phi_2 &= \phi_e(x_2, y_2) = \alpha_1 + \alpha_2 x_2 + \alpha_3 y_2 \\ \phi_3 &= \phi_e(x_3, y_3) = \alpha_1 + \alpha_2 x_3 + \alpha_3 y_3 \end{aligned} \quad (2.33)$$

in matrix form,

$$\begin{Bmatrix} \phi_1 \\ \phi_2 \\ \phi_3 \end{Bmatrix} = \begin{bmatrix} 1 & x_1 & y_1 \\ 1 & x_2 & y_2 \\ 1 & x_3 & y_3 \end{bmatrix} \begin{Bmatrix} \alpha_1 \\ \alpha_2 \\ \alpha_3 \end{Bmatrix} \quad (2.34)$$

the constants  $\alpha_1$ ,  $\alpha_2$  and  $\alpha_3$  can be determined by solving the matrix equation 2.34 and can be expressed as,

$$\alpha_1 = \frac{1}{2A_e} [\phi_1(x_2 y_3 - x_3 y_2) + \phi_2(x_3 y_1 - x_1 y_3) + \phi_3(x_1 y_2 - x_2 y_1)] \quad (2.35)$$

---


$$\alpha_2 = \frac{1}{2A_e}[\phi_1(y_2 - y_3) + \phi_2(y_3 - y_1) + \phi_3(y_1 - y_2)] \quad (2.36)$$

$$\alpha_3 = \frac{1}{2A_e}[\phi_1(x_3 - x_2) + \phi_2(x_1 - x_3) + \phi_3(x_2 - x_1)] \quad (2.37)$$

here,  $A_e$  is the area of the triangular element given by,

$$A_e = \frac{1}{2} \begin{vmatrix} 1 & x_1 & y_1 \\ 1 & x_2 & y_2 \\ 1 & x_3 & y_3 \end{vmatrix} = \frac{1}{2} [(x_2y_3 - x_3y_2) + (x_3y_1 - x_1y_3) + (x_1y_2 - x_2y_1)] \quad (2.38)$$

Using the obtained values of  $\alpha_i$ , the equation for the field values can be written as,

$$\phi_e(x, y) = N_1(x, y) \cdot \phi_1 + N_2(x, y) \cdot \phi_2 + N_3(x, y) \cdot \phi_3 \quad (2.39)$$

so,

$$\phi_e(x, y) = [N]\{\phi_e\} \quad (2.40)$$

$N_i(x, y)$   $i = 1, 2, 3$  are the shape functions that is given by,

$$[N]^T = \begin{bmatrix} N_1 \\ N_2 \\ N_3 \end{bmatrix} = \frac{1}{2A_e} \begin{bmatrix} x_2y_3 - x_3y_2 & y_2 - y_3 & x_3 - x_2 \\ x_3y_1 - x_1y_3 & y_3 - y_1 & x_1 - x_3 \\ x_1y_2 - x_2y_1 & y_1 - y_2 & x_2 - x_1 \end{bmatrix} \begin{bmatrix} 1 \\ x \\ y \end{bmatrix} \quad (2.41)$$

$$[N]^T = \begin{bmatrix} N_1 \\ N_2 \\ N_3 \end{bmatrix} = \begin{bmatrix} a_1 + b_1x + c_1y \\ a_2 + b_2x + c_2y \\ a_3 + b_3x + c_3y \end{bmatrix} \quad (2.42)$$

$a_i, b_i, c_i$  ( $i=1, 2, 3$ ) are the constants that are expressed as,

$$\begin{aligned} a_1 &= \frac{x_2y_3 - x_3y_2}{2A_e} \\ b_1 &= \frac{y_2 - y_3}{2A_e} \\ c_1 &= \frac{x_3 - x_2}{2A_e} \end{aligned} \quad (2.43)$$

the other constants  $a_2, b_2, c_2, a_3, b_3,$  and  $c_3$  can be calculated in the similar way by cyclic exchange of  $1 \rightarrow 2 \rightarrow 3$  in equation 2.43. The shape functions

---

$N_i$  can be expressed in terms of the areas of the triangles shown in Fig. 2.5 as follows,

$$N_i = \frac{\text{area of sub triangle } P_{23}}{\text{area of sub triangle } 123} \quad (2.44)$$

$N_2$  and  $N_3$  can be determined in the similar way and the  $N_i$  must satisfy the following condition,

$$\sum_{i=1}^3 N_i = 1 \quad (2.45)$$

### 2.2.1.3 Global and Element Matrices

The solution to the optical waveguide problem by FEM can be transformed into an eigenvalue problem expressed in equation 2.24, where the matrices [A] and [B] are global matrices comprises of the summation of the elements matrices. The waveguide cross-section is discretized by using first order triangular elements; each element is used to form the element matrices, combining the element matrices results in the global matrices. This section describes the procedures for formulating global matrices for variational formulation. Throughout this procedure, the first order triangular elements are being used and the full vectorial  $\mathbf{H}$  field is being used. The the  $\mathbf{H}$  field components  $H_x$ ,  $H_y$  and  $H_z$  within each elements can be written as,

$$H_x(x, y) = \begin{bmatrix} N_1 & N_2 & N_3 \end{bmatrix} \begin{bmatrix} H_{x1} \\ H_{x2} \\ H_{x3} \end{bmatrix} \quad (2.46)$$

$$H_y(x, y) = \begin{bmatrix} N_1 & N_2 & N_3 \end{bmatrix} \begin{bmatrix} H_{y1} \\ H_{y2} \\ H_{y3} \end{bmatrix} \quad (2.47)$$

$$H_z(x, y) = \begin{bmatrix} N_1 & N_2 & N_3 \end{bmatrix} \begin{bmatrix} H_{z1} \\ H_{z2} \\ H_{z3} \end{bmatrix} \quad (2.48)$$

---

here ,  $H_{xi}$ ,  $H_{yi}$  and  $H_{zi}$  ( $i=1, 2, 3$ ) are the field components at the  $i$  nodes of the elements. The magnetic field over the element  $[H]_e$  can be expressed as,

$$[H]_e = \begin{bmatrix} H_x(x, y) \\ H_y(x, y) \\ H_z(x, y) \end{bmatrix} = \begin{bmatrix} N_1 & N_2 & N_3 & 0 & 0 & 0 & 0 & 0 & 0 \\ 0 & 0 & 0 & N_1 & N_2 & N_3 & 0 & 0 & 0 \\ 0 & 0 & 0 & 0 & 0 & 0 & N_1 & N_2 & N_3 \end{bmatrix} \begin{bmatrix} H_{x1} \\ H_{x2} \\ H_{x3} \\ H_{y1} \\ H_{y2} \\ H_{y3} \\ H_{z1} \\ H_{z2} \\ H_{z3} \end{bmatrix} \quad (2.49)$$

in an more concise matrix form,

$$[H]_e = [N]\{H\}_e \quad (2.50)$$

here,  $\{H\}_e$  is the column vector containing the three components of the nodal field values and  $[N]$  is the shape function matrix. The curl equation can now be written as,

$$(\nabla \times \tilde{H})_e = \nabla \times [N]\{\tilde{H}\}_e = \begin{bmatrix} 0 & -\partial/\partial z & \partial/\partial y \\ \partial/\partial z & 0 & -\partial/\partial x \\ -\partial/\partial y & \partial/\partial x & 0 \end{bmatrix} [N]\{\tilde{H}\}_e = [Q]\{\tilde{H}\}_e \quad (2.51)$$

where the matrix  $[Q]$  is,

$$[Q] = \begin{bmatrix} [0] & -\partial[N]/\partial z & \partial[N]/\partial y \\ \partial[N]/\partial z & 0 & -\partial[N]/\partial x \\ -\partial[N]/\partial y & \partial[N]/\partial x & 0 \end{bmatrix} \quad (2.52)$$

where,

$$[0] = \begin{bmatrix} 0 & 0 & 0 \end{bmatrix} \quad \text{and} \quad [N] = \begin{bmatrix} N_1 & N_2 & N_3 \end{bmatrix} \quad (2.53)$$

and,

$$\begin{aligned}\frac{\partial N_1}{\partial x} &= b_1 & \frac{\partial N_2}{\partial x} &= b_2 & \frac{\partial N_3}{\partial x} &= b_3 \\ \frac{\partial N_1}{\partial y} &= c_1 & \frac{\partial N_2}{\partial y} &= c_2 & \frac{\partial N_3}{\partial y} &= c_3\end{aligned}\quad (2.54)$$

The variational formulation of equation 2.27 can now be written as,

$$\omega^2 = \frac{\int (\nabla \times \mathbf{H})^* \cdot \hat{\epsilon}^{-1} \cdot (\nabla \times \mathbf{H}) d\Omega}{\int \mathbf{H}^* \cdot \hat{\mu} \cdot \mathbf{H} d\Omega} \quad (2.55)$$

$$\omega^2 = \frac{\int_{\Delta} ([Q]\{\mathbf{H}\}_e)^* \cdot \hat{\epsilon}^{-1} \cdot ([Q]\{\mathbf{H}\}_e) d\Omega}{\int_{\Delta} ([N]\{\mathbf{H}\}_e)^* \cdot \hat{\mu} \cdot ([N]\{\mathbf{H}\}_e) d\Omega} \quad (2.56)$$

$$\omega^2 = \frac{\int_{\Delta} \{\mathbf{H}_e^T [Q]^* \cdot \hat{\epsilon}^{-1} \cdot [Q] \mathbf{H}_e d\Omega}{\int_{\Delta} \mathbf{H}_e^T [N]^T \cdot \hat{\mu} \cdot ([N] \mathbf{H}_e) d\Omega} \quad (2.57)$$

The equation can be rearranged to write,

$$J_e = \int_{\Delta} \{\mathbf{H}_e^T [Q]^* \cdot \hat{\epsilon}^{-1} \cdot [Q] \mathbf{H}_e d\Omega - \omega^2 \int_{\Delta} \mathbf{H}_e^T [N]^T \cdot \hat{\mu} \cdot ([N] \mathbf{H}_e) d\Omega \quad (2.58)$$

here,  $\Delta$  represents the integration over the element. The total function  $J$  is for the entire cross-section of the waveguide and can be obtained by adding the  $J_e$  of all the elements.

$$J = \sum_{e=1}^n J_e \quad (2.59)$$

here  $n$  is the total number of elements.

Minimisation of the functional of equation 2.59 can be found by taking derivative of the function with respect to the nodal field values and equating it to zero as shown in the following equation,

$$\frac{\partial J}{\partial \{H\}_e} = 0 \quad (2.60)$$

this results in,

$$\int_{\Delta} \hat{\epsilon}^{-1} [Q]^* [Q] d\Omega \cdot \{H\} - \omega^2 \int_{\Delta} \hat{\mu} [N]^T [N] d\Omega \cdot \{H\}_e = 0 \quad (2.61)$$

---

the following eigenvalue equation is thus obtained,

$$[A]\{H\} - \omega^2[B]\{H\} = 0 \quad (2.62)$$

where, [A] and [B] are defined as follows,

$$[A] = \sum_{e=1}^n [A]_e = \sum_{e=1}^n \int_{\Delta} \frac{1}{\hat{\epsilon}} [Q]^* [Q] d\Omega \quad (2.63)$$

and,

$$[B] = \sum_{e=1}^n [B]_e = \sum_{e=1}^n \hat{\mu} \int_{\Delta} [N]^T [N] d\Omega \quad (2.64)$$

The matrix  $\{H\}$  contains all the  $\mathbf{H}$  field values of the nodes over the entire cross-section of the waveguide.  $[A]_e$  and  $[B]_e$  are the element matrices.

#### 2.2.1.4 Spurious Solution

In eigenvalue problem along with the physical solutions, some non-physical solutions can be found. For a physical solution the divergence  $\nabla \cdot \mathbf{H} = 0$  must be satisfied in the ideal case, but in numerical solutions, this divergence value should be a little value. For an eigenvector if it is found that the divergence value is too high, this indicates the corresponding solution is possibly a spurious solution and can be discarded.

### 2.2.2 Finite Difference Time Domain Method (FDTD)

FDTD algorithm starts with the time-dependent Maxwell's equation in differential form as given in the following four equations,

$$\frac{\partial \mathbf{B}}{\partial t} = -\nabla \times \mathbf{E} - \mathbf{M} \quad (2.65)$$

$$\frac{\partial \mathbf{D}}{\partial t} = -\nabla \times \mathbf{H} - \mathbf{J} \quad (2.66)$$

$$\nabla \cdot \mathbf{D} = 0 \quad (2.67)$$

---


$$\nabla \cdot \mathbf{B} = 0 \quad (2.68)$$

Here,

$\mathbf{E}$  : Electric Field

$\mathbf{D}$  : Electric Flux density

$\mathbf{H}$  : Magnetic Field

$\mathbf{B}$  : Magnetic Flux density

$\mathbf{J}$  : Electric Current

$\mathbf{M}$  : Equivalent Magnetic Current

For a linear, isotropic, non-dispersive material the following relationship holds,

$$\mathbf{D} = \epsilon \mathbf{E} = \epsilon_r \epsilon_0 \mathbf{E} \quad (2.69)$$

$$\mathbf{B} = \mu \mathbf{H} = \mu_r \mu_0 \mathbf{H} \quad (2.70)$$

Here,

$\epsilon$  : Electric permittivity

$\epsilon_r$  : Relative permittivity

$\epsilon_0$  : Permittivity of the free space,  $8.85 \times 10^{-12}$  Farads/meter

$\mu$  : Magnetic permeability

$\mu_r$  : Relative permeability,  $4\pi \times 10^{-7}$  H/m

$\mu_0$  : Permeability of free space

The electric current density is considered as the sum of the conduction current density and the source current density; the magnetic field density is considered to be the sum of the magnetic current density and the magnetic source and the relationships are given as,

$$\mathbf{J} = \mathbf{J}_{source} + \sigma \mathbf{E} \quad (2.71)$$

$$\mathbf{M} = \mathbf{M}_{source} + \sigma^* \mathbf{H} \quad (2.72)$$

here,

$\sigma$  : Electric Conductivity (Siemens/meter)

$\sigma^*$  : Equivalent Magnetic Conductivity (Ohms/meter)

---

Substituting these two equations into the Maxwell's curl equations gives us the following two equations,

$$\frac{\partial \mathbf{H}}{\partial t} = -\frac{1}{\mu} \nabla \times \mathbf{E} - \frac{1}{\mu} (\mathbf{M}_{source} + \sigma^* \mathbf{H}) \quad (2.73)$$

$$\frac{\partial \mathbf{E}}{\partial t} = -\frac{1}{\epsilon} \nabla \times \mathbf{H} - \frac{1}{\epsilon} (\mathbf{J}_{source} + \sigma \mathbf{E}) \quad (2.74)$$

By expanding the curl equations above we get,

$$\frac{\partial H_x}{\partial t} = \frac{1}{\mu} \left[ \frac{\partial E_y}{\partial z} - \frac{\partial E_z}{\partial y} - (M_{source x} + \sigma^* H_x) \right] \quad (2.75)$$

$$\frac{\partial H_y}{\partial t} = \frac{1}{\mu} \left[ \frac{\partial E_z}{\partial x} - \frac{\partial E_x}{\partial z} - (M_{source y} + \sigma^* H_y) \right] \quad (2.76)$$

$$\frac{\partial H_z}{\partial t} = \frac{1}{\mu} \left[ \frac{\partial E_x}{\partial y} - \frac{\partial E_y}{\partial x} - (M_{source z} + \sigma^* H_z) \right] \quad (2.77)$$

$$\frac{\partial E_x}{\partial t} = \frac{1}{\epsilon} \left[ \frac{\partial H_z}{\partial y} - \frac{\partial H_y}{\partial z} - (J_{source x} + \sigma E_x) \right] \quad (2.78)$$

$$\frac{\partial E_y}{\partial t} = \frac{1}{\epsilon} \left[ \frac{\partial H_x}{\partial z} - \frac{\partial H_z}{\partial x} - (J_{source y} + \sigma E_y) \right] \quad (2.79)$$

$$\frac{\partial E_z}{\partial t} = \frac{1}{\epsilon} \left[ \frac{\partial H_y}{\partial x} - \frac{\partial H_x}{\partial y} - (J_{source z} + \sigma E_z) \right] \quad (2.80)$$

The six coupled differential equations 2.75 - 2.80 work as the basis for the FDTD algorithm for EM wave propagation through different media in 3D.

### 2.2.3 FDTD algorithm

Yee's Algorithm is the most popular in implementing Maxwell's curl equation for solving both the electric and the magnetic field components in space and time. The arrangement of the  $\mathbf{E}$  and the  $\mathbf{H}$  field components are taken as shown in Fig. 2.6. Here each  $\mathbf{E}$  field component is surrounded by  $\mathbf{H}$  components and when two neighbouring cells are attached each  $\mathbf{H}$  field component is surrounded by  $\mathbf{E}$

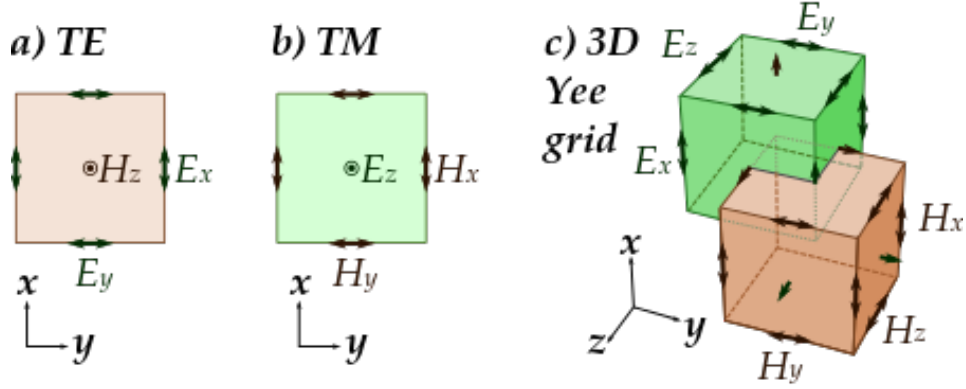


Figure 2.6: Yee's lattice source: wikipedia

components.

In this algorithm, the  $\mathbf{E}$  and the  $\mathbf{H}$  field components are placed in fact in two different grids staggered in space by half space steps. The algorithm evaluates the  $\mathbf{E}$  and the  $\mathbf{H}$  field components at alternate half-time steps. All the  $\mathbf{E}$  components in the modelled space are computed using the  $\mathbf{H}$  components stored in the memory from the previous computation. The magnetic components  $\mathbf{H}$  are then computed by the just computed  $\mathbf{E}$  components. The process is repeated until the time-stepping is concluded. The Fig. 2.7 illustrates the space-time steps of the algorithm in updating the field components.

The advantage of this algorithm is that the coupled equations form a system of equations that are fully explicit. That is why it is not required to solve a system of linear equations; the necessary computer memory and time is proportional to the computational domain.

The following notations for points in space and time has been assumed,

$$(i, j, k) = (i\Delta x, j\Delta y, k\Delta z) \quad (2.81)$$

$$u(i\Delta x, j\Delta y, k\Delta z, n\Delta t) = u_{i,j,k}^n \quad (2.82)$$

where  $\Delta x$ ,  $\Delta y$  and  $\Delta z$  are the space increments in  $x$ ,  $y$  and  $z$  directions respectively and  $i$ ,  $j$  and  $k$  are integers;  $\Delta t$  is the time increment and  $n$  is an

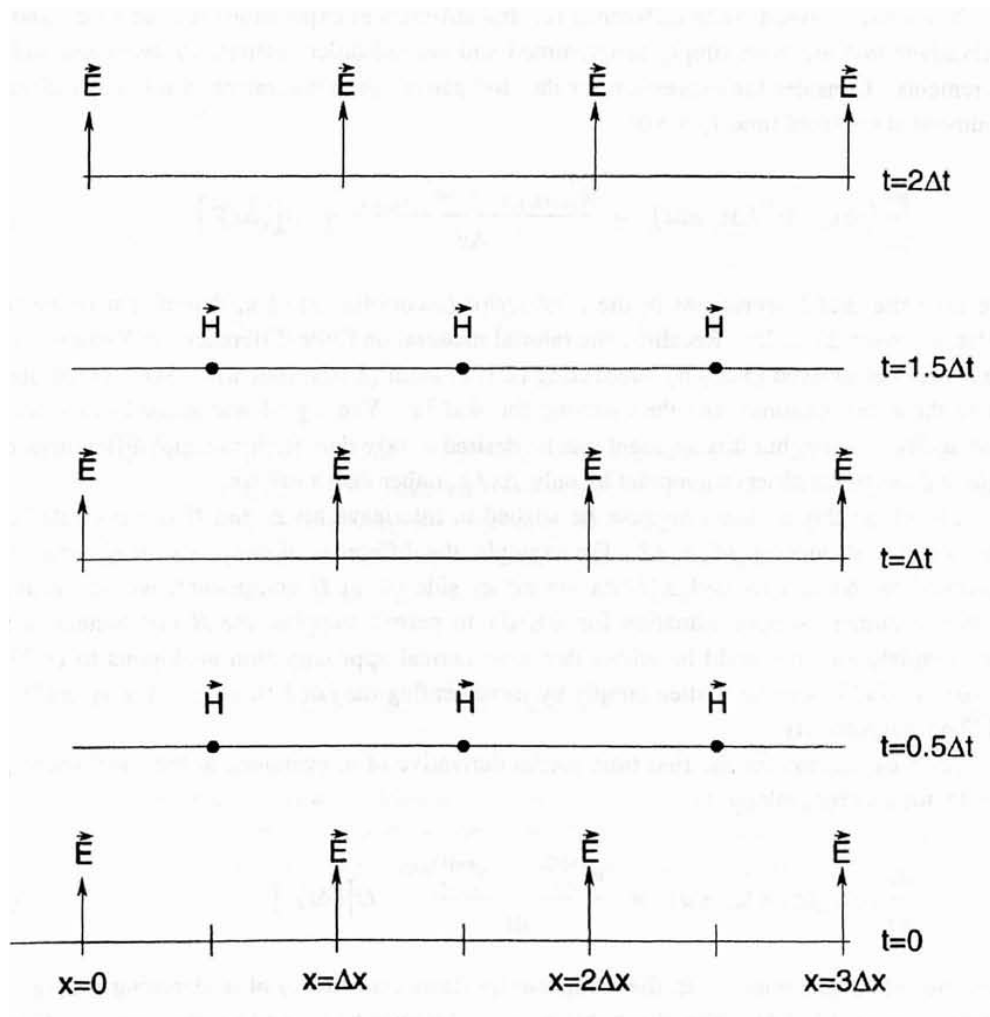


Figure 2.7: Space-time diagram for 1D wave propagation in FDTD, source: Taflove and Hagness [2005]

---

integer. The updating coefficients are given by the following equations. Updating coefficients - **E** field components at location  $(i, j, k)$

$$C_a \Big|_{i,j,k} = \left( 1 - \frac{\sigma_{i,j,k} \Delta t}{2\epsilon_{i,j,k}} \right) / \left( 1 + \frac{\sigma_{i,j,k} \Delta t}{2\epsilon_{i,j,k}} \right) \quad (2.83)$$

$$C_{b_1} \Big|_{i,j,k} = \left( \frac{\Delta t}{2\epsilon_{i,j,k} \Delta x} \right) / \left( 1 + \frac{\sigma_{i,j,k} \Delta t}{2\epsilon_{i,j,k}} \right) \quad (2.84)$$

$$C_{b_2} \Big|_{i,j,k} = \left( \frac{\Delta t}{2\epsilon_{i,j,k} \Delta y} \right) / \left( 1 + \frac{\sigma_{i,j,k} \Delta t}{2\epsilon_{i,j,k}} \right) \quad (2.85)$$

Updating coefficients - **H** field components at location  $(i, j, k)$

$$D_a \Big|_{i,j,k} = \left( 1 - \frac{\sigma_{i,j,k}^* \Delta t}{2\mu_{i,j,k}} \right) / \left( 1 + \frac{\sigma_{i,j,k}^* \Delta t}{2\mu_{i,j,k}} \right) \quad (2.86)$$

$$D_{b_1} \Big|_{i,j,k} = \left( \frac{\Delta t}{2\mu_{i,j,k} \Delta x} \right) / \left( 1 + \frac{\sigma_{i,j,k}^* \Delta t}{2\mu_{i,j,k}} \right) \quad (2.87)$$

$$D_{b_2} \Big|_{i,j,k} = \left( \frac{\Delta t}{2\mu_{i,j,k} \Delta y} \right) / \left( 1 + \frac{\sigma_{i,j,k}^* \Delta t}{2\mu_{i,j,k}} \right) \quad (2.88)$$

In case of a cubic lattice  $\Delta x = \Delta y = \Delta z$  and  $\Delta_1 = \Delta_2 = \Delta$  thus  $C_{b_1} = C_{b_2}$  and  $D_{b_1} = D_{b_2}$ . The finite Difference equations for space regions at particular time step for objects with distinct electrical and magnetic properties can be expressed as follows,

$$m = MEDIA_{E_x} \Big|_{i,j+1/2,k+1/2}$$

$$\begin{aligned} E_x \Big|_{i,j+1/2,k+1/2}^{n+1/2} &= C_a(m) E_x \Big|_{i,j+1/2,k+1/2}^{n+1/2} + C_b(m) \left[ H_z \Big|_{i,j+1,k+1/2}^n - H_z \Big|_{i,j,k+1/2}^n \right. \\ &\quad \left. + H_y \Big|_{i,j+1/2,k}^n - H_y \Big|_{i,j+1/2,k+1}^n - J_{source_x} \Big|_{i,j+1/2,k+1/2}^n \Delta \right] \end{aligned} \quad (2.89)$$

$$m = MEDIA_{E_y} \Big|_{i-1/2,j+1,k+1/2}$$

---


$$\begin{aligned}
E_y|_{i-1/2,j+1,k+1/2}^{n+1/2} &= C_a(m)E_y|_{i-1/2,j+1,k+1/2}^{n-1/2} + C_b(m)\left[H_x|_{i-1/2,j+1,k+1}^n - H_x|_{i-1/2,j+1,k}^n\right. \\
&\quad \left.+ H_z|_{i-1,j+1,k+1/2}^n - H_z|_{i,j+1/2,k+1}^n - J_{source_y}|_{i-1/2,j+1/2,k+1/2}^n \Delta\right] \quad (2.90)
\end{aligned}$$

$$m = MEDIA_{E_z|_{i-1/2,j+1/2,k+1}}$$

$$\begin{aligned}
E_z|_{i-1/2,j+1/2,k+1}^{n+1/2} &= C_a(m)E_z|_{i-1/2,j+1/2,k+1}^{n-1/2} + C_b(m)\left[H_y|_{i,j+1/2,k+1}^n - H_y|_{i-1,j+1/2,k+1}^n\right. \\
&\quad \left.+ H_x|_{i-1/2,j,k+1}^n - H_x|_{i-1/2,j+1,k+1}^n - J_{source_z}|_{i-1/2,j+1/2,k+1}^n \Delta\right] \quad (2.91)
\end{aligned}$$

$$m = MEDIA_{H_x|_{i-1/2,j+1/2,k+1}}$$

$$\begin{aligned}
H_x|_{i-1/2,j+1,k+1}^{n+1} &= D_a(m)H_x|_{i-1/2,j+1,k+1}^n + D_b(m)\left[E_y|_{i-1/2,j+1/2,k+3/2}^{n+1/2} - E_y|_{i-1/2,j+1,k+1/2}^{n+1/2}\right. \\
&\quad \left.+ E_z|_{i-1/2,j+3/2,k+1}^{n+1/2} - E_z|_{i-1/2,j+3/2,k+1}^{n+1/2} - M_{source_x}|_{i-1/2,j+1,k+1}^{n+1/2} \Delta\right] \quad (2.92)
\end{aligned}$$

$$m = MEDIA_{H_y|_{i-1/2,j+1/2,k+1}}$$

$$\begin{aligned}
H_y|_{i,j+1/2,k+1}^{n+1} &= D_a(m)H_y|_{i,j+1/2,k+1}^n + D_b(m)\left[E_z|_{i+1/2,j+1/2,k+1}^{n+1/2} - E_z|_{i-1/2,j+1/2,k+1}^{n+1/2}\right. \\
&\quad \left.+ E_x|_{i,j+1/2,k+1/2}^{n+1/2} - E_x|_{i,j+1/2,k+3/2}^{n+1/2} - M_{source_y}|_{i,j+1/2,k+1}^{n+1/2} \Delta\right] \quad (2.93)
\end{aligned}$$

$$m = MEDIA_{H_z|_{i-1/2,j+1/2,k+1}}$$

---


$$\begin{aligned}
H_z \Big|_{i,j+1,k+1/2}^{n+1} &= D_a(m) H_z \Big|_{i,j+1,k+1/2}^n + D_b(m) \left[ E_x \Big|_{i,j+3/2,k+1/2}^{n+1/2} - E_x \Big|_{i,j+1/2,k+1/2}^{n+1/2} \right. \\
&\quad \left. + E_y \Big|_{i-1/2,j+1,k+1/2}^{n+1/2} - E_y \Big|_{i+1/2,j+1,k+1/2}^{n+1/2} - M_{source_z} \Big|_{i,j+1,k+1/2}^{n+1/2} \Delta \right] \quad (2.94)
\end{aligned}$$

where,  $MEDIA(i, j, k)$  is an integer array for each vector field components. The following indexing scheme is used in the algorithm,

$$E_x \Big|_{i+1/2,j,k}^n, \quad i = 1, \dots, N_x, \quad j = 1, \dots, N_y + 1, \quad k = 1, \dots, N_z + 1 \quad (2.95)$$

$$E_y \Big|_{i,j+1/2,k}^n, \quad i = 1, \dots, N_x + 1, \quad j = 1, \dots, N_y, \quad k = 1, \dots, N_z + 1 \quad (2.96)$$

$$E_z \Big|_{i,j,k+1/2}^n, \quad i = 1, \dots, N_x + 1, \quad j = 1, \dots, N_y + 1, \quad k = 1, \dots, N_z \quad (2.97)$$

$$H_x \Big|_{i+1/2,j,k}^{n-1/2}, \quad i = 1, \dots, N_x + 1, \quad j = 1, \dots, N_y, \quad k = 1, \dots, N_z \quad (2.98)$$

$$H_y \Big|_{i,j+1/2,k}^{n-1/2}, \quad i = 1, \dots, N_x, \quad j = 1, \dots, N_y + 1, \quad k = 1, \dots, N_z \quad (2.99)$$

$$H_z \Big|_{i,j,k+1/2}^{n-1/2}, \quad i = 1, \dots, N_x, \quad j = 1, \dots, N_y, \quad k = 1, \dots, N_z + 1 \quad (2.100)$$

Where, for example  $H_x \Big|_{i,j+1/2,k+1/2}^{n-1/2}$  is located at  $((i-1)\Delta x, (j-1/2)\Delta y, (k-1/2)\Delta z)$  space point and  $t = (n-1/2)\Delta t$ .

---

## 2.2.4 Numerical Stability

There is a limit on the time step,  $\Delta t$  in ensuring the stability of the algorithm, where the choice of  $\Delta t$  is given by,

$$\Delta t \leq \frac{1}{c\sqrt{\frac{1}{(\Delta x)^2} + \frac{1}{(\Delta y)^2} + \frac{1}{(\Delta z)^2}}} \quad (2.101)$$

where  $c$  is the propagation speed of the wave. Hence the Courant factor is defined as,

$$S = c.\Delta t\sqrt{\frac{1}{(\Delta x)^2} + \frac{1}{(\Delta y)^2} + \frac{1}{(\Delta z)^2}} \quad (2.102)$$

and the stability condition is,

$$S < 1 \quad (2.103)$$

## 2.3 Perfectly Matched Layer (PML)

An essential consideration in applying FDTD method to solve Electromagnetic field the problem is that the domain is considered to be open. However, as the computer storage is limited, it is not, however, possible to solve the problem with unlimited computational domain. The computational domain is taken large enough so that the region of interest lies within the computational domain. As a consequence of taking a finite computational domain is that from the boundary of the computational domain we get numerical wave reflection to satisfy the boundary conditions. The solution obtained thus is affected by the artificial reflected waves generated from the computational limit. To address this problem, several techniques are being used such as the absorbing boundary condition (ABC) introduced by [Mur \[1981\]](#). One of the most popular and efficient ways to limit the computational domain is introducing perfectly matched layer (PML) introduced by [Berenger \[1994\]](#). The PML matches the propagating wave to cancel reflections from the computational boundary.

The finite difference system of equation of Maxwell's equation presented before in 3D can be reduces to 2D; Transverse Magnetic mode with respect to  $z$   $TM_z$

---

with  $E_z$ ,  $H_x$ , and  $H_y$  field components; Transverse Electric mode with respect to  $z$   $TE_z$  with  $H_z$ ,  $E_x$ , and  $E_y$  field components; assuming  $\frac{\partial}{\partial z} \rightarrow 0$ . The updating equations for 2D  $TM_z$  case are,

$$\epsilon_0 \frac{\partial E_{zx}}{\partial t} + \sigma_x E_{zx} = \frac{\partial E_y}{\partial x} \quad (2.104)$$

$$\epsilon_0 \frac{\partial E_{zy}}{\partial t} + \sigma_y E_{zy} = -\frac{\partial H_x}{\partial y} \quad (2.105)$$

$$\mu_0 \frac{\partial H_x}{\partial t} + \sigma_y^* H_x = \frac{\partial (E_{zx} - E_{zy})}{\partial y} \quad (2.106)$$

$$\mu_0 \frac{\partial H_y}{\partial t} + \sigma_x^* H_y = \frac{\partial (E_{zx} + E_{zy})}{\partial x} \quad (2.107)$$

and,

$$E_{zx} = E_z + E_x \quad (2.108)$$

$$E_{zy} = E_z + E_y \quad (2.109)$$

Based on the Fig. 2.8, the eight regions and the PML defined in each region are as follows,

1. PML( $\sigma_{x1}, \sigma_{x1}^*, \sigma_{y2}, \sigma_{y2}^*$ )
2. PML( $0, 0, \sigma_{y2}, \sigma_{y2}^*$ )
3. PML( $\sigma_{x2}, \sigma_{x2}^*, \sigma_{y2}, \sigma_{y2}^*$ )
4. PML( $\sigma_{x1}, \sigma_{x1}^*, 0, 0$ )
5. PML( $\sigma_{x2}, \sigma_{x2}^*, 0, 0$ )
6. PML( $\sigma_{x1}, \sigma_{x1}^*, \sigma_{y1}, \sigma_{y1}^*$ )
7. PML( $0, 0, \sigma_{y1}, \sigma_{y1}^*$ )
8. PML( $\sigma_{x1}, \sigma_{x1}^*, \sigma_{y1}, \sigma_{y1}^*$ )

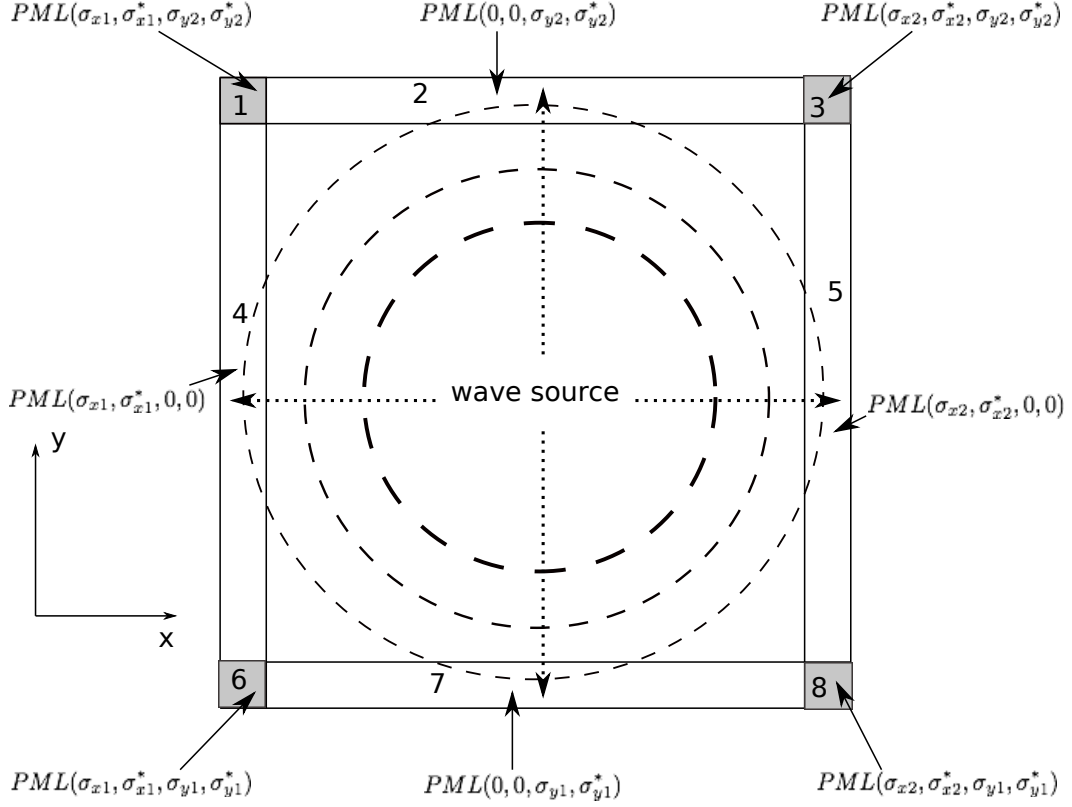


Figure 2.8: Structure of a 2D PML

The PML reflection factor is given by,

$$R(\theta) = e^{-2\eta\sigma_{x,0}\Delta(g^{d/\Delta}-1)\cos\theta/\ln g} \quad (2.110)$$

where,  $g$  is a scaling factor,  $d$  is the thickness of the PML medium,  $\Delta$  is the space increment,  $\eta = \sqrt{\mu_1/\epsilon_1}$  and the  $\theta$  is the angle of incidence relative to the wave-directed surface normal. The equation above can be rearranged to get,

$$\sigma_{x,0} = -\frac{\ln[R(0)]\ln(g)}{2\eta\Delta(g^{d/\Delta}-1)} \quad (2.111)$$

where, for  $d = 10$ ,  $R(0) = 10^{-16}$ , and  $2 \leq g \leq 3$  is found to be optimal choice.

---

### 2.3.1 Uniaxial PML Implementation

A two-step procedure is employed to update the components of  $\mathbf{E}$  and  $\mathbf{H}$  field components in implementing Uniaxial PML (UPML) presented by [Taflove and Hagness \[2005\]](#). Coefficients are updated first and they are used to compute the field components in the PML. For the electric field, the  $D_x$  coefficient is as follows,

$$D_x \Big|_{i+1/2,j,k}^{n+1} = \left( \frac{2\epsilon\kappa_y - \sigma_y\Delta t}{2\epsilon\kappa_y + \sigma_y\Delta t} \right) D_x \Big|_{i+1/2,j,k}^n + \left( \frac{2\epsilon\Delta t}{2\epsilon\kappa_y + \sigma_y\Delta t} \right) \left( \frac{H_z \Big|_{i+1/2,j+1/2,k}^{n+1/2} - H_z \Big|_{i+1/2,j-1/2,k}^{n+1/2}}{\Delta y} - \frac{H_y \Big|_{i+1/2,j+1/2,k}^{n+1/2} - H_y \Big|_{i+1/2,j-1/2,k}^{n+1/2}}{\Delta z} \right) \quad (2.112)$$

The  $E_x$  is given by,

$$E_x \Big|_{i+1/2,j,k}^{n+1} = \left( \frac{2\epsilon\kappa_y - \sigma_y\Delta t}{2\epsilon\kappa_y + \sigma_y\Delta t} \right) E_x \Big|_{i+1/2,j,k}^n + \left( \frac{1}{\epsilon(2\epsilon\kappa_z + \sigma_z\Delta t)} \right) \left[ (2\epsilon\kappa_x + \sigma_x\Delta t) D_x \Big|_{i+1/2,j,k}^{n+1} - (2\epsilon\kappa_x + \sigma_x\Delta t) D_x \Big|_{i+1/2,j,k}^n \right] \quad (2.113)$$

$B_x$  coefficient is given by,

$$B_x \Big|_{i,j+1/2,k+1/2}^{n+3/2} = \left( \frac{2\epsilon\kappa_y - \sigma_y\Delta t}{2\epsilon\kappa_y + \sigma_y\Delta t} \right) B_x \Big|_{i,j+1/2,k+1/2}^{n+1/2} + \left( \frac{2\epsilon\Delta t}{2\epsilon\kappa_y + \sigma_y\Delta t} \right) \left( \frac{E_z \Big|_{i,j+1,k+1/2}^{n+1} - E_z \Big|_{i,j,k+1/2}^{n+1/2}}{\Delta y} - \frac{E_y \Big|_{i,j+1/2,k+1}^{n+1} - E_y \Big|_{i,j+1/2,k}^{n+1}}{\Delta z} \right) \quad (2.114)$$

Updating the  $H_x$  component is updated as follows,

$$H_x \Big|_{i,j+1/2,k+1/2}^{n+3/2} = \left( \frac{2\epsilon\kappa_z - \sigma_z\Delta t}{2\epsilon\kappa_z + \sigma_z\Delta t} \right) H_x \Big|_{i+1/2,j,k+1/2}^{n+1/2} + \left( \frac{1}{\epsilon(2\epsilon\kappa_x + \sigma_x\Delta t)} \right) \left[ (2\epsilon\kappa_x + \sigma_x\Delta t) B_x \Big|_{i,j+1/2,k+1/2}^{n+3/2} - (2\epsilon\kappa_x + \sigma_x\Delta t) B_x \Big|_{i,j+1/2,k+1/2}^{n+1/2} \right] \quad (2.115)$$

---

the other field components  $E_y$ ,  $E_z$ ,  $H_y$  and  $H_z$  can be updated in a similar way.

## 2.4 Diffraction

### 2.4.1 Kirchoff's Diffraction Integral

Kirchoff's diffraction integral solves the homogeneous wave equation (Helmholtz equation) at an arbitrary point  $P$  in terms of the solution of the wave equation and its first order derivative at all points on a surface that encloses  $P$ . The geometric arrangements for deriving Kirchoff's diffraction integral is shown in Fig. 2.9. Here, the point source is  $P_0$ ,  $P$  is the point at which we wish to determine the field intensity,  $A_1$  is the aperture,  $A_1 - A_2 - A_3$  constitute the surface that encloses  $P$ ,  $r$  is the distance between the point source and any point  $Q$  on  $A_1$ ,  $s$  is the distance between  $Q$  and  $P$ ,  $n$  is the normal unit vector to the surface  $A_1$  and  $j = \sqrt{-1}$ . The solution provided by the Integral theorem for a monochromatic wave can be written as,

$$U(P) = -\frac{1}{4\pi} \int_S \left[ U \frac{\partial}{\partial n} \left( \frac{e^{jks}}{s} \right) - \frac{e^{jks}}{s} \frac{\partial U}{\partial n} \right] dS \quad (2.116)$$

here,  $k = \frac{2\pi}{\lambda}$  is the wave vector,  $\lambda$  is the operating wavelength, and  $S$  is the surface of  $A_1$ . The following assumptions are made,

- $U$  and  $\frac{\partial U}{\partial n}$  are discontinuous at the boundary of the aperture
- $r$  and  $s$  are much higher than  $\lambda$

The assumption,  $U$  and  $\frac{\partial U}{\partial n}$  are discontinuous at the boundary of the aperture, requires  $U$  and  $\frac{\partial U}{\partial n}$  to be zero in  $A_2$ . The contribution from  $A_3$  is considered zero as well. For most of the possible geometries, these assumptions are not true, That is why this integral is mathematically inconsistent. However, if  $A_3$  is positioned far away from  $P$  and  $1/r$  and  $1/s$  are negligible compared to  $k$ , the integral provides us with reasonably accurate results. If we assume that a point

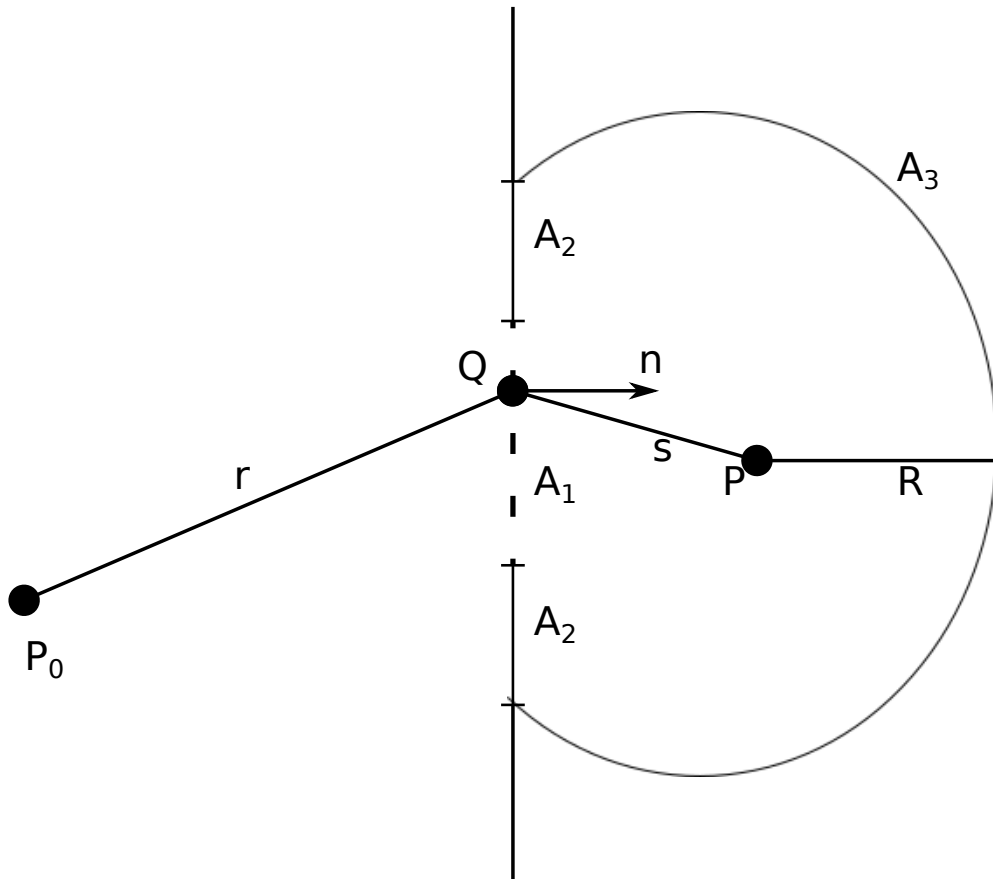


Figure 2.9: Geometric arrangements for Kirchhoff's diffraction integral

source is placed at point  $P_0$  described by the following equation,

$$U(r) = \frac{ae^{jkr}}{r} \quad (2.117)$$

here,  $a$  is the amplitude of the point source. After simplification the integral can be written as,

$$U(P) = -\frac{ia}{2\lambda} \int_S \frac{e^{jk(r+s)}}{rs} [\cos(n, r) - \cos(n, s)] dS \quad (2.118)$$

where,  $(n, r)$  and  $(n, s)$  are the angles between  $\mathbf{n}$  and  $\mathbf{P}_0\mathbf{Q}$ ,  $\mathbf{PQ}$  vectors respectively. This integral can be computed by using numerical integration, i.e. Simpson's 1/3rd rule.

## 2.4.2 Rayleigh-Sommerfeld Diffraction Integral

Figure 2.10 shows the geometric arrangements for evaluating the Rayleigh-Sommerfeld diffraction integral. It is assumed that an aperture is present at  $z = 0$  plane and it is illuminated by a point source placed far away from it,  $U_0(x, y, z)$  is the incident wavefront from the point source,  $\Omega$  refers to the area of the aperture,  $r_0$  is the position vector of a point on the aperture, a screen is located at  $z = z_0$  plane,  $r$  is the position vector of a point located on the screen with the coordinates  $(x_0, y_0, z_0)$ .

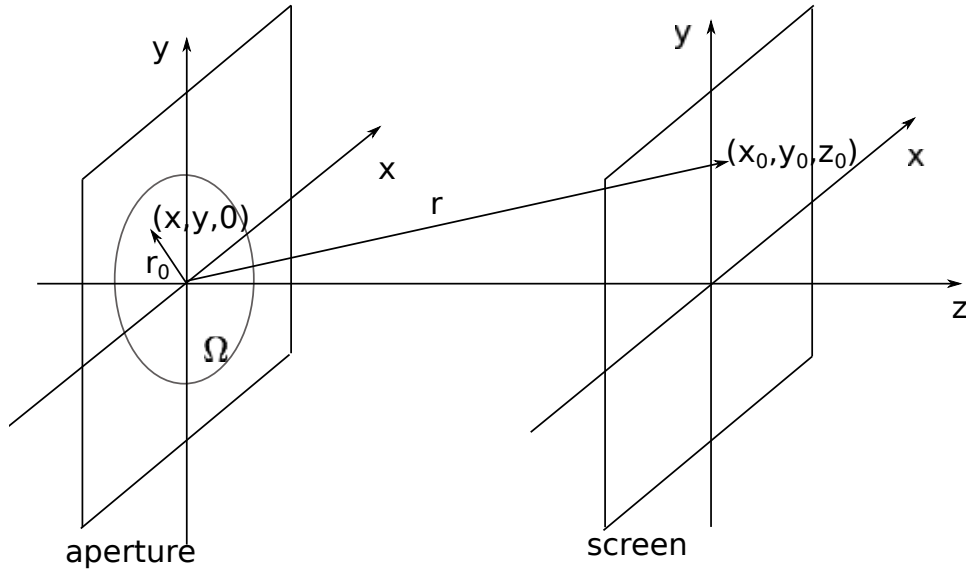


Figure 2.10: Geometric arrangements for evaluating RS diffraction formula

The following assumptions are made,

- On the aperture  $U_0(x, y, 0) = U(x, y, 0)$
- Outside the aperture on the aperture screen,  $U(x, y, 0) = 0$

---

The Rayleigh-Somerfeld diffraction integral is now given by the following equation,

$$U(x_0, y_0, z_0) = - \int \int_{\Omega} U(x, y, 0) \frac{2z_0}{|\bar{r}_0 - \bar{r}|} \left( jk - \frac{1}{|\bar{r}_0 - \bar{r}|} \right) \frac{\exp(jk|\bar{r}_0 - \bar{r}|)}{4\pi|\bar{r}_0 - \bar{r}|} dx dy \quad (2.119)$$

This equation can be computed by numerical integration techniques.

## 2.5 Summary

This Chapter provides a comprehensive description of the computational tools used in this thesis. As the Maxwell's equations can characterise the light (Electromagnetic wave), at the beginning this Chapter the Maxwell's equations in the differential form are provided. A comprehensive description of the formulation of **H**-field based finite element method is presented next. The various aspects of the formulation, i.e. Discretisation, Shape function, Formation of Element and Global matrices, Boundary conditions, and the eliminations of spurious modes have been presented. Finite Difference Time Domain (FDTD) method used to study the time evolution of the signals is presented then. The criteria for numerical stability of the algorithm and the implementation strategy of a Perfectly Matched Layer (PML) is also discussed. Finally, the diffraction integral is described. This Chapter thus serves as the computational foundations for the tools used in this thesis.

# Chapter 3

## Simulation of the Visual System

### 3.1 Planar Structure

For a planar waveguide, it is considered that the core material is sandwiched between the cladding material and it is assumed that the structure is infinitely extended in the  $y$  direction as shown in Fig. 3.1. The core material width along  $x$  direction is assumed as  $d$  and the direction of propagation is considered to be in the  $z$  direction. The core has a refractive index of  $n_1$  and both the upper and lower cladding have refractive index of  $n_2$ , where  $n_1 > n_2$ .

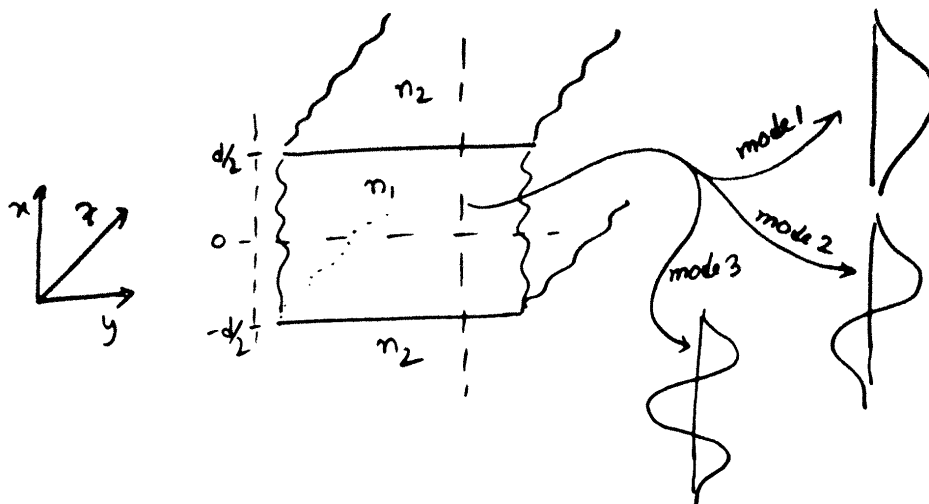


Figure 3.1: Planar Waveguide Schematics

---

A typical field profile for a Planar waveguide guide ( $x$  vs.  $\beta z$ ) and the RAY optics analogy is shown in Fig. 3.2. Here the RAY direction is assumed as the normal to the wavefront,  $\bar{k}$  is the wave vector normal to the wavefront,  $\bar{k}_z$  is the wave vector component along z-axis,  $\bar{k}_x$  is the wave vector component along x-axis, and  $\theta$  is the angle made by the RAY with the normal of the core-cladding interface.

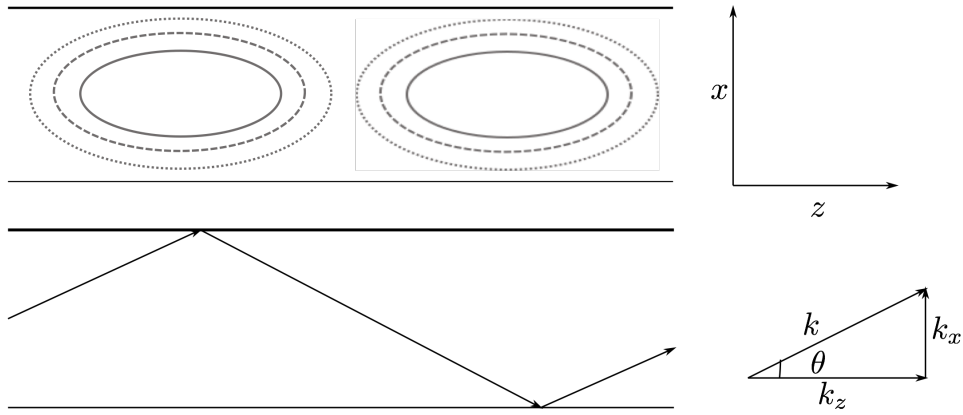


Figure 3.2: Planar Field profiles at XZ plane for TE

here,

$$k_z = k_1 \sin \theta$$

$$n_{eff} = n_1 \sin \theta$$

and

$$k_z = \beta$$

the angle  $\theta$  can be defined by Eq. 3.1.

$$\theta = \sin^{-1} \frac{n_{eff}}{n_1} \quad (3.1)$$

Effective index,  $n_{eff}$  is a critical parameter in describing the characteristics of the propagating mode. An increase in the effective index  $n_{eff}$  means the mode is more confined to the core with the refractive index  $n_1$  and it also means that the mode makes a smaller angle with the axis of the core ( $\theta$  approaches  $90^\circ$ ).

Table 3.1: Relationship between confinement factor and  $n_{eff}$

| $n_{eff}$ | Confinement                        |
|-----------|------------------------------------|
| $n_1$     | 100% field is confined in the core |
| $n_2$     | 0% field is confined in the core   |

Lower order modes have higher  $n_{eff}$ , means, more confinement, the lowest order mode or the fundamental mode have the highest  $n_{eff}$ . The confinement factor is defined as,

$$C_f = \frac{\text{Power in the core}}{\text{Total mode power}} \quad (3.2)$$

The higher order modes have subsequently lower  $n_{eff}$  with lower confinement factor. For a mode whose incident angle satisfies the condition  $\theta \geq \theta_c$ , is no longer guided by the core, where the  $\theta_c$  is the critical angle at the  $n_1 - n_2$  interface that is defined by

$$\theta_c = \sin^{-1} \frac{n_2}{n_1} \quad (3.3)$$

here the symbol  $n_1$  and  $n_2$  have their usual meaning and  $n_1 > n_2$  is assumed. If  $n_{eff} \approx n_1$ , the  $\theta \approx 90^\circ$ , is the case when the propagation vector  $\mathbf{k}$  makes a very small angle to the guide axis (z- axis in the current case).

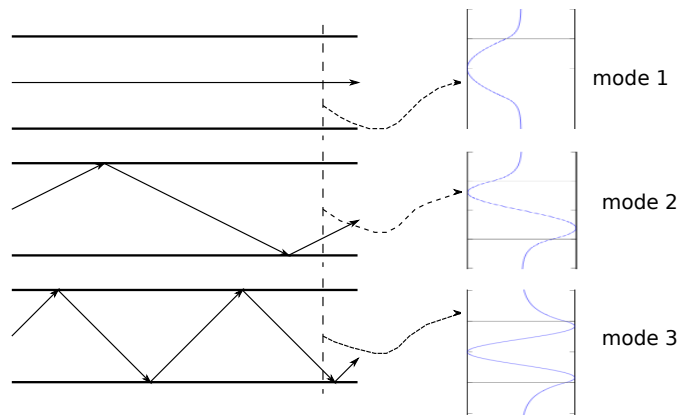


Figure 3.3: Propagation angle and the corresponding field profiles

Figure 3.3 shows that the higher mode angle corresponds to a higher order

---

mode. The relationship between the mode angle ( $\theta$ ) and the propagating modes can be found in Table 3.3 and in Fig. 3.4.

For the Maxwell's equation in the planar structure, we assume the  $\frac{\partial}{\partial y} \rightarrow 0$ , that means the structure is infinitely extended in the y direction and no field variation along y. This assumption breaks the Maxwell's equation into two separate sets,

| TE                            | TM                            |
|-------------------------------|-------------------------------|
| non-zero $E_y, H_x$ and $H_z$ | non-zero $H_y, E_x$ and $E_z$ |

Table 3.2: TE and TM modes with their respective field components

One set with no electric field component in the direction of propagation (z), known as the Transverse Electric (TE) wave and another set with no magnetic field components in the z direction, known as the Transverse Magnetic (TM) wave.

For TE polarization,

$$\bar{\mathbf{E}} = \hat{y}E_y$$

and

$$\bar{\mathbf{H}} = \hat{x}H_x + \hat{z}H_z$$

The power flow,  $\bar{\mathbf{P}}$  is defined as the cross-product of the electric field  $\bar{\mathbf{E}}$  and the magnetic field  $\bar{\mathbf{H}}$  that is given as,

$$\bar{\mathbf{P}} = \bar{\mathbf{E}} \times \bar{\mathbf{H}} \tag{3.4}$$

$$= \begin{pmatrix} \hat{x} & \hat{y} & \hat{z} \\ 0 & E_y & 0 \\ H_x & 0 & H_z \end{pmatrix} \tag{3.5}$$

$$\bar{\mathbf{P}} = -\hat{x}E_yH_x + \hat{z}E_yH_z \tag{3.6}$$

---

propagating in the XZ plane, the  $\bar{\mathbf{P}}$  making an angle  $\theta$  with the z axis where,

$$\tan \theta = \frac{H_z}{H_x} \quad (3.7)$$

in order to keep the angle  $\theta$  small, the  $H_x$  should be the dominant field component.

For TM polarization,

$$\bar{\mathbf{E}} = \hat{x}E_x + \hat{z}E_z$$

and

$$\bar{\mathbf{H}} = \hat{x}H_y$$

$$\bar{\mathbf{P}} = \bar{\mathbf{E}} \times \bar{\mathbf{H}} \quad (3.8)$$

$$= \begin{pmatrix} \hat{x} & \hat{y} & \hat{z} \\ E_x & 0 & E_z \\ 0 & H_y & 0 \end{pmatrix} \quad (3.9)$$

$$\bar{\mathbf{P}} = \hat{x}H_yE_z - \hat{z}H_yE_x \quad (3.10)$$

propagating in the XZ plane, the  $\bar{\mathbf{P}}$  making an angle  $\theta$  with the z axis where,

$$\tan \theta = \frac{E_z}{E_x} \quad (3.11)$$

in order to keep the angle  $\theta$  small, the  $E_x$  should be the dominant field component. When a plane wave is reflected from a dielectric-dielectric interface, it experiences a phase change  $\phi$  that is given by,

$$\phi_{12} = \sqrt{\frac{1 - \left(\frac{n_2}{n_1}\right)^2}{\sin^2\theta}} \quad \text{for TE} \quad (3.12)$$

$$\phi_{12} = \left(\frac{n_1}{n_2}\right)^2 \sqrt{\frac{1 - \left(\frac{n_2}{n_1}\right)^2}{\sin^2\theta}} \quad \text{for TM} \quad (3.13)$$

---

A RAY that propagates at an angle  $\theta$  with the  $z$  axis, forms standing wave profiles or the mode profiles along the  $x$  direction if it satisfies the following condition,

$$2k_0n_1d \sin \theta - 2\phi_{12} - 2\phi_{13} = 2m\pi \quad (3.14)$$

where,

$k_0 = \frac{2\pi}{\lambda}$  is the free space propagation constant

$\lambda$  : free space wavelength

$n_1$  : core refractive index

$\phi_{12}$  : phase change at the 1-2 interface due to reflection

$\phi_{13}$  : phase change at the 1-3 interface due to reflection

$m$  : mode number

$d$  : guide thickness along  $x$  direction

Assuming a symmetric structure with  $n_1 = n_3$  the equation takes the following form,

$$k_0n_1d \sin \theta = 2\sqrt{\frac{1 - \left(\frac{n_2}{n_1}\right)^2}{\sin^2\theta}} + m\pi \quad \text{for TE} \quad (3.15)$$

$$k_0n_1d \sin \theta = \left(\frac{n_1}{n_2}\right)^2 \sqrt{\frac{1 - \left(\frac{n_2}{n_1}\right)^2}{\sin^2\theta}} + m\pi \quad \text{for TM} \quad (3.16)$$

The equations can be solved numerically for  $\theta$  using Newton-Raphson method, the Table 3.3 shows different values of the values for TE polarisation. Figure 3.4 displays the mode angle ( $\theta$ ) against the normalised height ( $d/\lambda$ ) for the first few supported modes of the planar waveguide for TE polarisation. The planar waveguide structure as shown in Fig. 3.1 is used for these calculations.

Table 3.3: Mode angles for various normalised heights ( $d/\lambda$ ) of a Planar waveguide,  $NA = 0.15$

| $d/\lambda$ | mode 1 | mode 2 | mode 3 | mode 4 | mode 5 |
|-------------|--------|--------|--------|--------|--------|
| 0.50        | 53.73  | –      | –      | –      | –      |
| 0.75        | 33.81  | –      | –      | –      | –      |
| 1.00        | 25.52  | 50.85  | –      | –      | –      |
| 1.25        | 20.79  | 38.81  | 65.98  | –      | –      |
| 1.50        | 17.69  | 31.83  | 49.89  | –      | –      |
| 1.75        | 15.49  | 27.15  | 41.20  | 59.93  | –      |
| 2.00        | 13.84  | 23.77  | 35.38  | 49.40  | 70.33  |
| 2.50        | 11.53  | 19.16  | 27.87  | 37.64  | 49.11  |
| 3.00        | 9.97   | 16.15  | 23.14  | 30.78  | 39.21  |
| 3.50        | 8.84   | 14.03  | 19.86  | 26.16  | 32.94  |
| 4.00        | 7.99   | 12.44  | 17.45  | 22.81  | 28.52  |

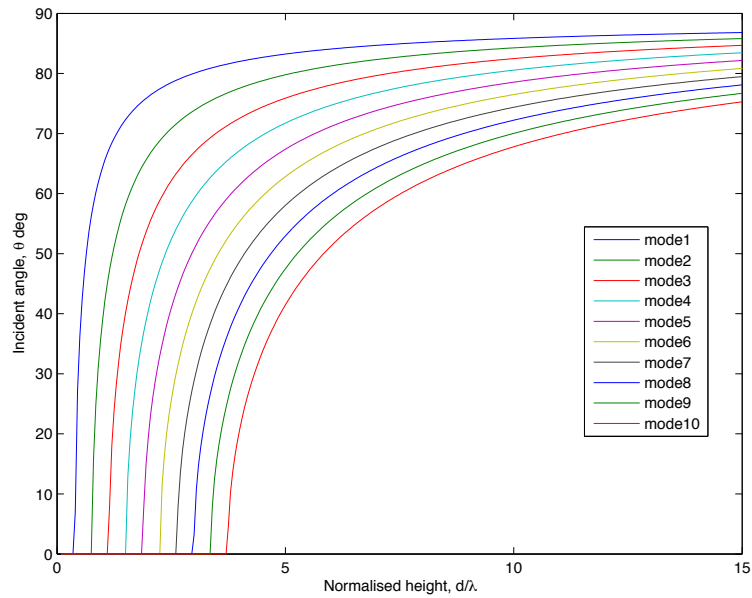


Figure 3.4: Mode angles vs normalised height ( $d/\lambda$ ) of a Planar waveguide,  $NA = 0.15$

---

### Helmholtz equation

We assume propagation as  $e^{-j\beta z}$  in the z direction, and if  $\frac{\partial}{\partial y} \rightarrow 0$ , the solution breaks into TE and TM type. For TE polarization, the Helmholtz equation for  $E_y$  can be written as,

$$\frac{d^2 E_{yi}}{dx^2} = (\beta^2 - k_i^2), \quad i = 1, 2, 3 \quad (3.17)$$

here,  $i$  representing the layers,  $k_i = \frac{2\pi}{\lambda} n_i$  is the propagation constant in the  $i$  th medium, and  $\beta = \frac{2\pi}{\lambda} n_{eff}$ . The solution of equation 3.17 is exponential or sinusoidal depending upon the parameter  $\beta^2 - k_i^2$  is positive or negative respectfully. As we are considering the medium 1 as the guiding medium,  $k_1 < \beta$ . In the upper and lower cladding  $\beta > k_1$  and  $\beta > k_3$  must be true. The solutions in region 2 and region 3 must be exponentially decreasing and in region 1 (core) it should be sinusoid. From  $E_y$ , the other two components  $H_x$  and  $H_z$  can be determined using the Maxwell's equation,

$$\nabla \times \mathbf{E} = -j\omega\mu\mathbf{H} \quad (3.18)$$

In layer 2,

$$\left. \begin{aligned} E_{y2} &= Ae^{-qx} \\ H_{x2} &= -\frac{\beta}{\omega\mu} Ae^{-qx} \\ H_{z2} &= \frac{q}{j\omega\mu} Ae^{-qx} \end{aligned} \right\} x > d/2 \quad (3.19)$$

in layer 1,

$$\left. \begin{aligned} E_{y1} &= B \cos hx + C \sin hx \\ H_{x1} &= -\frac{\beta}{\omega\mu} [B \cos hx + C \sin hx] \\ H_{z1} &= \frac{h}{j\omega\mu} [B \sin hx - C \cos hx] \end{aligned} \right\} -d/2 \leq x \leq d/2 \quad (3.20)$$

---

in layer 3,

$$\left. \begin{aligned} E_{y3} &= De^{px} \\ H_{x3} &= -\frac{\beta}{\omega\mu}De^{px} \\ H_{z3} &= \frac{p}{j\omega\mu}De^{px} \end{aligned} \right\} x < -d/2 \quad (3.21)$$

here,  $q^2 = \beta^2 - k_2^2$ ,  $h^2 = k_1^2 - \beta^2$  and  $p^2 = \beta^2 - k_3^2$ . The tangential components of Electric and Magnetic fields must be continuous at the interfaces  $x = d/2$  and  $x = -d/2$ . By applying the continuity conditions the coefficients  $A$ ,  $B$ ,  $C$  and  $D$  can be eliminated to get the following transcendental equation for a symmetric mode and  $n_2 = n_3$ ,

$$\frac{hd}{2} \tan \frac{hd}{2} = \frac{qd}{2} \quad (3.22)$$

The equation can be solved graphically to get  $h$  and  $q$ , hence the  $\beta$  can be found. To plot the propagation characteristics, the following definitions are used, the normalised frequency,

$$V = \frac{\pi d}{\lambda} \sqrt{n_1^2 - n_2^2} \quad (3.23)$$

the normalised propagation constant,

$$b = \frac{n_{eff}^2 - n_2^2}{n_1^2 - n_2^2} \quad (3.24)$$

and the effective index is given by,

$$n_{eff} = \frac{\beta}{k_0} \quad (3.25)$$

The  $qd/2$  vs.  $hd/2$  curves have been plotted in Fig. 3.5, where the green lines are for the symmetric and the red ones are for the antisymmetric modes. Intersections between the circle having the radius of  $V$  and the  $qd/2$  vs  $hd/2$  curves based on equation 3.22 gives us the  $n_{eff}$  values of the supported modes.

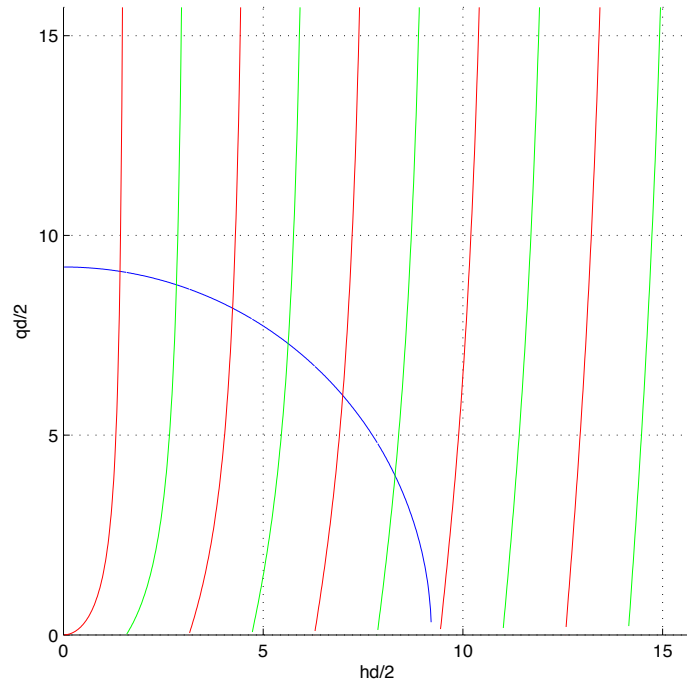


Figure 3.5:  $qd/2$  vs  $hd/2$  curves for the detrimental equation of planar structure,  $d = 2\mu m$ ,  $NA = 0.15$

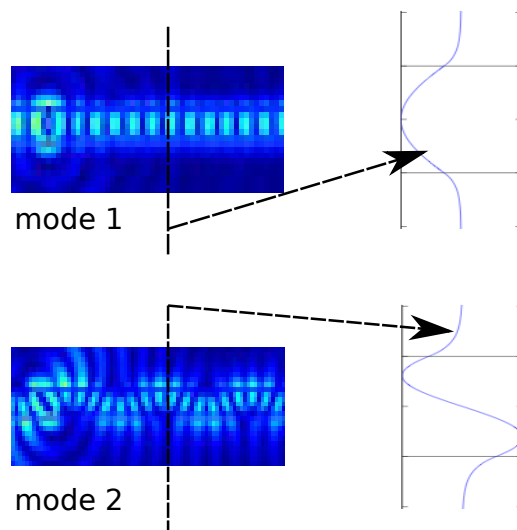


Figure 3.6: FDTD simulations of the incident angles and the supported modes

---

FDTD simulations of the incident angles and the first two supported modes have been presented in Fig. 3.6 that indicates that the Poynting vector of the first mode makes less angle with the waveguide axis than that of the second mode.

## 3.2 Introducing loss

Permittivity is a complex number for a lossy material, and this can be written as,

$$\epsilon = \epsilon' + j\epsilon'' \quad (3.26)$$

The loss tangent is defined as the ratio of imaginary to real part of the permittivity,

$$\tan \delta = \frac{\epsilon''}{\epsilon'} \quad (3.27)$$

The loss tangent can also be defined in terms of material conductivity as follows,

$$\tan \delta = \frac{\sigma}{\omega\epsilon'} \quad (3.28)$$

Here,  $\sigma$  is the conductivity of the material, and  $\omega$  is the angular frequency. The imaginary part of the permittivity is related to the conductivity of the material as follows,

$$\epsilon'' = \frac{\sigma}{\omega} \quad (3.29)$$

Refractive index of a lossy material must be complex as well since  $n = \sqrt{\epsilon}$ ,

$$n = n' + jn'' \quad (3.30)$$

Here, we are assuming that the dielectric and conduction loss both accounted into  $\epsilon''$ . The propagation constant is complex as well and is given by,

$$\gamma = \alpha + j\beta \quad (3.31)$$

$\alpha$  represents the loss of the mode in the waveguide guide.

Let us consider a case where the core is loss-less with a refractive index  $n_2$ ; the cladding (both the lower and upper) is lossy with refractive index  $n_1 = n'_1 + jn''_1$

and the structure is symmetric; hence, the upper and bottom cladding have the same material. Here  $n_1'$  and  $n_1''$  are the real and imaginary parts of the cladding refractive indices, respectively. Schematic diagram of such a structure is shown in Fig. 3.7.

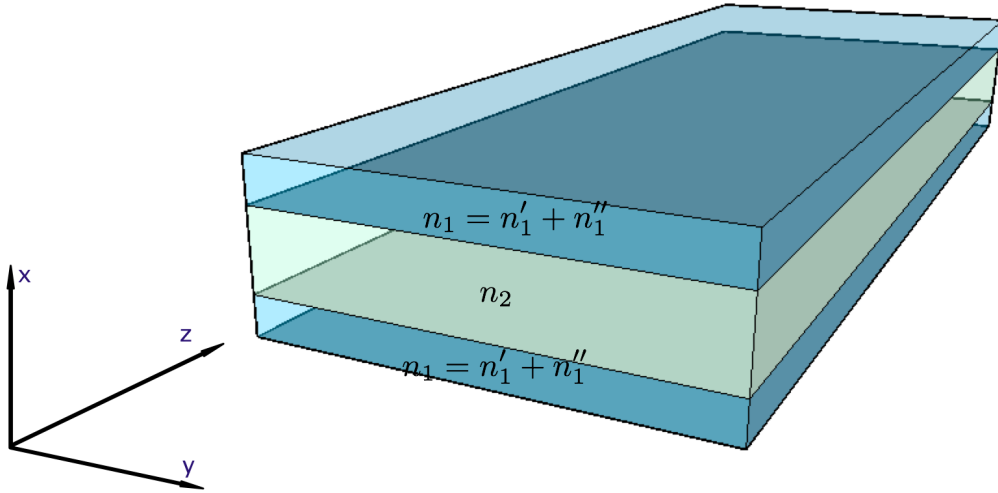


Figure 3.7: Planar Waveguide with lossy cladding

For TE polarisation and symmetric modes the field equations are as follows,

$$E_{y1} = Ae^{-q'x} \cos q''x \quad (3.32)$$

$$H_{z1} = \frac{Ae^{-q'x}}{j\omega\mu} [q' \cos q''x + q'' \sin q''x] \quad (3.33)$$

$$E_{y2} = Be^{-h'x} \cos h''x \quad (3.34)$$

$$H_{z2} = \frac{Be^{-h'x}}{j\omega\mu} [h'' \cos h'x + h' \sin h'x] \quad (3.35)$$

Boundary condition for tangential electric field,

$$E_{y1} = E_{y2}|_{x=d/2}$$

leads to,

$$Ae^{-\frac{q'd}{2}} \cos \frac{q''d}{2} = Be^{-\frac{h''d}{2}} \cos \frac{h'd}{2} \quad (3.36)$$

and for tangential magnetic field,

$$H_{z1} = H_{z2}|_{x=\frac{d}{2}}$$

leads to,

$$\frac{Ae^{-\frac{q'd}{2}}}{j\omega\mu} \left[ q' \cos \frac{q''d}{2} + q'' \sin \frac{q''d}{2} \right] \quad (3.37)$$

$$= \frac{Be^{-\frac{h''d}{2}}}{j\omega\mu} \left[ h'' \cos \frac{h'd}{2} + q'' \sin \frac{h'x}{2} \right] \quad (3.38)$$

After eliminating the constants A and B the detrimental equation takes the following form,

$$q' - h' \tan \frac{h'd}{2} = h'' - q'' \tan \frac{q''d}{2} \quad (3.39)$$

Assuming the complex propagation constant in the core  $\gamma = \alpha + j\beta$ ,  $h'$ ,  $h''$ ,  $q'$  and  $q''$  can be written as,

$$h' = \frac{M(M^2 + 4\alpha^2\beta^2)^{1/4}}{\sqrt{M^2 + \alpha^2\beta^2}} \quad (3.40)$$

$$h'' = \frac{\alpha\beta(M^2 + 4\alpha^2\beta^2)^{1/4}}{\sqrt{M^2 + \alpha^2\beta^2}} \quad (3.41)$$

$$q' = \frac{N(N^2 + 4(\alpha\beta + k'_1 k''_1)^2)^{1/4}}{\sqrt{(N^2 + (\alpha\beta + k'_1 k''_1)^2)}} \quad (3.42)$$

$$q'' = \frac{(\alpha\beta + k'_1 k''_1)(N^2 + 4(\alpha\beta + k'_1 k''_1)^2)^{1/4}}{\sqrt{(N^2 + (\alpha\beta + k'_1 k''_1)^2)}} \quad (3.43)$$

where

$$M = k_2^2 - \beta^2 + \alpha^2 = h'^2 - h''^2$$

and

$$N = \beta^2 - \alpha^2 - k_1'^2 + k_1''^2 = q'^2 - q''^2$$

Normalised frequency of this structure is defined as

$$v = \text{Re} \left( \frac{\pi d}{\lambda} \sqrt{n_2^2 - n_1'^2 + n_1''^2 - j2n_1'n_1''} \right) \quad (3.44)$$

after simplification it takes the following form,

$$v = \frac{\pi d}{\lambda} \left( (n_2^2 - n_1'^2 + n_1''^2)^2 + 4n_1'^2 n_1''^2 \right)^{1/4} \frac{n_2^2 - n_1'^2 + n_1''^2}{\sqrt{(n_2^2 - n_1'^2 + n_1''^2)^2 + n_1'^2 n_1''^2}} \quad (3.45)$$

for lossless cladding, where  $n_1'' = 0$ , the equation takes the well known form,

$$V = \frac{\pi d}{\lambda} \sqrt{n_2^2 - n_1'^2} \quad (3.46)$$

The parameter  $\mathbf{M}$  is plotted against  $\tan \delta$  for a 2  $\mu\text{m}$  guide at the wavelength  $\lambda = 550 \text{ nm}$  in Fig. 3.8.

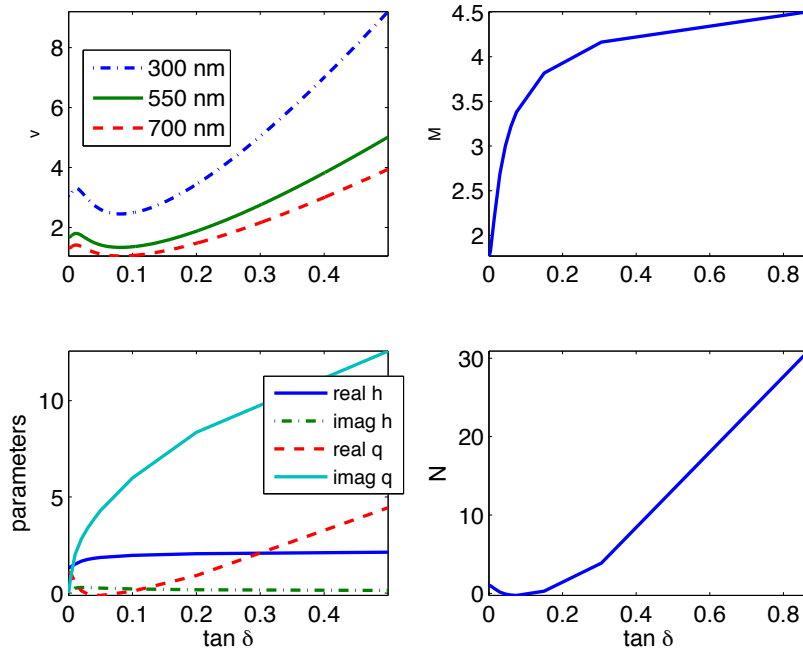


Figure 3.8: Lossy Guide Parameters

The core refractive index and the real part of the cladding refractive index is kept constant. The parameter  $\mathbf{M}$  is appears to be an increasing function of  $\tan \delta$ . Figure 3.8 shows the parameter  $\mathbf{N}$  under same conditions, and it appears to be decreasing with  $\tan \delta$  for very low loss tangent, reaches a minimum point at around  $\tan \delta \approx 1.0$ , increases beyond that loss tangent. Figure 3.8 shows how the normalised frequency  $V$  varies with the imaginary part of the cladding refractive index. It is evident from the figure that the  $V$  decreases at very low loss values with increasing material loss, reaches a minimum at some point (corresponds to  $\tan \delta \approx 0.12$ ), and then increase with increasing the material loss. Increased  $V$  means the cutoff wavelength  $\lambda_c$  to be increased. Figure 3.8 shows the variations of the parameters  $M$ ,  $N$ ,  $v$ ,  $h'$ ,  $h''$ ,  $q'$  and  $q''$  with  $\tan \delta$  for fixed  $d = 2 \mu\text{m}$ . Abscissa for all the plots of figure 3.8 are  $\tan \delta$ .

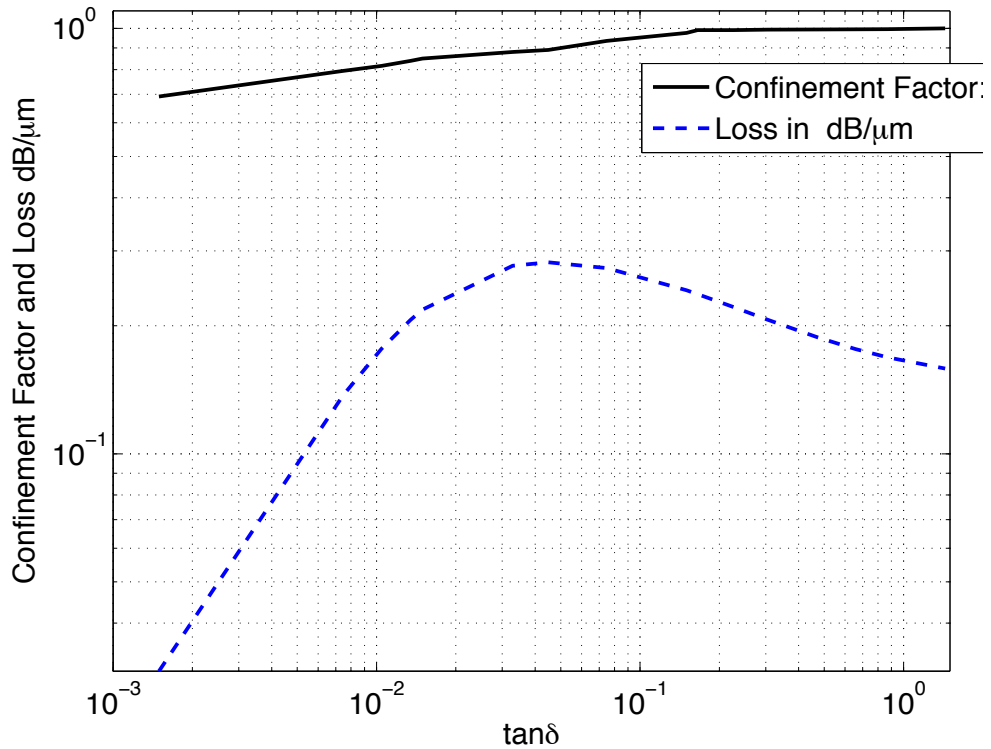


Figure 3.9: Confinement factor and Loss vs  $\tan \delta$

With the increasing material loss, the field confinement increases but the

waveguide loss has maxima at a certain material loss value, beyond that point the guide loss decreases as can be seen in Fig. 3.9. When the cladding is lossy the field in the core is exponentially decreasing sinusoid instead of sinusoid as in the lossless case.

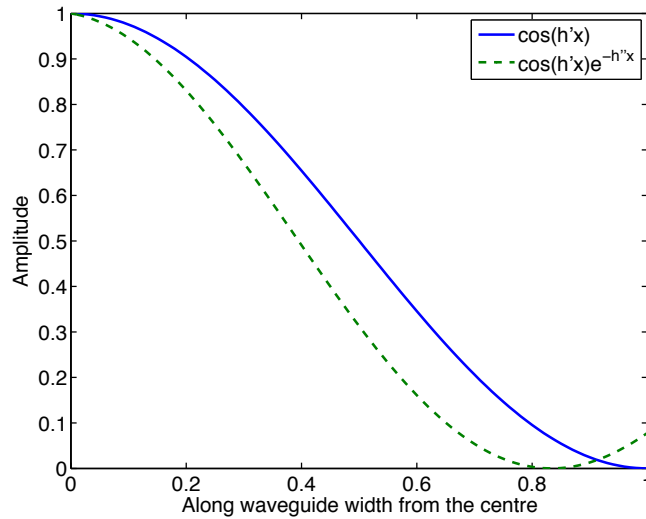


Figure 3.10: Field along guide dimension for lossy cladding

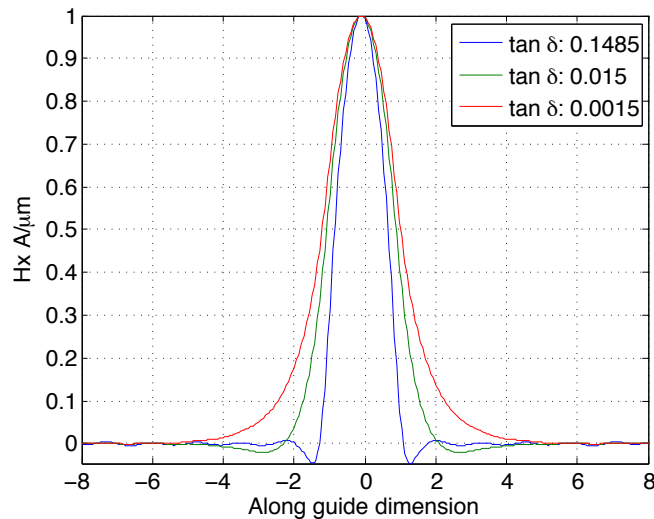


Figure 3.11: Field profile for lossy cladding

Here, Fig. 3.10 shows that multiplying the sinusoid by an exponentially decreasing function results in narrowing down the first lobe toward the centre. That

---

might be the reason we observe an increase in confinement factor with a rise in  $\tan \delta$  of the cladding material as shown in Fig. 3.9. The field profile in Fig. 3.11 shows that the field is exponentially varying sinusoid.

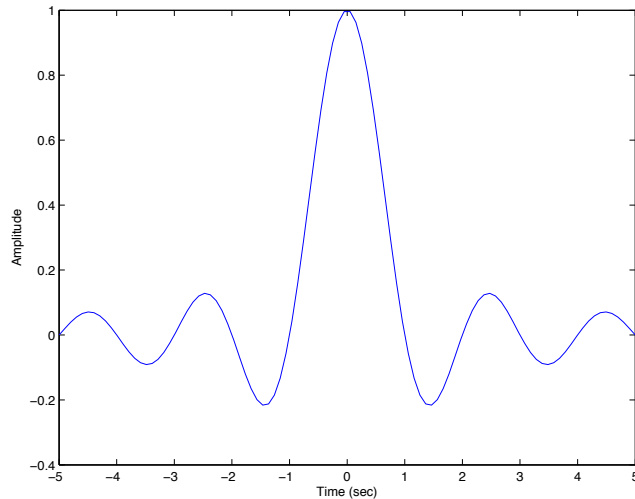


Figure 3.12: Sinc function plot

Intensity profile has a striking similarity to the plot of the absolute value of  $\text{sinc}(x)$  in shown in Fig. 3.12. The interesting point to note here that the field pattern in an Airy disc generated by a finite aperture is very similar to these theoretical field patterns of a lossy guide. The connection between them, if there in any, shall be considered in details in the later parts of the results section.

### 3.3 Importance of Evanescent Fields

For a guided wave although the power flows through the core region, from the solution of the Maxwell's equation we can see that the field components are not zero at the cladding region. Usually for a waveguide with loss-less materials, it is found that the field in the cladding region decreases exponentially to zero, this field in the cladding region in known as the evanescent field. The guided mode propagates through the core region at a phase velocity defined by the  $n_{eff}$  of that mode, and for a guide mode  $n_{eff} > n_{cladding}$ , but the evanescent field in the

cladding region travels at the same velocity as of the core region field. Although the evanescent field does not carry power, it must be present in order the mode to effectively guided. If we remove the evanescent field by any means, the fields present in the core region will eventually loose some of its power and will produce the evanescent field to propagate properly.

A Finite Difference Time Dimain (FDTD) method is implemented in MATLAB to produce the simulation results presented in this section and onward. It is assumed that  $\Delta x = \Delta y = \Delta z = \Delta = 50$  nm and  $\Delta t = 9.62 \times 10^{-17}$  sec. is used by using equation 2.101.

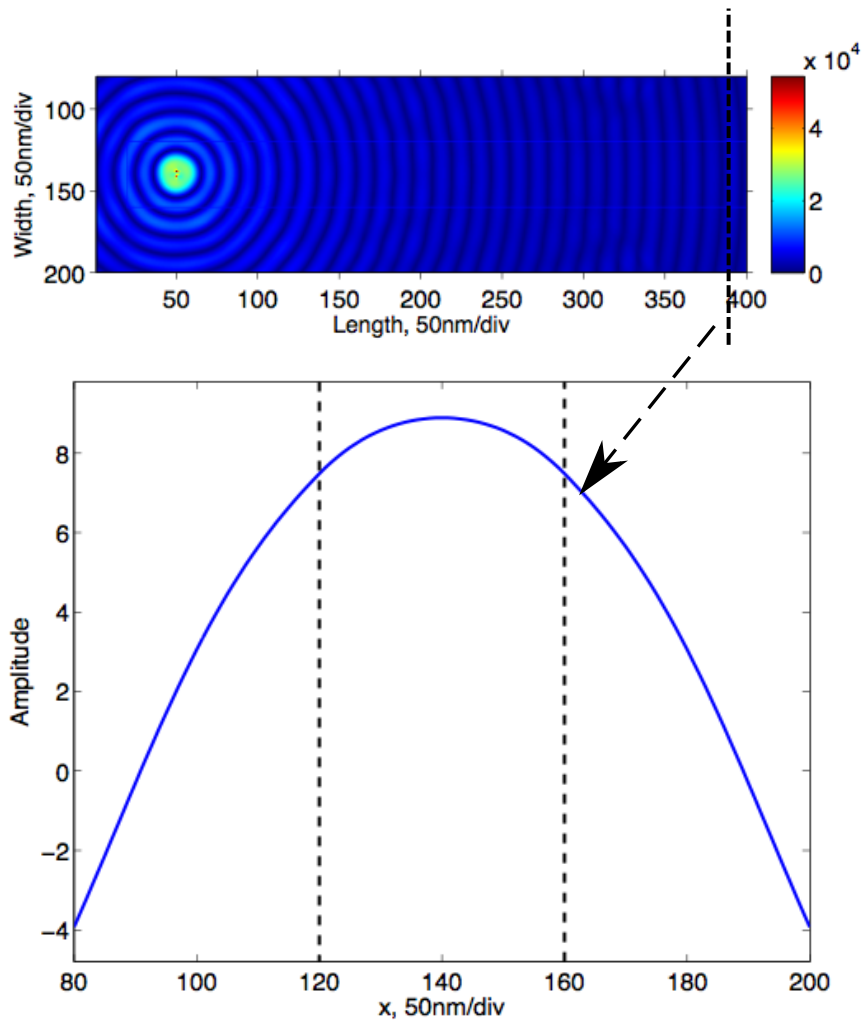


Figure 3.13: Point source in single mode guide

When a point source is present in the core of a waveguide, it starts to radiate in all directions. At the core-cladding interface, the wavefronts that make an angle more than the critical angle radiates to the cladding. The waveform that is equal to the angle to that of a supported mode would be guided through the core region. Figure 3.13 shows a point source placed inside the core of a single-moded waveguide excites only the fundamental mode and is guided by the core.

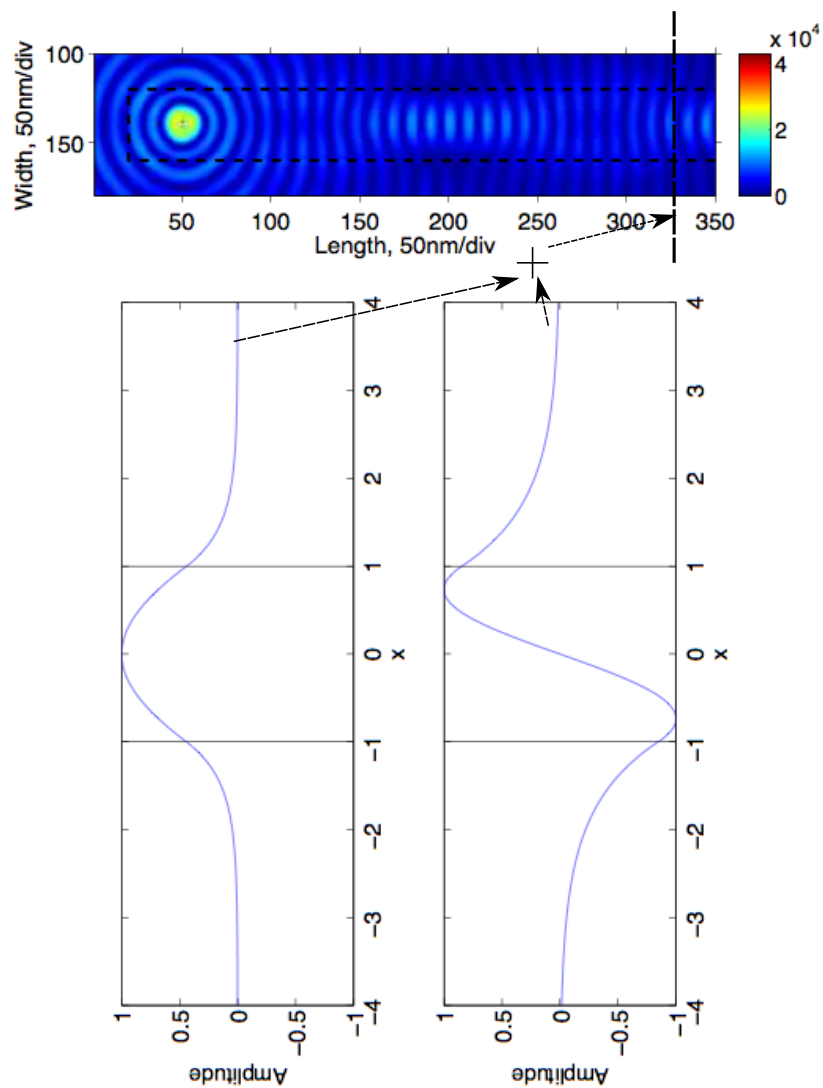


Figure 3.14: Point source in a multi-mode guide

Figure 3.14 shows that a point source excites the first two modes in the core

region where the waveguide is multi moded and supports upto the second mode. As the materials used in these two cases were loss-less, the evanescent fields are exponentially decreasing as expected.

Figure 3.15 shows that when a plane wave source is placed in the core region of the multimoded waveguide where the wavefront of the source makes very small angle with the guide axis excites only the first mode that is guided by the core.

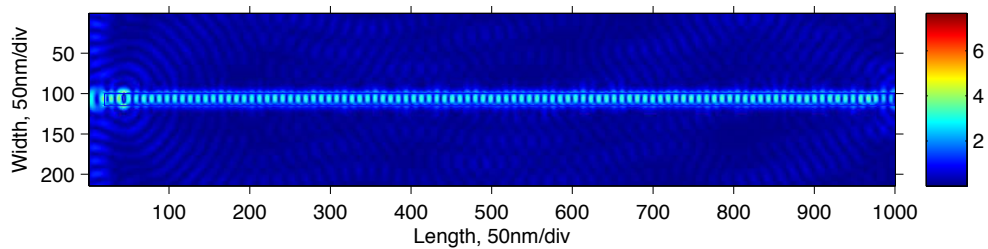


Figure 3.15: Plane wave in a multimode guide

Figure 3.16 shows when the plane wave source's wavefront is adjusted to make a higher angle with the guide axis in a multimoded waveguide, it is possible to excite only the second mode. By adjusting the angle it is however possible to excite other higher modes as well.

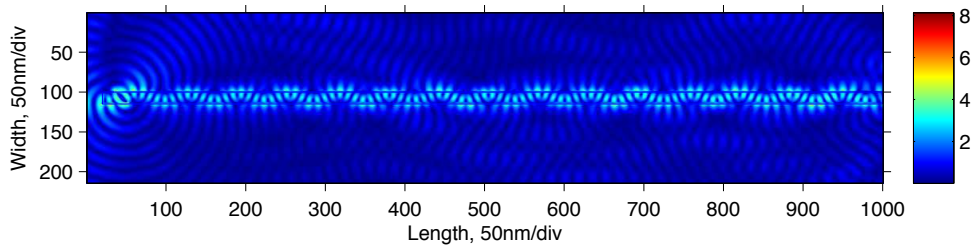


Figure 3.16: Plane wave incident at an angle to excite the higher order modes

In a multimode waveguide, if a source is placed whose field profile resembles that of a supported mode of the waveguide, the mode would travel unperturbed through it. Figure 3.17 shows when the mode profile of the first mode is placed as the source in a waveguide with a lossless material, it is guided by the waveguide unperturbed.

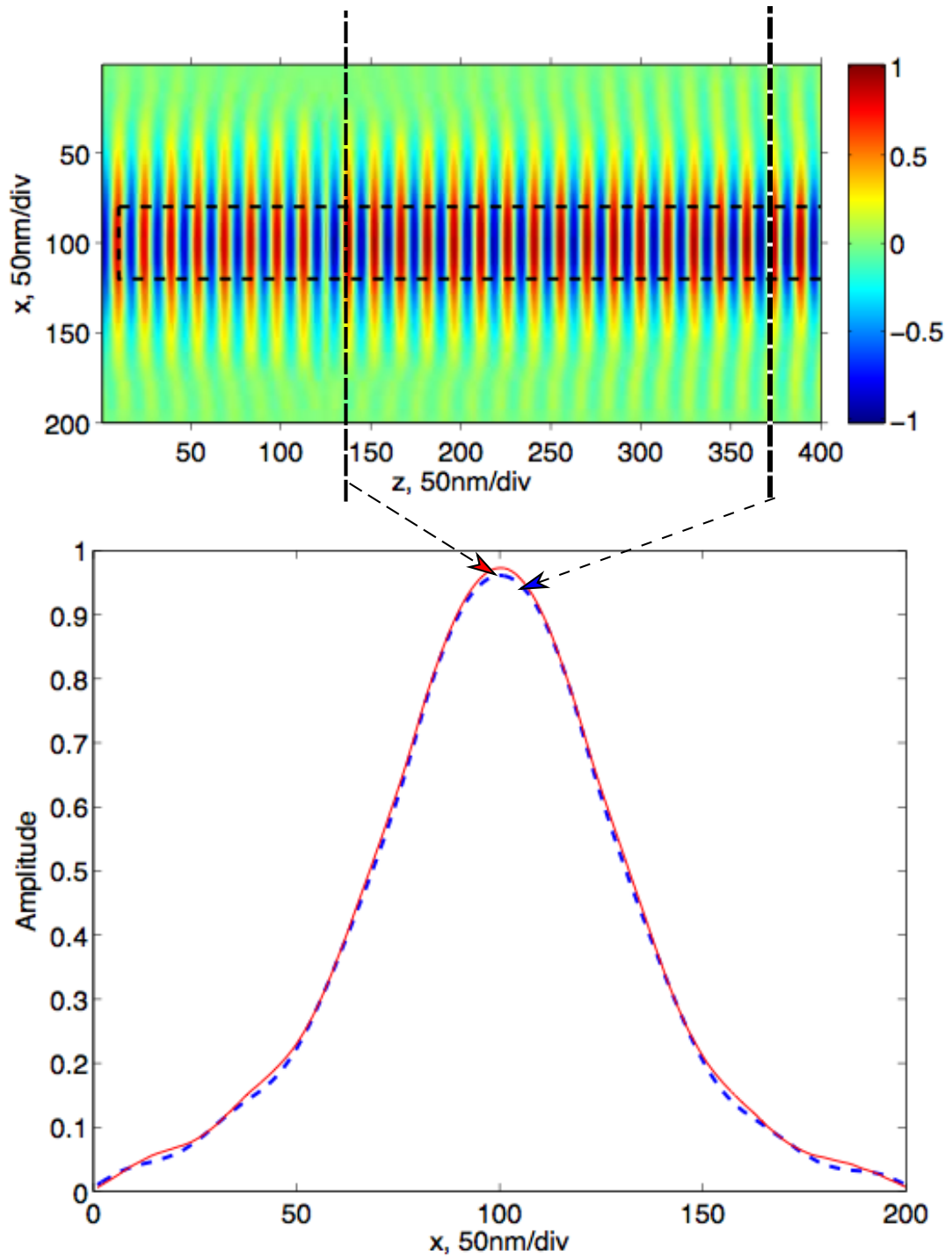


Figure 3.17: Mode input - mode output; multimode

In the previous sections, it has been shown that for a waveguide with lossy cladding has supported modes where for the fundamental mode the core region is exponentially decreasing sinusoid, and field profile at the cladding region is sinusoidally varying decreasing sinusoid. The exponential term in the core and the sinusoidal term in the cladding region depends on the loss value present in the cladding material.

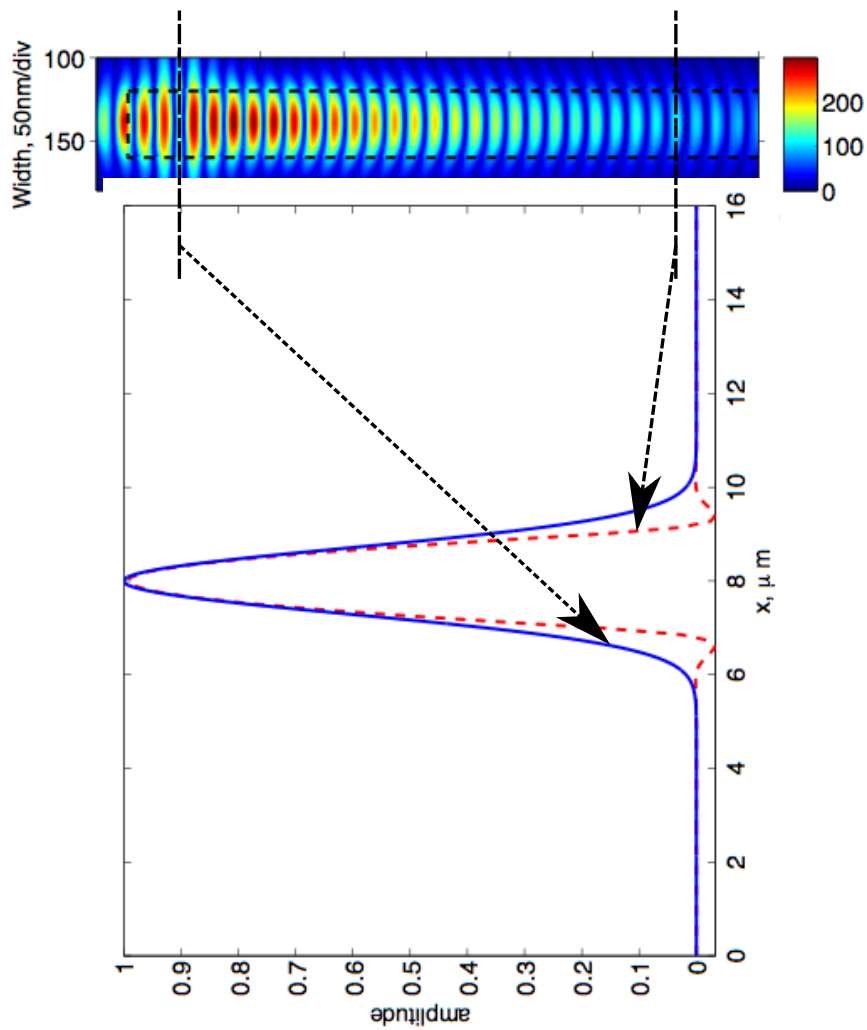


Figure 3.18: Gaussian input - mode output; multimode guide

For a waveguide with a lossless material the mode shape of the fundamental or the lowest order mode can be approximated by a Gaussian function. Figure

3.18 shows when a Gaussian profile is placed at the input of a waveguide with lossy cladding, the mode shape evolves to that of an exponentially decreasing sinusoidal profile. It can be concluded from the figure that the field confinement is increased due to the loss present in the cladding material.

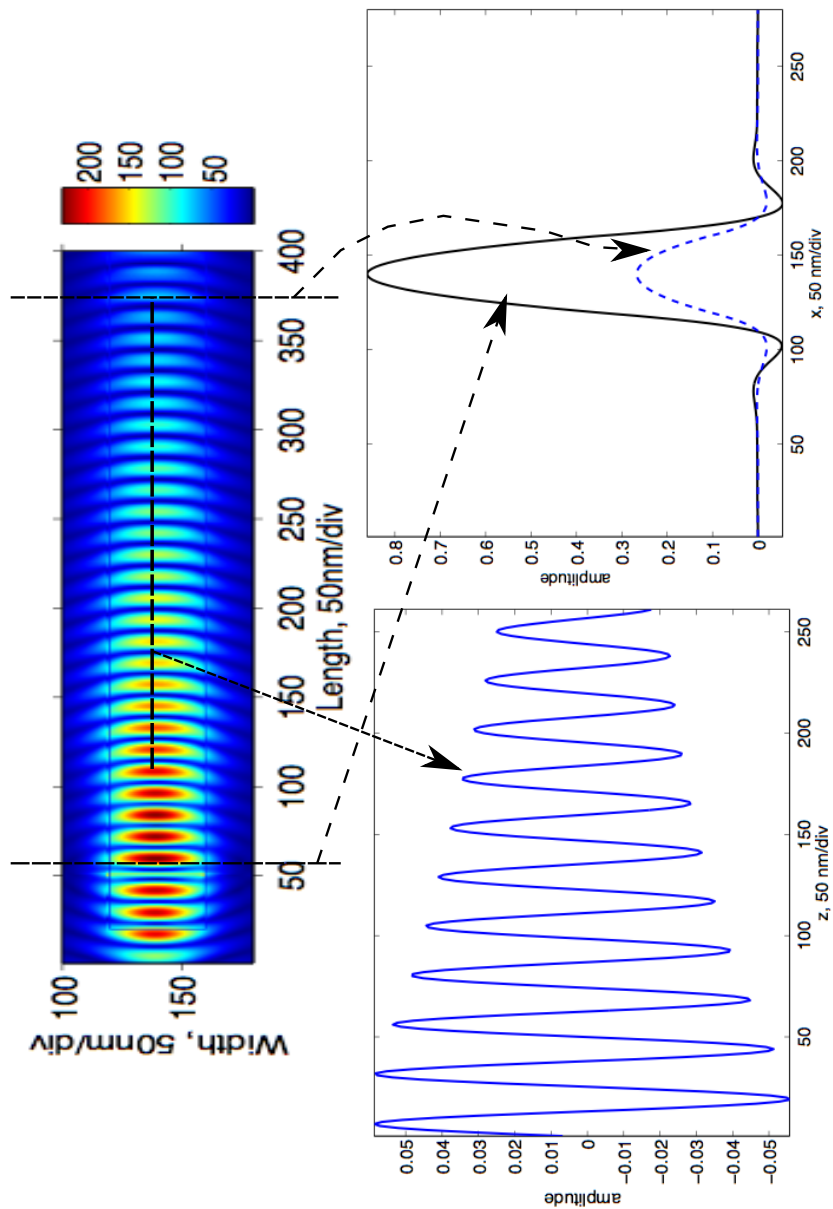


Figure 3.19: Lossy Mode input - mode output

---

Figure 3.19 shows that when the mode profile of a lossy mode is used as the source of the waveguide, the mode shape remains unchanged. Due to the material loss, the  $n_{eff}$  should be a complex number, and the mode should be lossy. It is evident from the figure that the mode experiences power loss as it propagates through the waveguide but the field profile as well as the confinement remains unchanged.

### 3.4 Waveguide Loss Calculation

For the lossy case the effective index is a complex value, which is given by,

$$n_{eff} = n_r + jn_i \quad (3.47)$$

here  $n_r$  and  $n_i$  are the real and imaginary parts of the effective index  $n_{eff}$  respectively. The real part of the propagation constant is related to the imaginary part of the effective index as,

$$\alpha = \frac{2\pi}{\lambda} n_i \quad (3.48)$$

The waveguide loss in dB can be written by,

$$Loss = -8.6859\alpha z \quad (3.49)$$

$$Loss(dB/\mu m) = -8.6859\alpha \quad (3.50)$$

it is considered here that the  $\lambda$  is expressed in  $\mu m$ .

---

### 3.5 Planar guide as a limiting case of rectangular guide

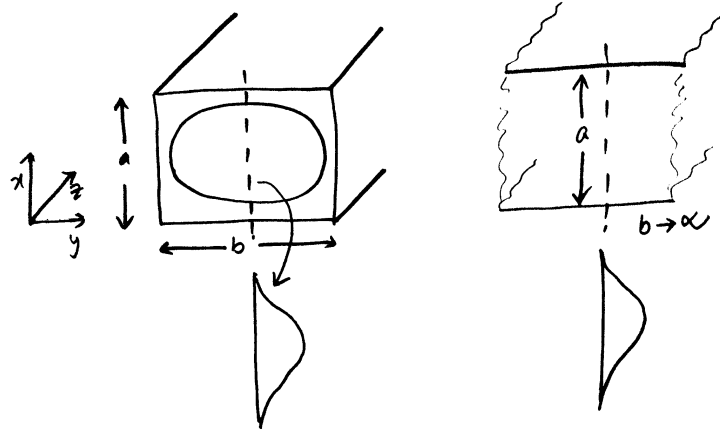


Figure 3.20: Rectangular guide - mode along dimension; planar guide field along dimension

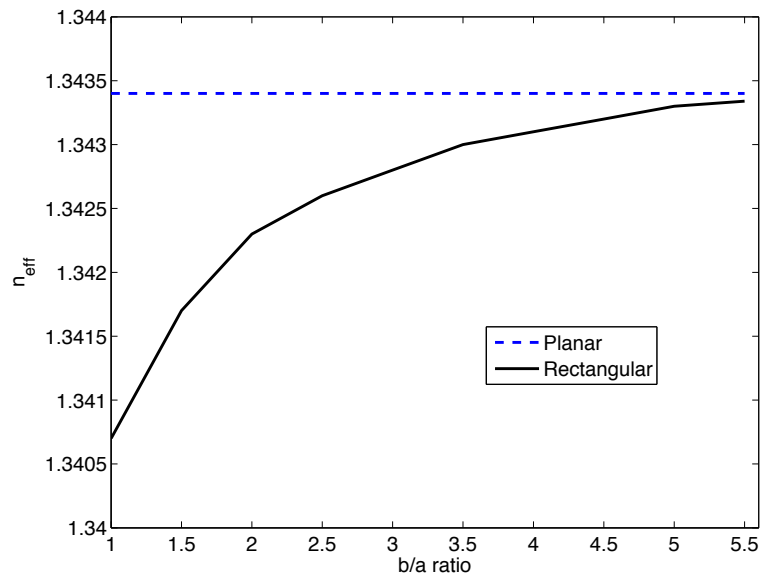


Figure 3.21:  $n_{eff}$  changes with  $b/a$  ratio;  $NA=0.15$ ,  $\lambda = 550$  nm

---

Here,  $n_{eff1}$  and  $n_{eff2}$  are the effective indices of the planar and rectangular guide having the same height. The width of the rectangular guide is varied to observe the impact. It is evident from the Fig. 3.21, as the width of the rectangular guide approaches infinity,  $n_{eff2}$  approaches  $n_{eff1}$ , where the blue dotted line represents  $n_{eff1}$  and the black solid line is for  $n_{eff2}$ .

### 3.6 Selection of Wavelength Range

The wavelengths range of 390 nm - 740 nm is considered as the visible spectrum as shown in Fig. 3.23. Although the sun radiates, as shown in the sun spectra in Fig. 3.22, wavelength as small as 100 nm to far infrared (3000 nm), but the wavelengths below 300 nm are absorbed in the Earth's atmosphere, so at Earth's surface, the sunlight contains only wavelengths above 300 nm. The simulation carried out in this study uses  $\lambda = 50$  nm as the lowest wavelength. This allows our propagation characteristics still valid for six times the dimensions employed in the study. Although the focuses the dimension around  $2 \mu m$  (typical dimension of insect rhabdom), we can analyse the guides with dimension  $12 \mu m$  (Glial cell dimension at some cross-sections) using the same set of results.

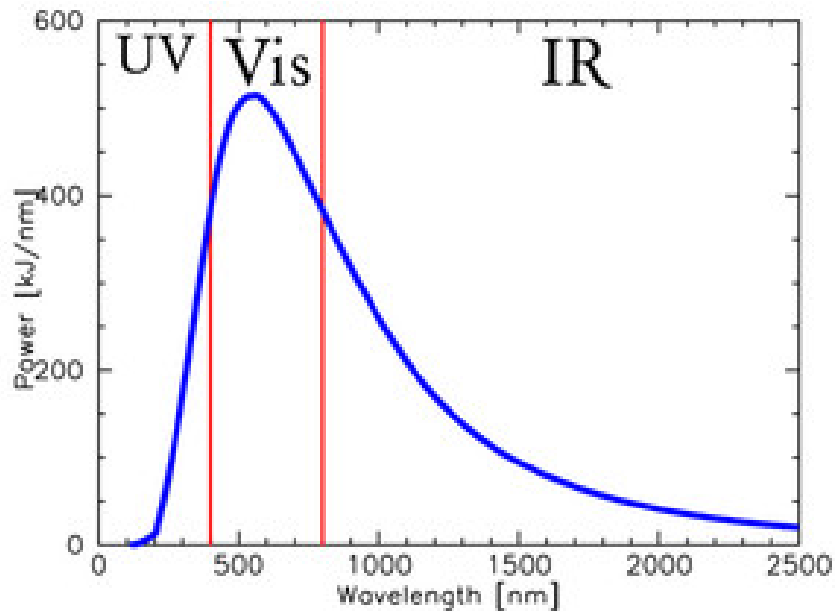


Figure 3.22: Sun spectra on the Earth surface source:

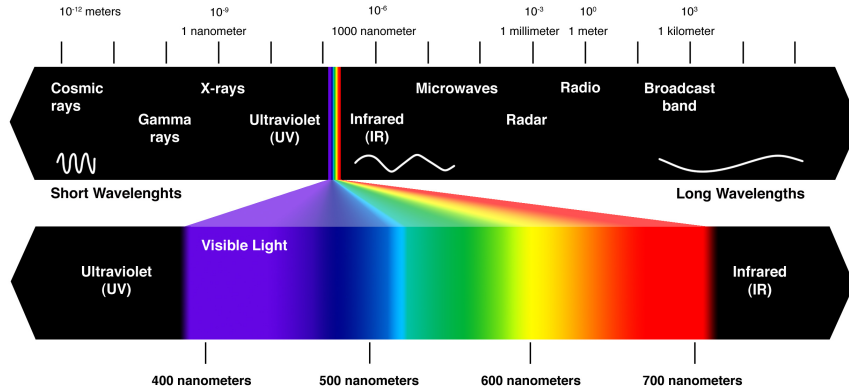


Figure 3.23: Visible spectrum source:

The normalised frequency  $V = \frac{\pi d}{\lambda} \sqrt{n_1^2 - n_2^2}$  used in propagation characteristics is a function of  $d/\lambda$  ratio, that means a guide with twice the dimension has the same effective index ( $n_{eff}$ ) if the  $\lambda$  is doubled as long as the refractive index profile remains the same. As  $n_{eff}$  determines the phase velocity as well as the angle the poynting vector makes with the guide axis, the results obtained from the simulation for  $2 \mu m$  guide can be extended for higher as well as lower dimension guides.

### 3.7 Selection of Methods

The FEM and FDFD methods can be used to solve the eigenvalue problem formulated by discretising the simulation domain for Maxwell's equations. As previously discussed, the FD based methods do not work well for approximating irregular geometries due to their staircase representation for slanted or curved edges that are frequently encountered in biological structures. Figure 3.24 shows how the FD based meshing approximates the curved boundaries by stair casing, while the meshing used for FE based methods can follow the curves with reasonable accuracies. Despite being computationally more expensive than FD based methods, FE based methods can produce results with much better accuracies because of the advantage it gets from meshing.

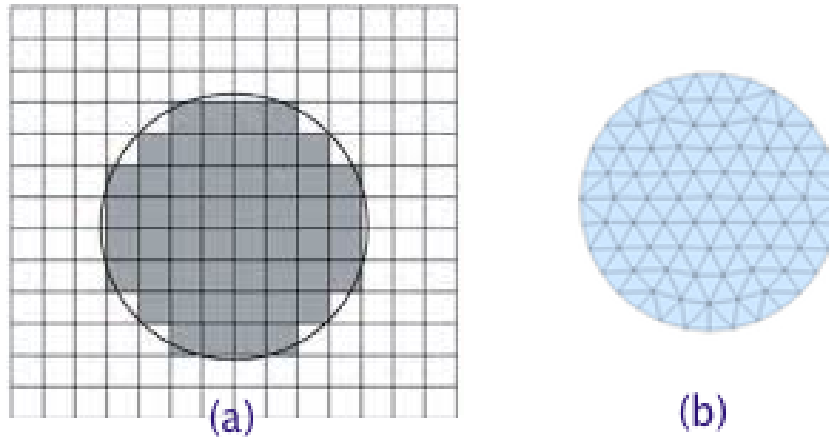


Figure 3.24: Approximating irregular geometries with FE and FD based methods

FE based discretization performs well for domains containing irregular shapes or boundaries. Figure 3.25 shows some examples of computational domains where the FE based meshing can approximate the domain very well, FD based meshing would not produce excellent approximation in these cases due to their stair-casing problem. In FE based meshing it is also possible to refine the mesh sizes at locations where higher accuracies are required. Therefore, an FE-based method is the ideal choice for simulating biological structures, despite being computationally more expensive.

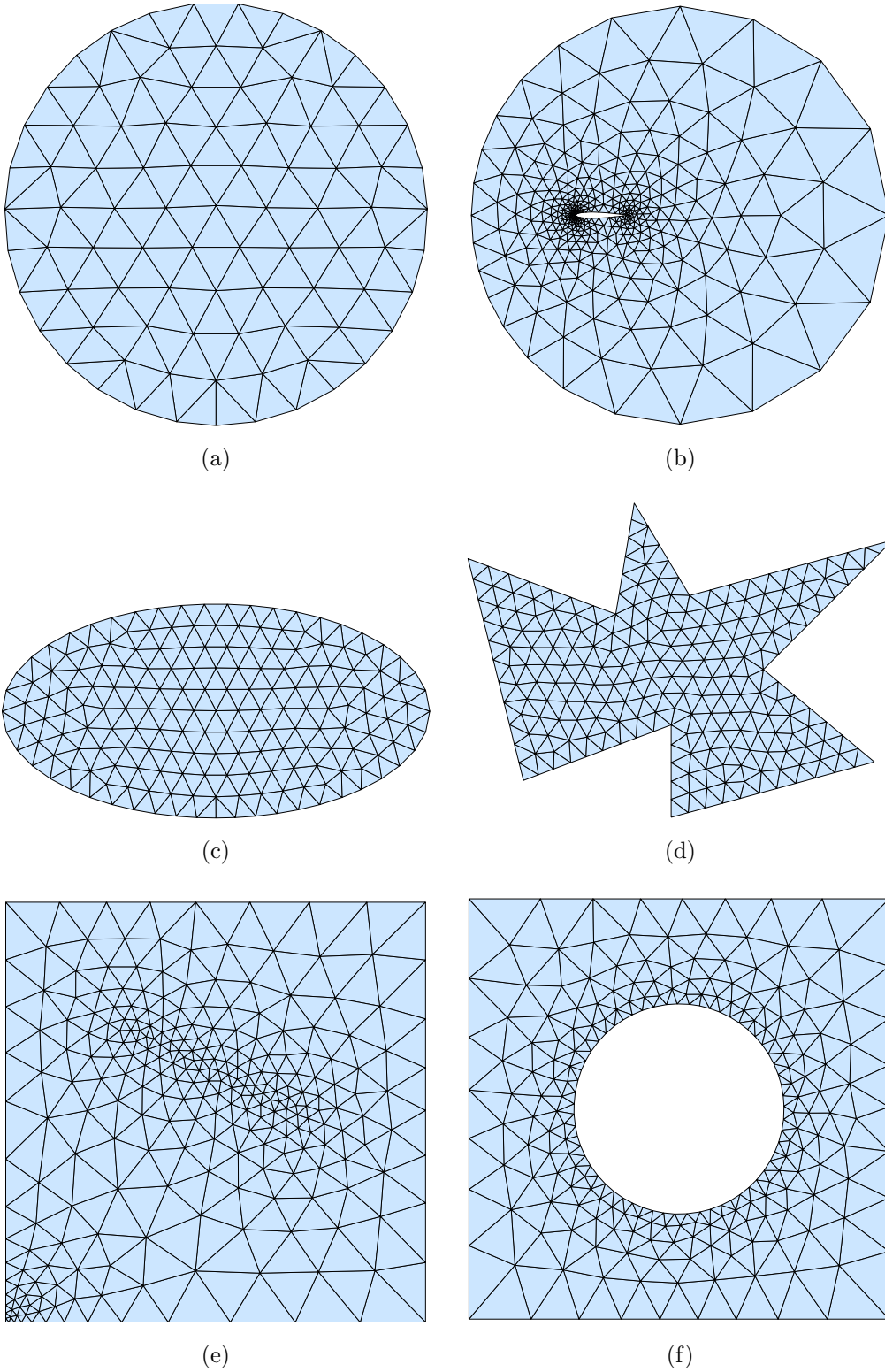


Figure 3.25: Examples of approximating some complicated geometries in FE based mesh (Burkardt [2011])

---

### 3.8 Rectangular guide

The theoretical analysis of a rectangular dielectric waveguide, even with a simple refracting index profiles is very complicated. Goell [1969] and Marcatili [1969] did some groundbreaking analysis on this type of optical waveguide. For more complicated shape and refracting index profiles numerical solution of Maxwell's equations can provide us with the solutions with reasonable accuracies, and in most of the cases the only way to address the problem.

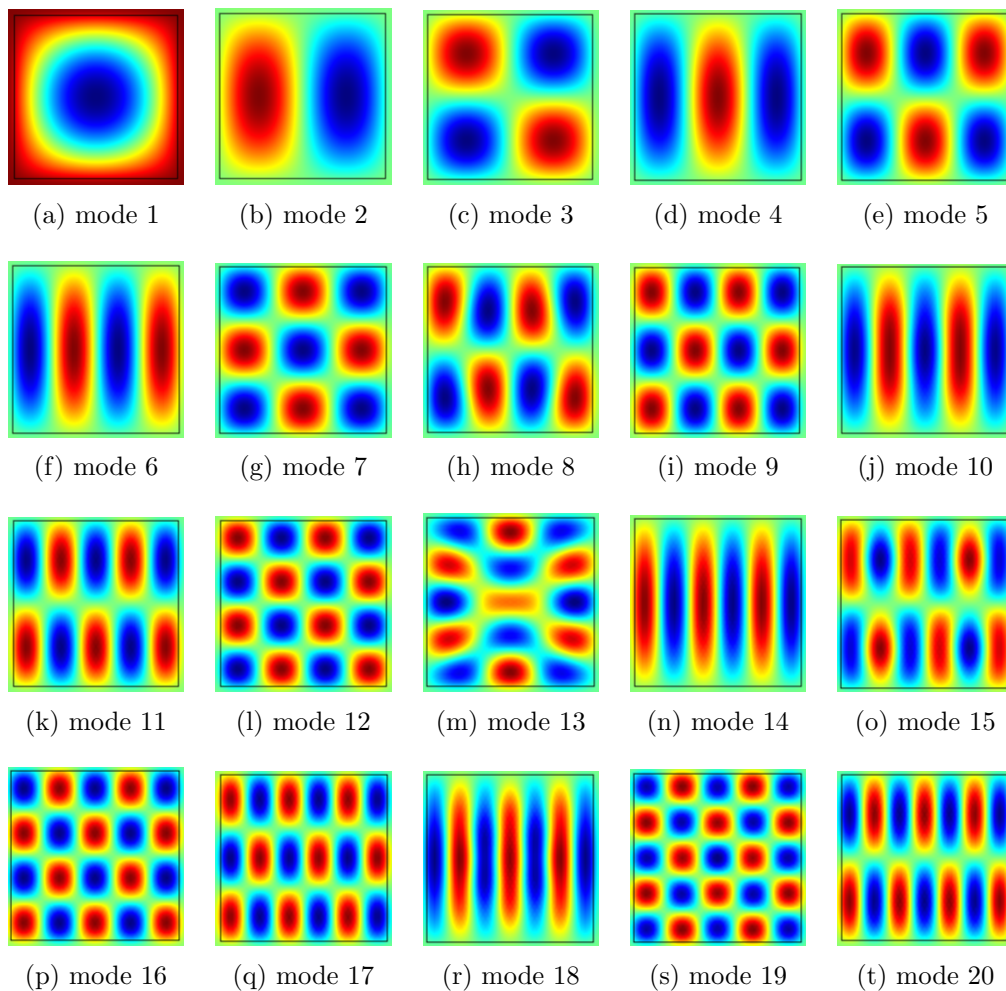


Figure 3.26: First 20 modes of a rectangular waveguide, dimension  $2\mu m \times 2\mu m$ , NA=0.15

---

Numerical solution of Maxwell's equations is carried out to obtain the mode profiles for a rectangular waveguide using  $\mathbf{H}$  field based full vectorial Finite Element Method (Rahman and Agrawal [2013]). 20000 elements have been used to discretize the computational domain. The core and the cladding refractive indices are taken as 1.347 and 1.339 respectively, with no material loss in the core and the cladding region. To obtain higher modes, the operating wavelength,  $\lambda = 50$  nm is considered. Width and height of the core are taken as equal; the width =  $2\mu$  m is taken. Figure 3.26 shows the  $H_y$  field distribution of the first 20 supported modes of such a waveguide. In all of the modes, the  $H_y$  is the dominant field component. For a guided mode the condition  $n_{core} \geq n_{eff} \geq n_{cladding}$  must be satisfied, here the lowest order mode has the highest  $n_{eff}$ , the modes have subsequently lower  $n_{eff}$ .

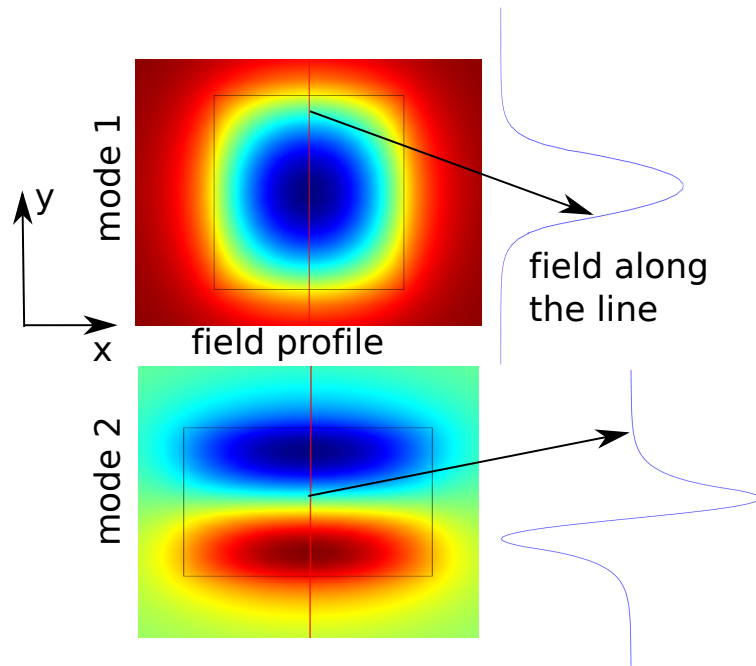


Figure 3.27: The first and the second modes of the rectangular waveguide with fields along the axis

For a rectangular waveguide, the field patterns have symmetries along two directions, x and y. The mode 1 has no zero crossing in the field in x- and y-directions, this mode is commonly known as the  $H_y^{11}$  mode, where the subscript

$y$  represents the dominant field component and the superscript 11 represents one variation in the x-direction and one variation in the y-direction. The mode 2 is the  $H_y^{21}$  mode, has two variations in the x-direction and one variation in y direction. Figure 3.27 shows the field variations of the first two modes along the y-axis at the centre of the guide core. The other modes as shown in Fig. 3.26 have higher variations in the x and/or y directions.

### 3.9 Circular guide

Optical fibres are the most well-known examples of an optical waveguide with a circular cross-section. Fortunately, the analytic solution of this type of waveguide is available in the literature Yeh and Shimabukuro [2008]. The typical structure of a waveguide with circular cross-section is shown in Fig. 3.28. For this waveguide  $n_{core} = 1.347$  and  $n_{cladding} = 1.339$  is assumed and the mode profiles have been generated using FEM mode solver with similar parameters that of the rectangular waveguide. The diameter of the core is taken as  $2\mu$  m.

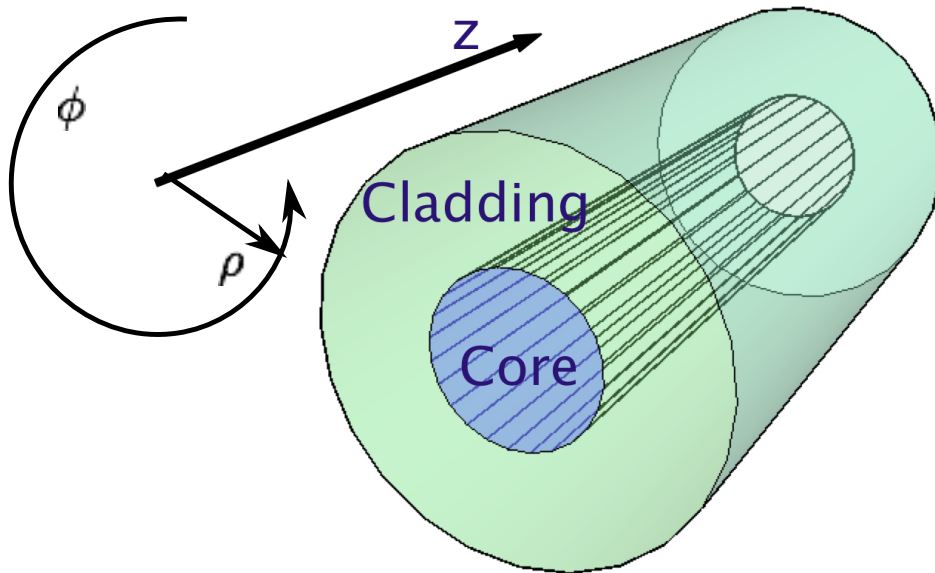


Figure 3.28: Circular Optical Waveguide structure

For waveguides with a circular cross-section, the mode profiles have two axes of symmetries, radial direction ( $\rho$ ) and angular direction ( $\phi$ ). Figure 3.29 shows

---

the first 20 supported modes of the circular optical waveguide. Mode 1 of this circular waveguide has one variation along  $\rho$  but no variations along  $\phi$ ; mode 2 has on variation in  $\rho$  and one variation in  $\phi$ ; the other higher order modes have higher variations in the field along  $\rho$  and/or  $\phi$ .

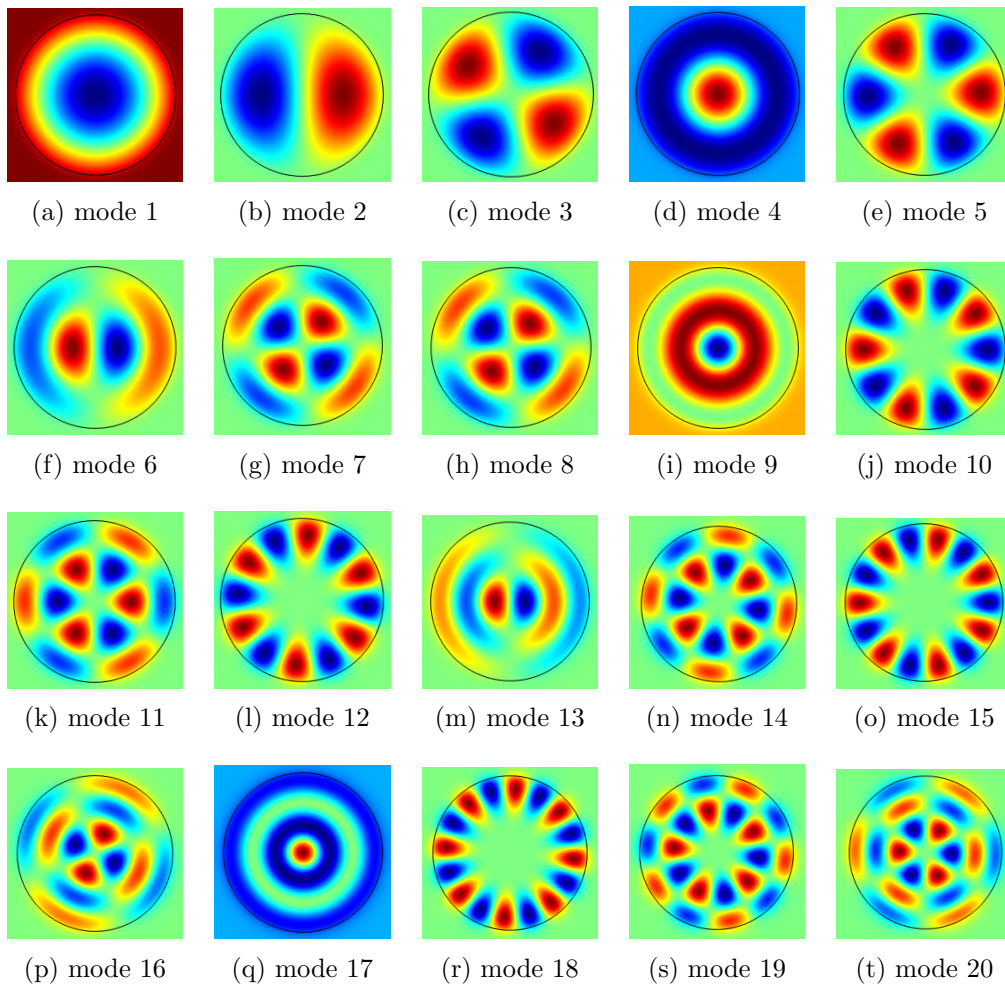


Figure 3.29: First 20 modes of a Circular waveguide, core diameter  $2\mu m$ , NA=0.15

Figure 3.30 shows the comparison of field profiles between the mode 1 and the mode 4. Both of the modes have no variations along  $\phi$ ; mode 1 has one variation along  $\rho$  and mode 4 has two variations along  $\rho$ .

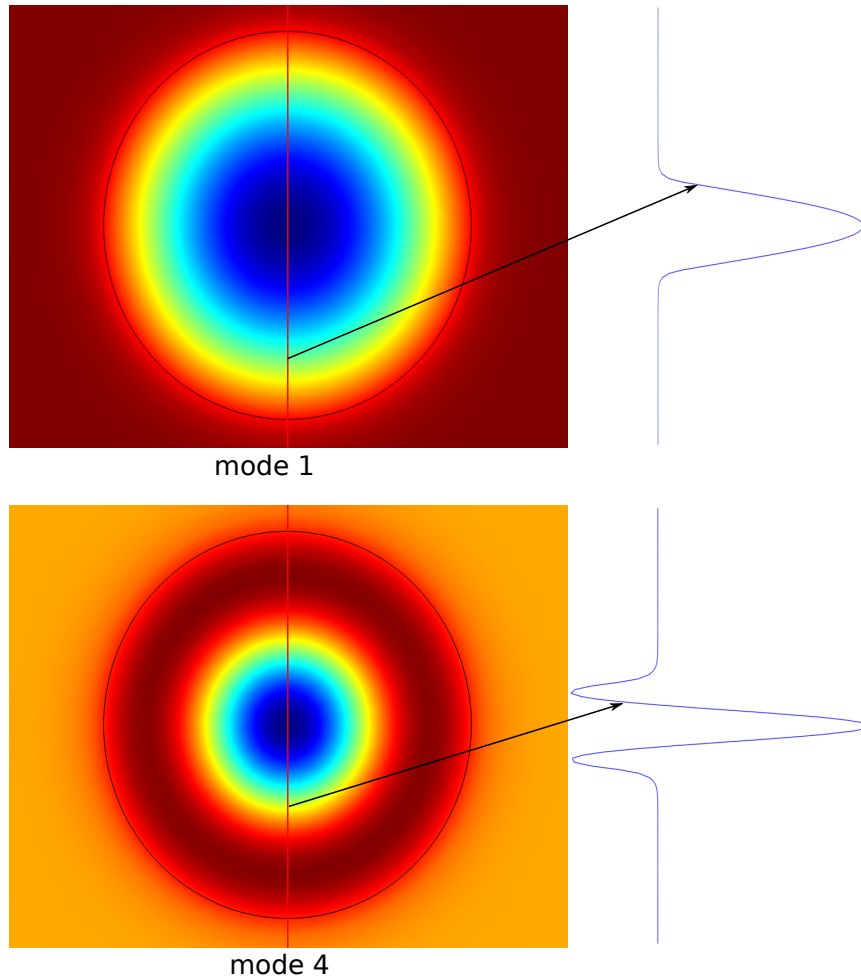


Figure 3.30: Comparisons of the field profile of mode 1 and mode 4 of a circular optical waveguide

The first 2 modes of both rectangular and circular waveguides have similar field profiles.

### 3.10 Hexagonal guide

The analytic solution of Hexagonal waveguide structure requires rigorous mathematics and in most of the cases with various refractive index profiles, it is impossible to find the analytic solution. In analysing biological structures, the hexagonal structure is essential as the hexagonal structure is frequently found in nature. To

---

obtain the mode profile of a hexagonal structure, we have to rely on the numerical methods.

A typical structure of a hexagonal waveguide is shown in Fig. 3.31, where  $n_{core} = 1.347$  and  $n_{cladding} = 1.339$  is assumed and the mode profiles have been generated using FEM mode solver with the similar parameters as considered for the circular and rectangular waveguide. Side to side distance is taken as  $2\mu\text{ m}$ .

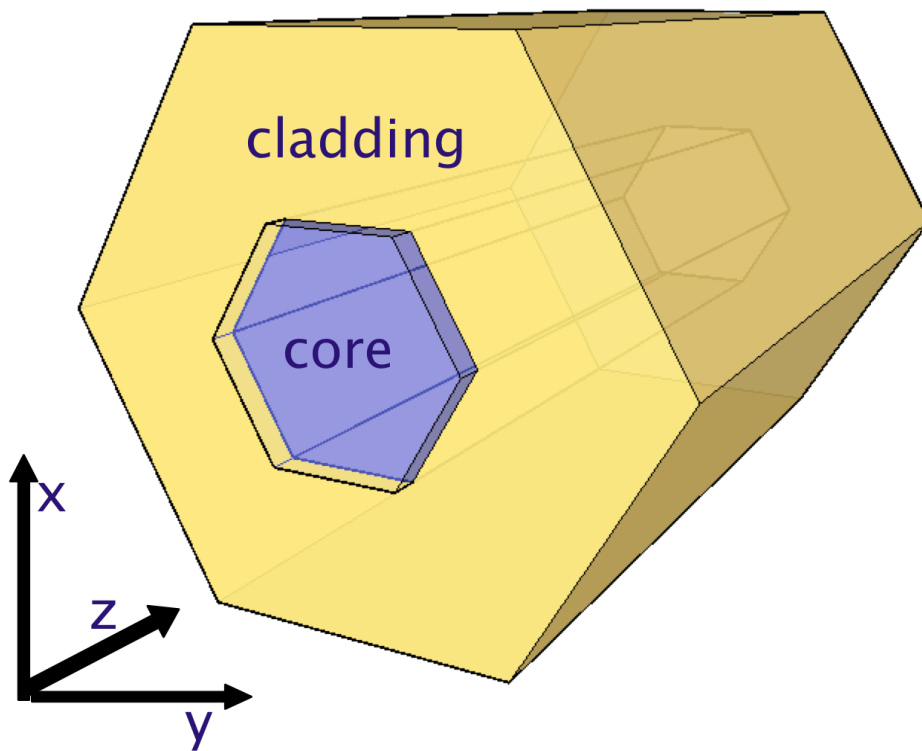


Figure 3.31: Hexagonal Optical Waveguide Structures

Figure 3.32 shows the first 20 modes of a Hexagonal waveguide. The numbering of modes is used as proposed by [Bauer and Reiss \[1978\]](#). The first mode has similar field profile as that of the circular and rectangular waveguide.

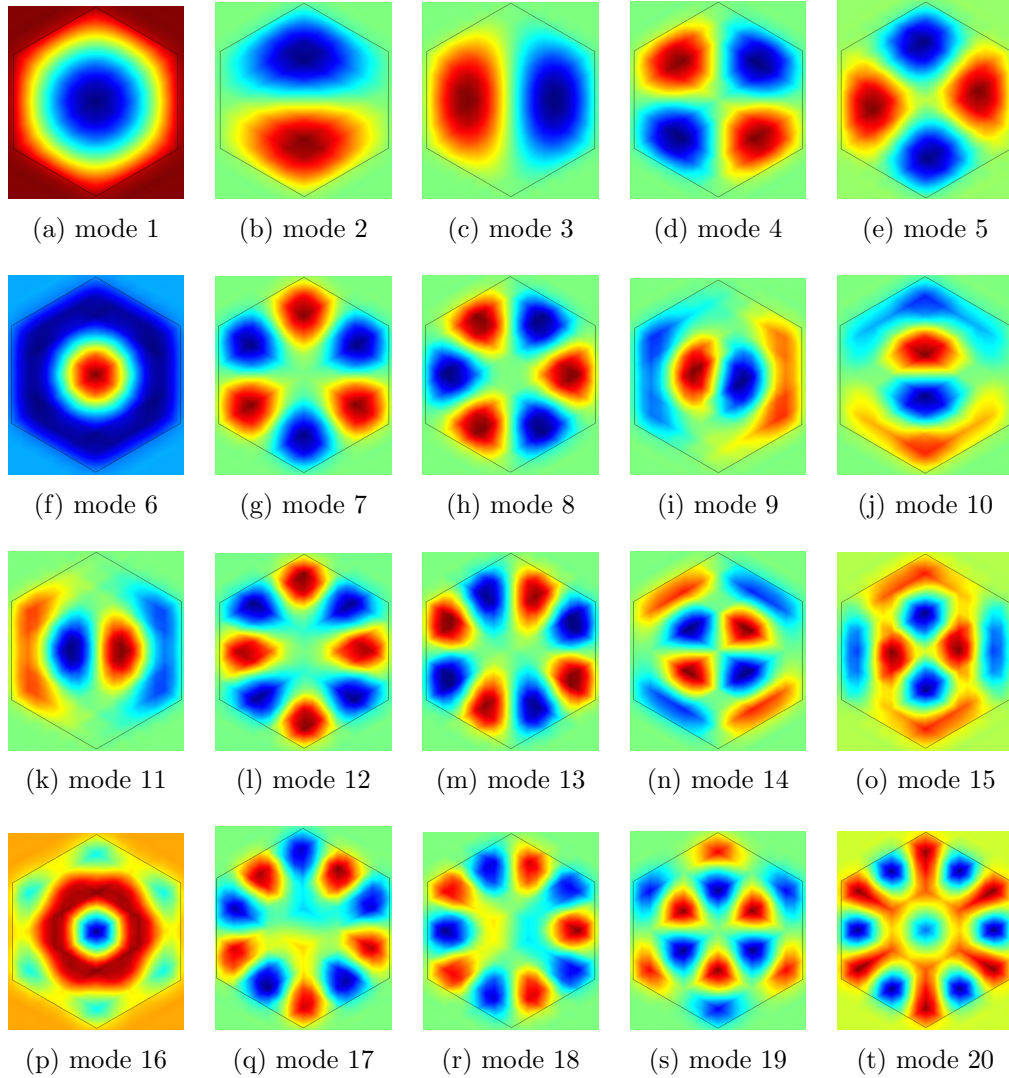


Figure 3.32: First 20 modes of a Hexagonal waveguide, side-side distance  $2\mu\text{m}$ ,  $\text{NA}=0.15$

### 3.11 Irregular guide

First a waveguide with elliptical cross-section is considered, where the major axis =  $2.2\mu\text{ m}$  and the minor axis =  $1.8\mu\text{ m}$  is taken. The first 20 modes of this elliptic waveguide are presented in Fig. 3.33. The mode patterns are more or less similar to that of the circular waveguide, but the interesting point to note here

that the first mode and the second mode have very similar characteristics in all these waveguide considered so far.

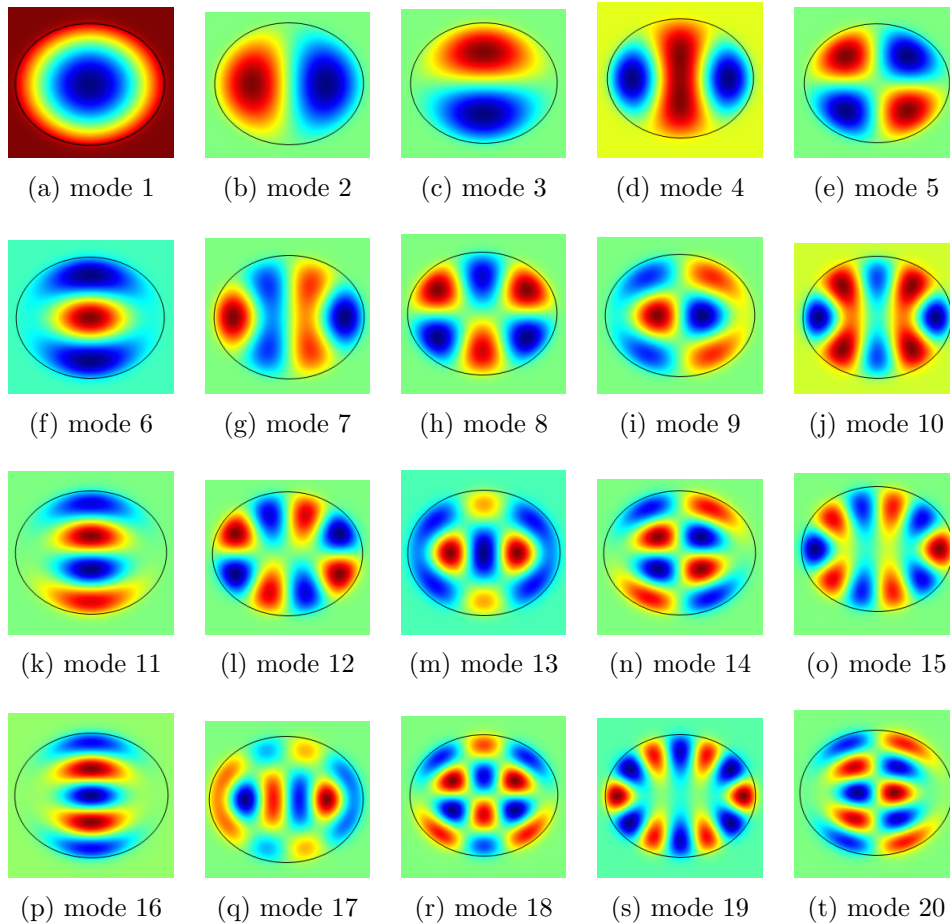


Figure 3.33: First 20 modes of a Elliptical waveguide, major axis  $2.2\mu m$ , minor axis  $1.8\mu m$ ,  $NA=0.15$

As the biological structures do not have pure geometric shapes in their structures, to analyse biological structures, it is required to analyse structures with irregular shapes. The hexagonal structures found in the biological structures are pseudo hexagon rather than pure geometric hexagon. However, the mode profiles of a pseudo-hexagonal waveguide should be very similar to that of pure hexagonal structure if the structural dimensions and the material profiles are similar. We have considered at this point a waveguide with an irregular cross-section that is

shown in Fig. 3.34.

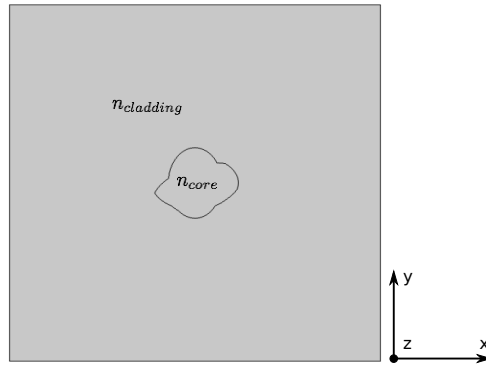


Figure 3.34: Guide having irregular cross-section Structure

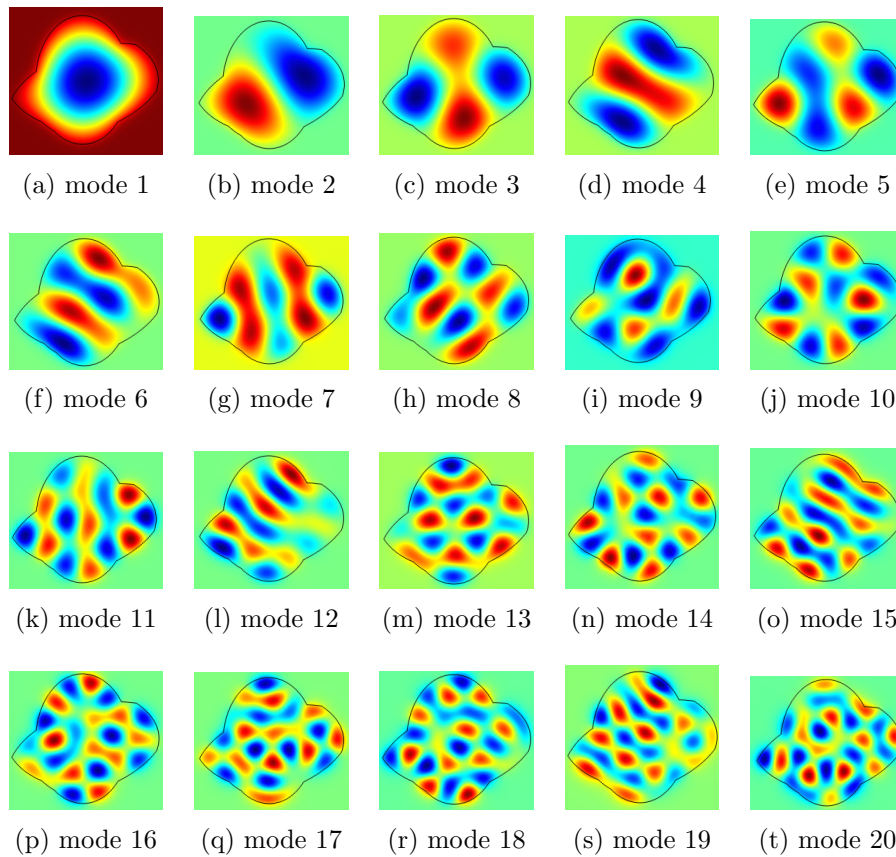


Figure 3.35: First 20 modes of a irregular cross-section waveguide, approximate dimension  $2\mu m$   $NA=0.15$

Figure 3.35 shows the field profiles obtained for the first 20 supported modes of the waveguide with an irregular cross-section. The first two modes have very similar field profiles as that of the other waveguide types.

### 3.12 Comparisons about the mode profiles of waveguides with different cross-sections

The fundamental or the lowest order modes of all these guides with similar dimensions have similar  $n_{eff}$ , indicating the phase velocities and the mode angles are similar. The field profiles are similar to some extent.

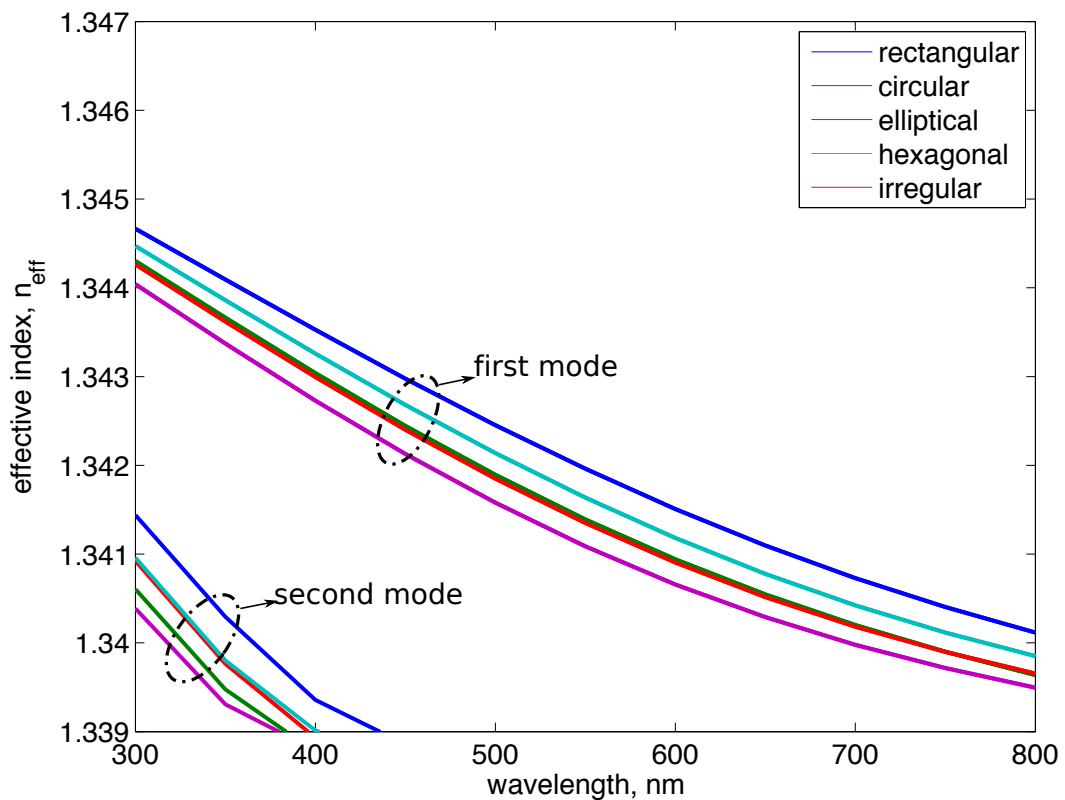


Figure 3.36: Structures and the propagation characteristics of the first and the second modes for the first mode of Rectangular, Hexagonal, Circular and irregular cross-sections with similar dimensions

Rectangular guides are usually analysed in Cartesian coordinates and the in

---

numbering the modes the field variations along X and Y directions are considered, i.e. an  $H_{32}^x$  mode has 3 variations in the X direction, and 2 variations in the Y direction, with  $H^x$  being the dominant field component as shown in the Fig. 3.37.

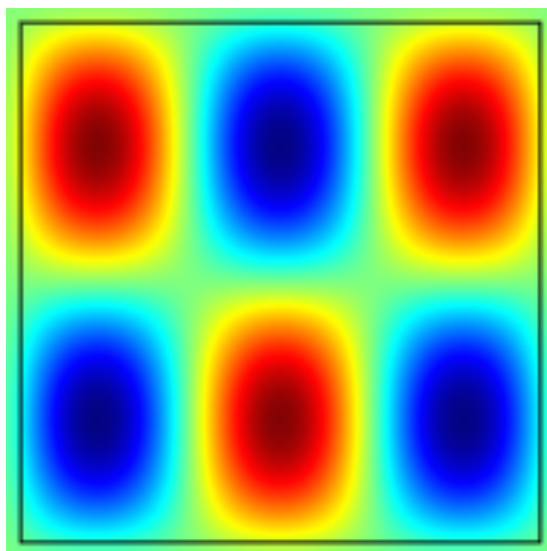


Figure 3.37:  $H_{32}^x$  field profiles for a rectangular waveguide

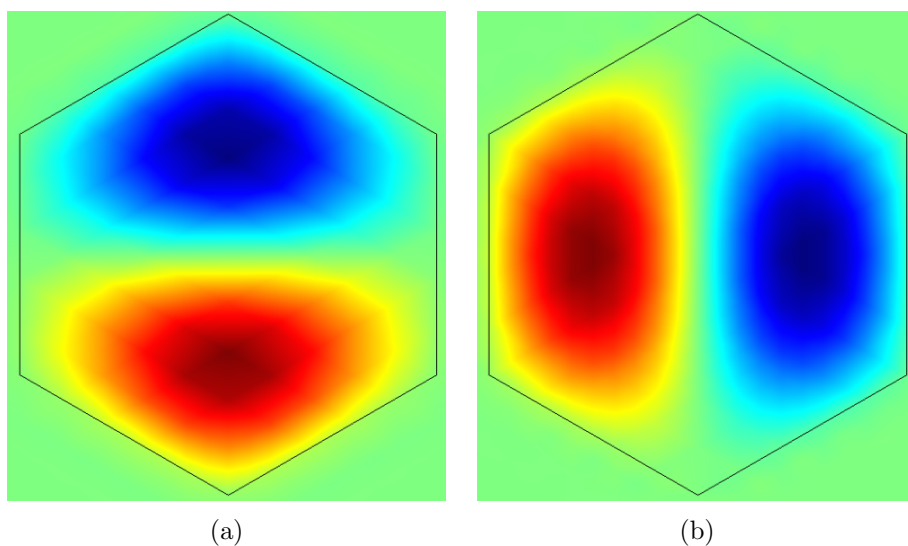


Figure 3.38: Different types of symmetries present in the field profiles of a Hexagonal guide

---

In analysing the circular guide, the Polar coordinate system is preferred over the Cartesian one, where the mode is considered to have radial ( $\rho$ ) and angular ( $\theta$ ) variations. A  $H_{32}^p$  mode has a dominant  $\rho$  component in the  $\mathbf{H}$  field, with three variations in the radial direction and two variations in the angular dimension.

The number of symmetries present in a Hexagonal guide makes it difficult to use the mode numbering scheme with Cartesian or Polar coordinate systems. [Bauer and Reiss \[1978\]](#) proposed a method of numbering the modes as  $mode_i$ ,  $i = 1, 2, 3, \dots$

Despite having one variation along  $\theta$ , modes as shown in the Fig. 3.38, are different, must have different  $n_{eff}$ . It has been found that the  $n_{eff}$  are very close to each other, but the propagation angles are much different. The hexagonal cross-section waveguide thus should be more sensitive to the polarisation than the other guide shapes. It has been reported that the eyes of some insects are sensitive to the polarisation of the light and it plays a vital role in their daily life; the study has the potential to shed some light on the matter.

### 3.13 Summary

This Chapter provides the derivations required in this study. The Chapter, first deals with a planar waveguide structure derive the necessary equations that represent the various field components considering lossless materials. The necessary equations for a planar waveguide structure are then derived considering the cladding material as lossy. Angle dependence of the waveguide modes is presented in this Chapter then. The propagation characteristics of waveguides with a different cross-section, i.e. Rectangular, Circular, Hexagonal, Elliptical and irregular, have been presented in the Chapter. Comparisons among the propagation characteristics of different waveguides are presented in the later parts of the Chapter. As the theoretical analysis is possible for the planar structure, the results obtained for the planar structure from the numerical methods are compared with the theoretical results to validate the numerical methods. For the more complicated structures where the theoretical analysis is complicated, numerical methods have been used in their study. This Chapter thus serves as a brief introduction to the various aspects related to the analysis of biological optical waveguide.

# Chapter 4

## Results and Discussion

This chapter provides the simulations results and discusses the implications of the obtained results. Theoretical derivations for planar waveguide structure is compared with the simulations results to justify the validity of the simulations results. As the theoretical analysis is extremely complicated, impossible in some cases, for 3D waveguides structures; results obtained from Numerical simulations has been presented. Effects of material loss on the propagation characteristics of optical waveguides have been explored after that. At the later parts of this chapter, the impacts of multi-layer waveguide structures and the presence of the surrounding waveguides on the propagation characteristics have been provided. The results obtained from the different waveguide structures is then utilised to explore in characterising the Ommatidium of *Drosophila Melanogaster*'s Compound eye and the Glial cell of Human Retina. An explanation of the Stiles-Crawford effect of Human eye is provided at the end of this chapter.

### 4.1 Planar Waveguide

In a planar waveguide, the core with higher refractive index ( $n_2$ ) is sandwiched between the upper cladding ( $n_1$ ) and lower cladding ( $n_3$ ) having lower refractive indices than the core. In a symmetric structure, we assume that  $n_1 = n_3$  and  $n_2 > n_1$ . The schematics of a planar structure is found in Fig. 4.1, where the direction of propagation is considered along the  $z$  direction and the waveguide is

infinitely extended along the  $y$  direction; as a result we assume that the variation of the field along the  $y$  direction is zero ( $\frac{\delta}{\delta y} \rightarrow 0$ ).

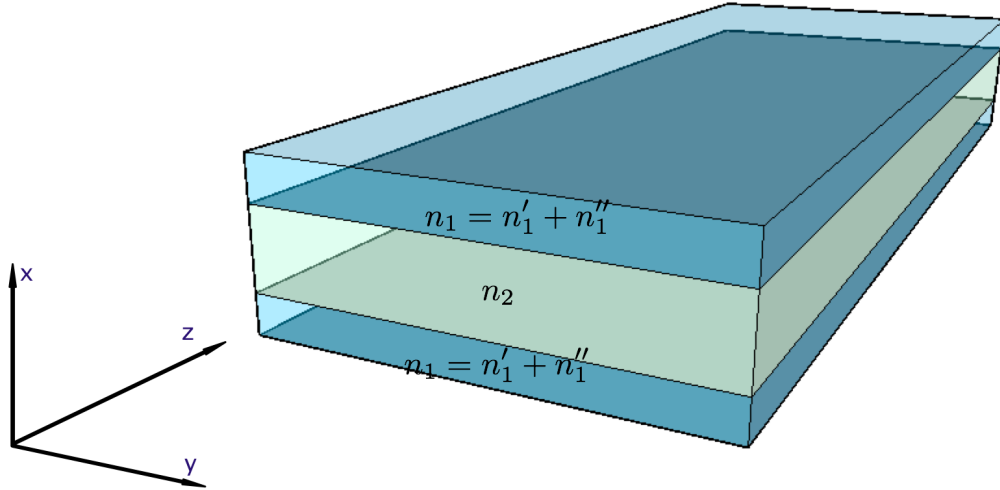


Figure 4.1: Schematics of a planar waveguide

## 4.2 Waveguides with Lossy Materials

In the previous chapter, propagation characteristics of waveguides having lossless material have been considered. In most of the practical cases the waveguide materials are not lossless because the material loss is tiny for dielectric materials ( $SiO_2$ , MICA, Quartz) and semiconductors, typically  $\tan \delta \approx 10^{-4}$ , the effects of loss on the propagation characteristics can be ignored. It has been shown in Chapter 4 that the material loss of the waveguide material has profound effects on the propagation characteristics. In this chapter, the impact of material loss on different aspects of waveguide characteristics will be explored. As the waveguides having various types of the cross-section (i.e. Rectangular, Hexagonal, Circular, and Irregular) have similar propagation characteristics as well as the field profiles as far as we restrict our attention to the lowest order mode, the majority of the results in this chapter is on rectangular guide unless specified otherwise. The core is considered to be loss-less with real refractive index  $n_{core}$ , the cladding is lossy with complex refractive index  $n_{cladding} = n_{real} + jn_{imag}$ , Fig. 4.2 shows the

---

schematics of the cross-section of the waveguide in XY plane, where the direction of propagation is considered to be in the z direction. To observe the effects of loss, we assume  $n_{core} = 1.347$ ,  $n_{real} = 1.339$  and  $n_{imag}$  is varied for obtaining different  $\tan \delta$  that is defined as,

$$\tan \delta = \frac{2n_{real}n_{imag}}{n_{real}^2 - n_{imag}^2} \quad (4.1)$$

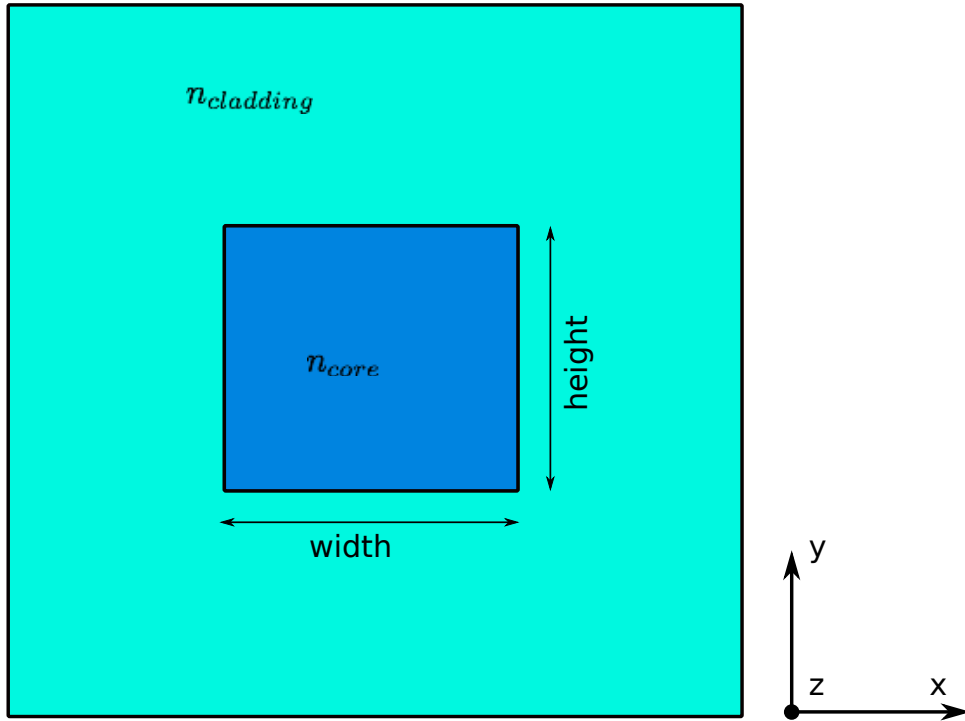


Figure 4.2: Schematic diagram of the XY plane cross-section of a rectangular guide with lossless core and lossy cladding materials

### Propagation Characteristics

Figure 4.3 shows the normalised effective index (b) with respect to normalised frequency ( $v$ ) for different  $\tan \delta$  curves for the  $H_x^{11}$  mode or the lowest order quasi-TM mode of a rectangular guide with  $2\mu m \times \mu m$  cross-section dimension. As the frequency is increased, or, in other words, the wavelength is decreased,

the effective index,  $n_{eff}$  is increased. An increase in the  $n_{eff}$  means the mode is more confined to the core and there is room for possible higher order modes with lower  $n_{eff}$ . As we increase the  $\tan \delta$ , the figure shows that the  $n_{eff}$  is decreased. A possible consequence for this lowered  $n_{eff}$  is less room for the higher order modes. The curves for  $\tan \delta = 0$  and  $\tan \delta = 0.0015$  seems to be very similar that proves that our previous assumptions that very little materials loss have a negligible impact on the propagation characteristics.

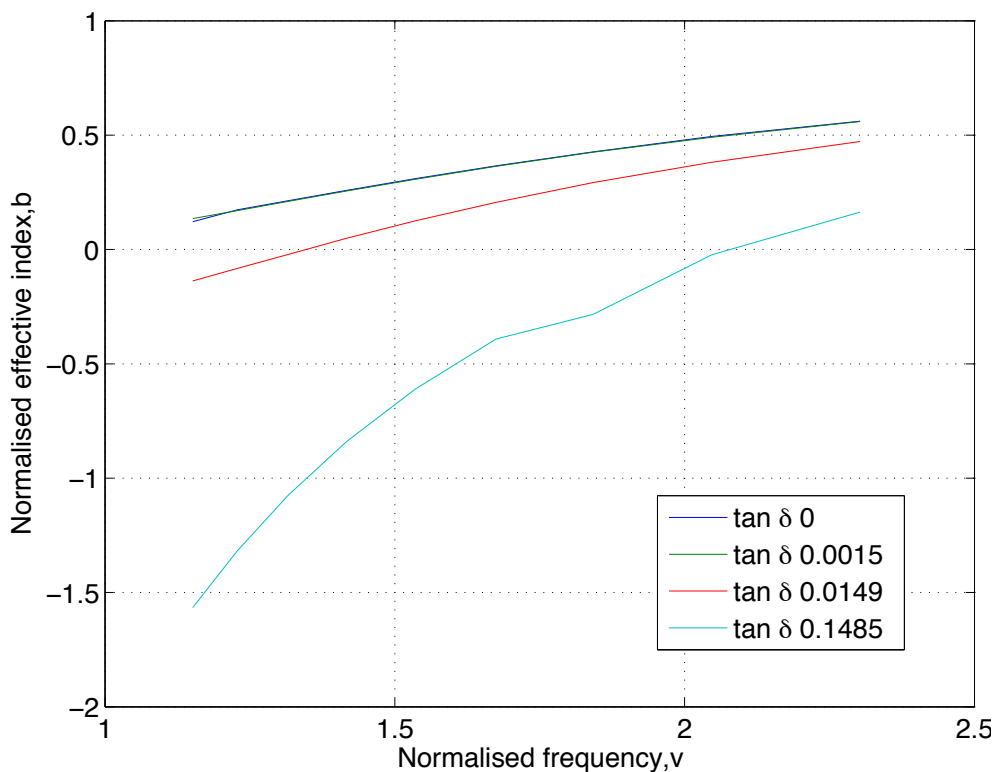


Figure 4.3: Normalised  $n_{eff}$  vs normalised frequency of  $H_x^{11}$  mode ( $v$ ) for a  $2 \times 2 \mu m$  rectangular waveguide for different  $\tan \delta$ ,  $n_{core} = 1.347$ ,  $n_{cladding} = 1.339$

An increase in the loss part of the cladding refractive index ( $\tan \delta$ ) results in a decrease in the real part of the effective index ( $n_{eff}$ ) at the same time an increase in the imaginary part of  $n_{eff}$ . Figure 4.4 shows that, for a loss-less cladding, or when the loss is very low ( $\approx 10^{-8}$ ), for a rectangular guide having a dimension of  $2 \mu m \times 2 \mu m$ , the real part of  $n_{eff}$  of the lowest order mode is about 1.342 and the imaginary part is  $\approx 0$ . For  $\tan \delta > 10^{-4}$ , the real part of the  $n_{eff}$

starts to decrease, while the imaginary part starts to increase. A decrease in the  $\text{Real}\{n_{eff}\}$  means an increase in the phase velocity of the propagating mode as well as a decrease in the tangential components of the field components. As the  $\text{Imag}\{n_{eff}\}$  represents the loss experienced by the propagating mode, an increase in the imaginary part represents an increase in mode power loss. At this point, it can be asked, “What would happen if we continue to increase the material loss?” . For an extremely high value of material loss  $\tan \delta > 0.15$ , the modal loss shows interesting characteristics that would be shown later in this chapter.

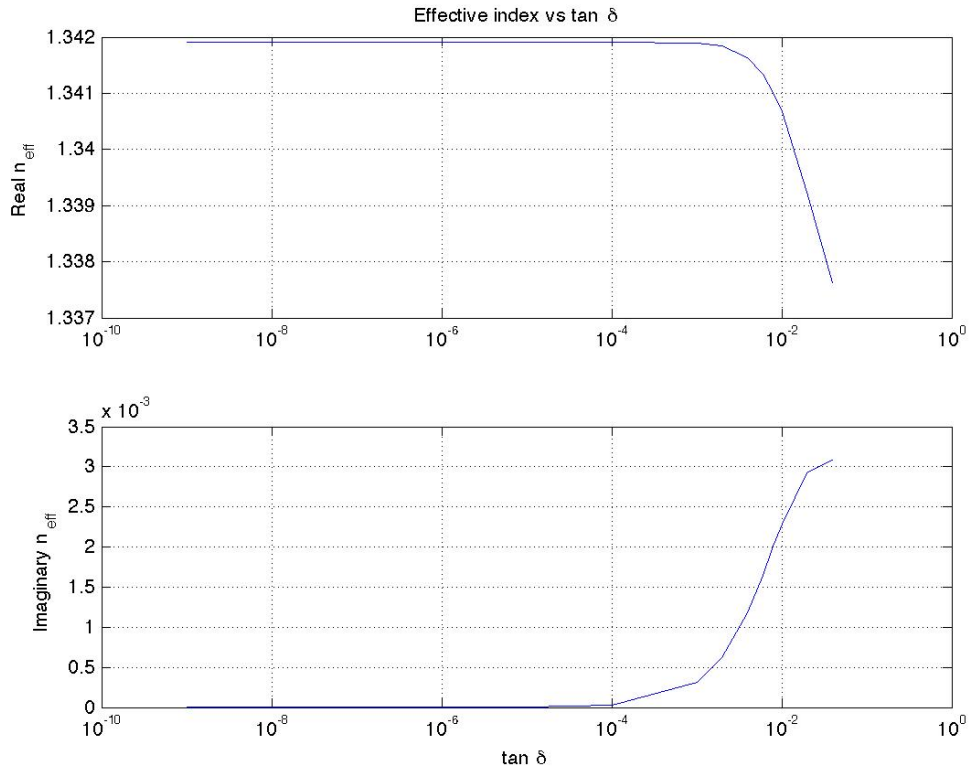


Figure 4.4: Effective index vs Loss tangent for Rectangular guide with  $2 \mu\text{m} \times 2 \mu\text{m}$  dimension,  $n_{core} = 1.347$ ,  $n_{cladding} = 1.339$ ,  $\lambda = 550 \text{ nm}$  FEM simulation

A waveguide with lossy dielectric (complex refractive index) has its effective index ( $n_{eff}$ ) as a complex number, implies that the propagating mode is lossy. In analysing such lossy waveguides, several FEM-based numerical methods capable of producing complex effective index can be deployed. Two of these methods are

full vectorial FEM mode solver using complex eigenvalue solver CSSITER [Rahman and Agrawal \[2013\]](#) and using perturbation method [Rahman and Agrawal \[2013\]](#).

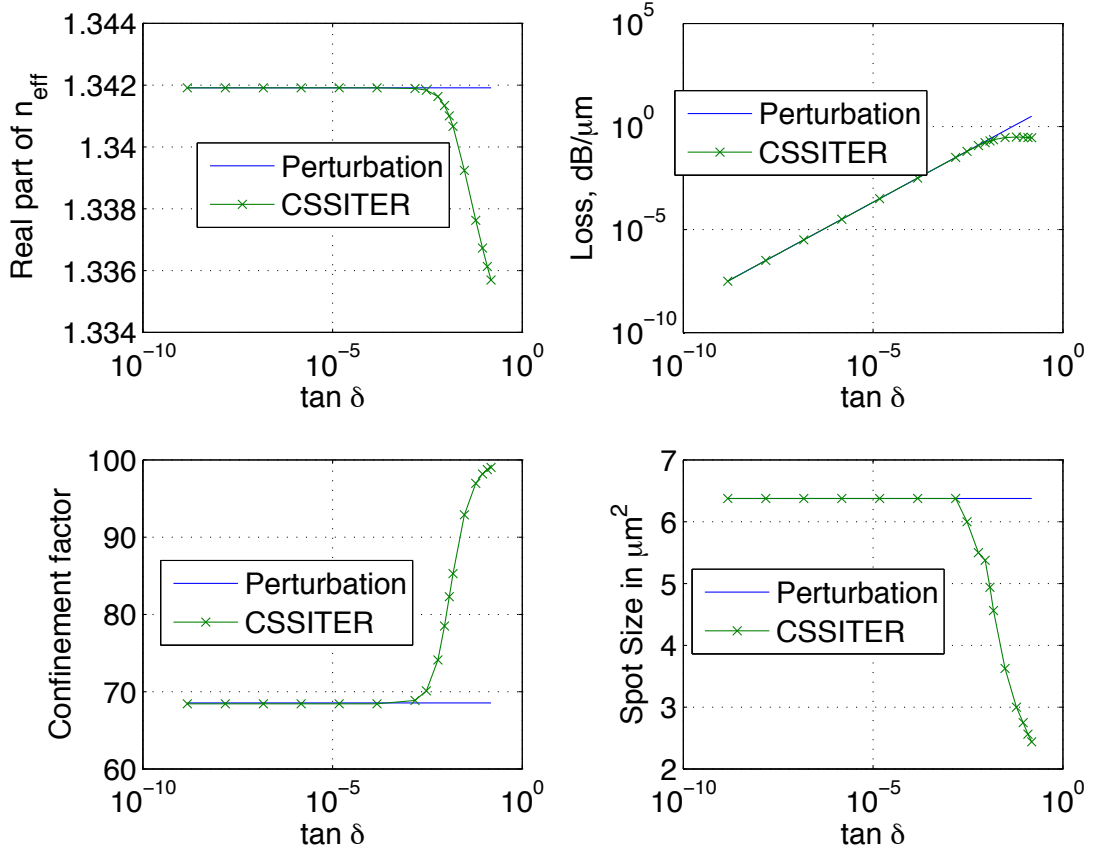


Figure 4.5: Propagation characteristics vs Loss tangent for  $d=2\mu\text{m}$ ,  $\lambda=550\text{ nm}$ , Rectangular guide

Perturbation method uses a real solver ignoring the imaginary parts initially, then tries to determine the imaginary part based on the real part and an integration performed over the structural domain while the CSSITER is capable of dealing with the complex quantity as it uses a complex eigenvalue solver. Figure 4.5 shows the propagation characteristics of the  $H_{11}^x$  mode of a rectangular dielectric waveguide with a dimension of  $2\mu\text{m} \times 2\mu\text{m}$ , wavelength,  $\lambda = 550\text{ nm}$  where, the top left figure shows the real  $n_{eff}$  vs  $\tan \delta$ , the top right figure shows the loss vs  $\tan \delta$ , the bottom left one displays the field confinement factor vs

$\tan \delta$  and the bottom right graph shows the mode spot size vs  $\tan \delta$ . As evident from all the sub-figures of Fig 4.5, there is good agreement between the results produced by the two methods as mentioned earlier as long as the material loss stays minuscule, more precisely  $\tan \delta < 10^{-3}$ . At higher material loss values, the two methods produce significantly different results. There is a good agreement between the results obtained from CSSITER with the other commercially available Softwares such as COMSOL at higher loss values. These findings suggest that despite being computationally less costly, the Perturbation method is not a suitable candidate if higher losses are sought.

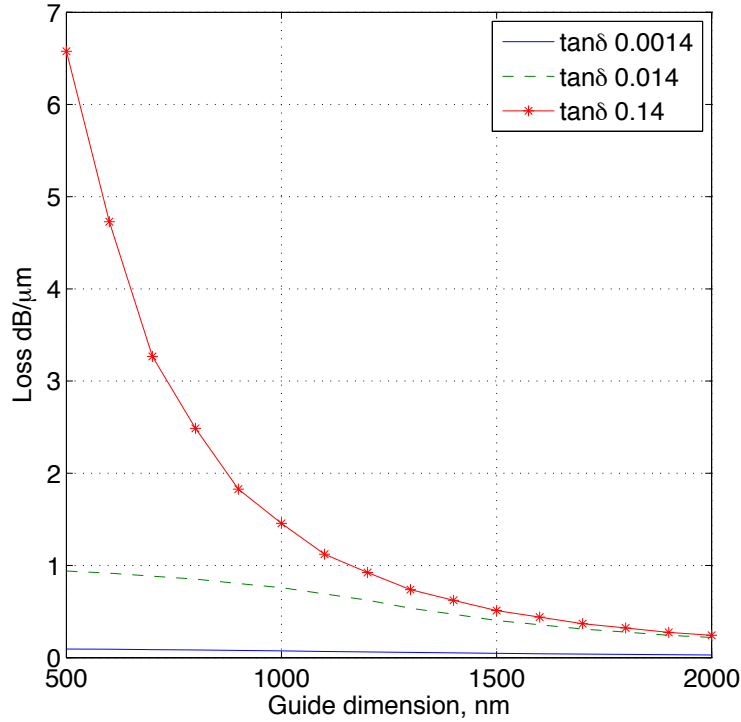


Figure 4.6: Loss vs Guide Width ( $d$ ) for Different Loss Tangents,  $n_{core} = 1.347$ ,  $n_{cladding} = 1.339$ ,  $\lambda = 550$  nm

Waveguide loss, in this thesis expressed in  $dB/\mu m$ , not only depends on the material loss but also on the waveguide dimensions or more precisely on  $d/\lambda$  ratio, where  $d$  stands for the waveguide cross-section dimension and  $\lambda$  is the operating wavelength. Higher ratio leads to lower guide loss. Loss values calculated against a range of guide dimensions for a rectangular waveguide with  $n_{core} = 1.347$ ,

$n_{cladding} = 1.339$ ,  $\lambda = 550$  nm, using CSSITER has been presented in Fig. 4.6. It is clear from the figure that as we increase the  $d/\lambda$  ratio, the guide loss decreases. An increase in the material loss keeping the  $d/\lambda$  ratio leads to higher guide loss. By choosing the three parameters ( $d$ ,  $\lambda$  and  $\tan \delta$ ), it can be possible to set a waveguide at any desired guide loss condition.

It has been shown in Fig. 4.4 that an increase in waveguide material  $\tan \delta$  results in a reduction in  $n_{eff}$ , where the operating wavelength was kept constant at  $\lambda = 550$  nm. The visible spectrum is referred to the wavelength range of 390 nm-740 nm. To analyse the performance of any waveguide device that works in the visible spectrum has to be evaluated for the entire spectrum if possible. The wavelength range has been taken as 350 nm-750 nm to include the visible spectrum, and for this wavelength range the real part of the  $n_{eff}$  is presented in

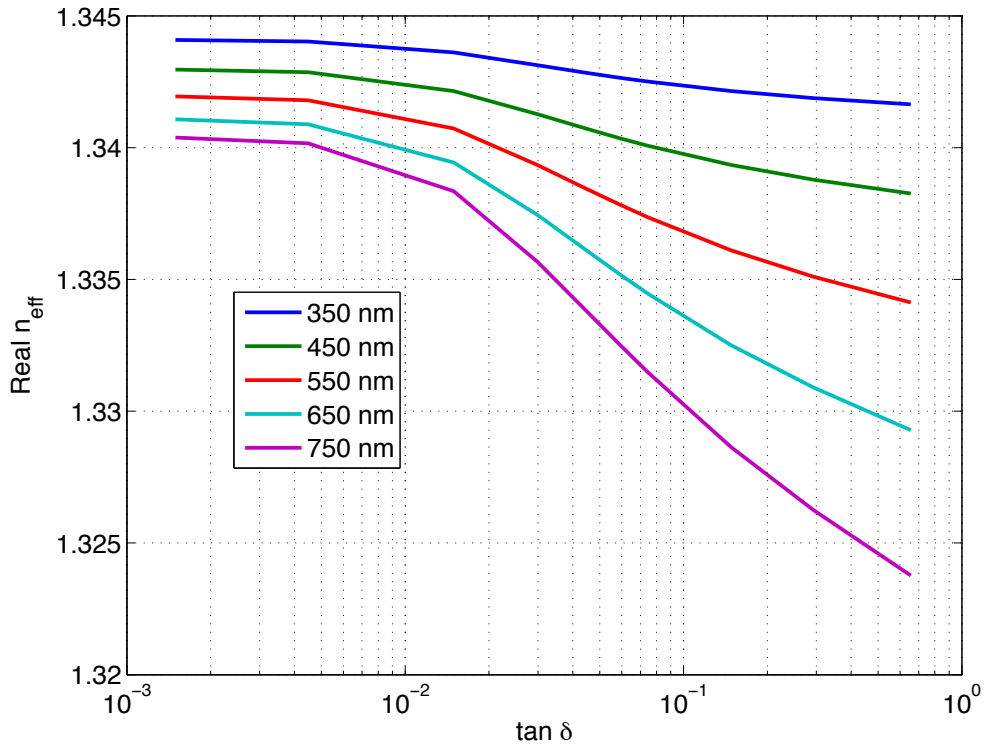


Figure 4.7: Real  $n_{eff}$  vs  $\tan \delta$  for different wavelengths for a  $2 \mu m \times 2 \mu m$  rectangular waveguide,  $n_{core} = 1.347$ ,  $n_{cladding} = 1.339$

Fig. 4.7 for the waveguide with same parameters as before. For all wavelengths

in the range increase in  $\tan \delta$  means a decrease in the real  $n_{eff}$ . Longer wavelength at the same  $\tan \delta$  leads to lower  $\text{Real}\{n_{eff}\}$ . Figure 4.8 shows the variations of the imaginary parts of the  $n_{eff}$  against  $\tan \delta$  at various wavelength in the same wavelength range. The simulation is done, at this instance, for  $\tan \delta$  value as high as 0.5. The interesting point to note that the imaginary parts of  $n_{eff}$  continue to increase with increasing  $\tan \delta$  up to a certain value of the material loss, but starts to decrease beyond that point with further increase in the material loss. Increase in the operating  $\lambda$  results in a rise in the  $\text{Imag}\{n_{eff}\}$ , consequently increase in the waveguide loss as the waveguide loss is directly proportional to the imaginary part of  $n_{eff}$ . It has been shown before that the field confinement of a guided mode increases with  $\tan \delta$  of the cladding material. It is possible to achieve the same waveguide loss with other field confinements by adjusting the cladding material loss.

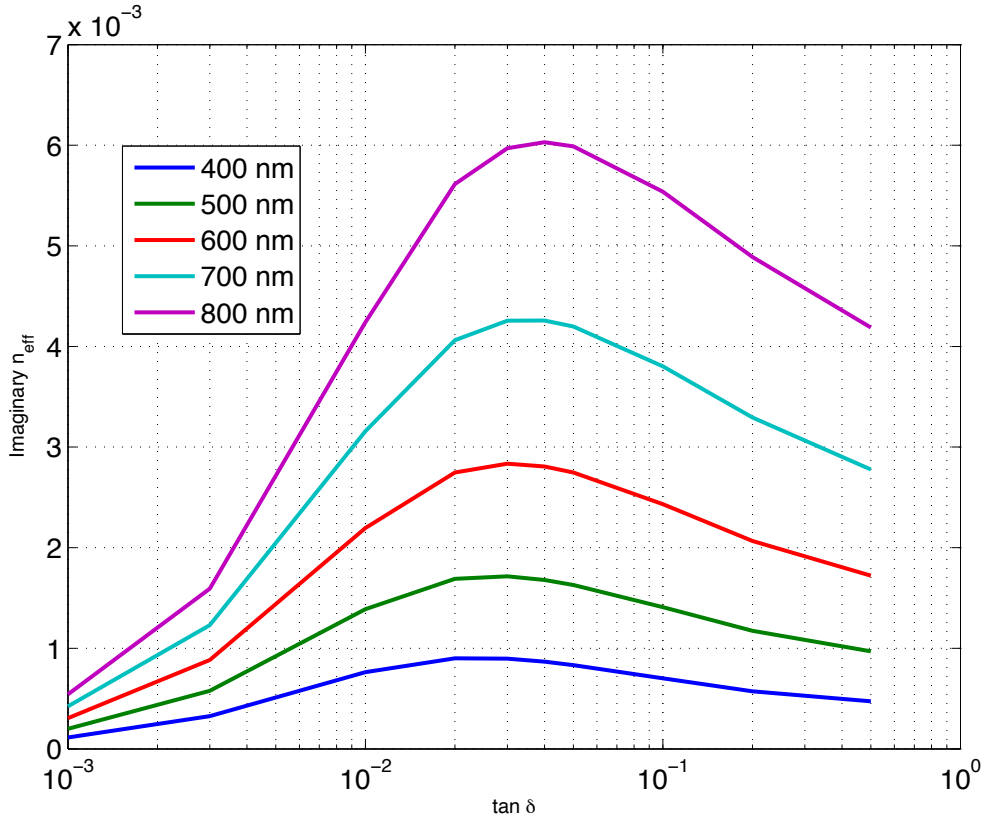


Figure 4.8: Imaginary  $n_{eff}$  vs  $\tan \delta$ , for a  $2 \mu\text{m} \times 2 \mu\text{m}$  rectangular waveguide,  $n_{core} = 1.347$ ,  $n_{cladding} = 1.339$  at different wavelengths

---

### Effects on Field Profile

Typically the mode profile of a rectangular dielectric waveguide can be represented by sinusoidal variations in the core and exponentially decaying fields for the evanescent field in the cladding. It has been shown in Chapter 4 that a Gaussian profile can approximate the lowest order mode for a planar dielectric waveguide for a lossless case and lossy cladding the field profile at the core is exponentially decreasing sinusoid, the field profile at the cladding is exponentially decreasing sinusoid as well. There is good agreement between the theoretical and the numerical results for the planar waveguide. As the rectangular waveguide can be considered as an extension of the planar waveguide, the similar types of field profile should be found for the rectangular case as well. As was shown in Chapter 4 that there are similarities, at least amongst the lowest order modes, in field profiles for rectangular, circular, hexagonal and irregular cross-section waveguides, from the results shown for the rectangular case can be used to conclude for the other waveguide types as well.

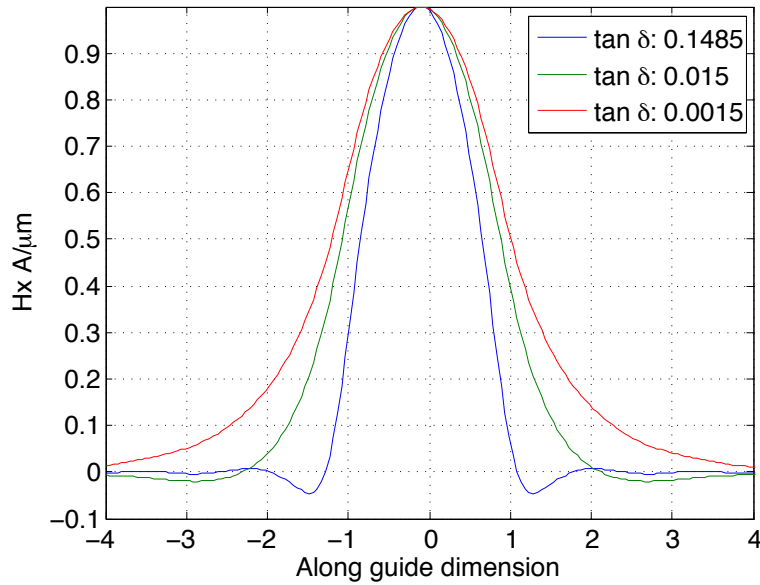


Figure 4.9:  $H_x$  along dimension for Different Loss Tangents, for a  $2 \mu\text{m} \times 2 \mu\text{m}$  rectangular waveguide,  $n_{core} = 1.347$ ,  $n_{cladding} = 1.339$

Numerical simulations performed on a waveguide with rectangular cross-section has been used to determine the field profile along the guide axis of the lowest or-

der  $H_x^{11}$  mode is presented in Fig. 4.9. Waveguide cross-section, in this case, like the preceding section, is taken as  $2 \mu m \times 2 \mu m$ , with the similar material profile. It is evident from the Fig. 4.9 that the field profile is comparable to a Gaussian profile for a lossless case, as the  $\tan \delta$  is increased the core shows exponentially decreasing sinusoidal profile and the cladding shows sinusoidally varying exponentially decreasing profile. With increasing  $\tan \delta$ , the field is more confined to the core. Figure 4.10 displays the impacts of the loss present in the cladding material upon the field profile, which clearly indicates that an increase in the material loss pushes the modal field towards the centre of the waveguide, thereby increases the field confinement.

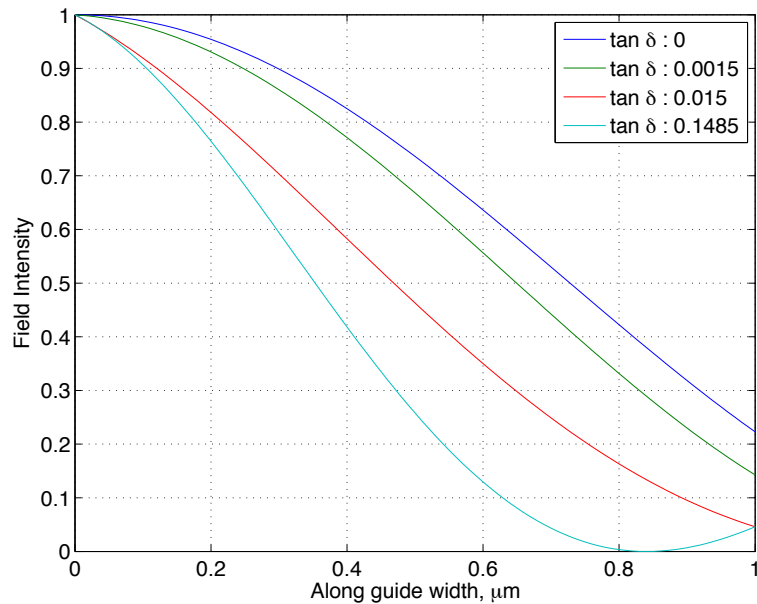


Figure 4.10: Field intensity along guide width for Rectangular guide with  $2 \mu m \times 2 \mu m$  dimension

### Dispersion

In Optics, dispersion [Cole and Cole \[1941\]](#) is referred to the phenomenon in which the phase velocity of a wave depends on its frequency. Usually, most of the materials are dispersive in nature for a wide band of frequencies. An optical instrument that operates in the visible spectrum (390 nm-750 nm) experiences dispersion as the operating wavelength band is quite wide; thus, the design of

such an instrument must take the effects of dispersion into active consideration. Dispersion of an Optical waveguide depends not only on their material dispersion but also on their geometry. Dispersion of an Optical waveguide is given by,

$$D = -\frac{2\pi c}{\lambda} \frac{d^2\beta}{d\omega^2} \quad (4.2)$$

where  $\lambda = 2\pi c/\omega$  is the vacuum wavelength,  $c$  is the speed of the wave in free space, and  $\beta = \frac{2\pi}{\lambda} n_{eff}$ . Equation 4.2 is the generalised case where the waveguide dispersion and the material dispersion both are taken into account.

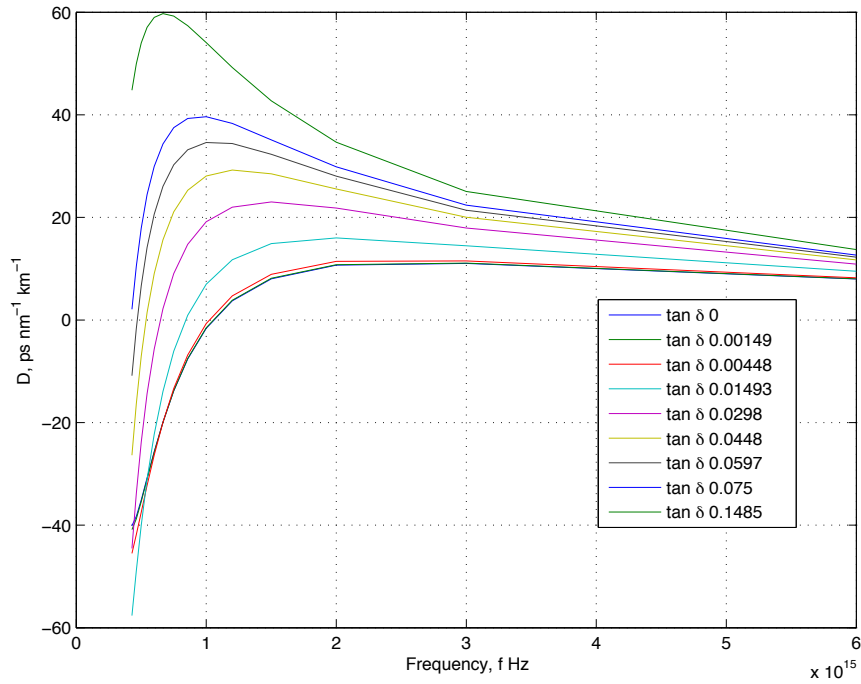


Figure 4.11: Dispersion vs Frequency for a  $2\mu\text{m}$  Rectangular guide for different  $\tan \delta$

Figure 4.11 presents the waveguide dispersion curves for a rectangular waveguide ( $2\mu\text{m}$  dimension) over a wide range of frequencies ( $50\text{ nm} - 800\text{ nm}$ ) for different  $\tan \delta$ . The visible spectrum is defined as the frequency range of  $0.4 \times 10^{15}\text{ Hz}$  to  $0.75 \times 10^{15}\text{ Hz}$ . As seen in the figure, the waveguide is highly dispersive in the visible frequency band, suggests that the waveguide works in this range would be affected severely by the dispersion. Any broadband pulse propagates

---

through the waveguide would experience pulse broadening as a result of this dispersion. A flatter dispersion curve in the wavelengths under consideration means less broadening of the propagated pulse. As we increase the material loss of the cladding material, the dispersion curve becomes more and more flat, indicating the reduction in the pulse broadening at the expense of the modal loss.

### Cutoff wavelength ( $\lambda_c$ )

Depending upon the waveguide dimension, operating wavelength and the material profiles of an optical waveguide, several waveguide modes are supported. For a rectangular waveguide the lowest order mode can be  $H_{11}^x$  or  $H_{11}^y$  depending upon the dominant field component where the  $H^x$  field is dominant in the former and the  $H^y$  field is dominant in the later case; along X and Y direction there is no zero crossing of the field components. The subscript represents the number of variations in X and Y direction respectively, so any subscript higher than 1 represents higher order modes. According to [Senior and Jamro \[2009\]](#), the normalised frequency  $v < 2.405$  ensures that the waveguide supports only the lowest order or the fundamental mode. The normalised frequency is defined as,

$$v = \frac{\pi d}{\lambda} NA \quad (4.3)$$

where, the  $NA = \sqrt{n_{core}^2 - n_{cladding}^2}$  is the numerical aperture,  $d$  is the waveguide diameter, and the  $\lambda$  is the operating wavelength.  $\lambda_c$  denotes the wavelength at which the waveguide is marginally single-moded (a further reduction in wavelength supports the second mode).

Figure 4.12 shows the propagation characteristics for the first two lowest order modes of a waveguide having a numerical aperture  $NA = 0.146$ . The results demonstrate that the waveguide remains single-moded up to the normalised frequency  $v \approx 2.4$ , an increase in  $v$  beyond that value, means an increase in the  $d/\lambda$  ratio, leads to more than one supported modes. If it is sought that the waveguide to operate as single-moded over the operating frequency range, we have to make sure that the condition  $v < 2.405$  is satisfied by adjusting the waveguide parameters. It is evident from Fig. 4.12 that as the  $\tan \delta$  is increased the cut-off normalised frequency,  $v_c = \frac{\pi d}{\lambda_c} NA$ , is increased. Higher cladding loss allows the waveguide to operate in the single-moded condition for smaller wavelengths

(higher frequencies) keeping the waveguide dimension ( $d$ ) and the numerical aperture  $NA$  the same.

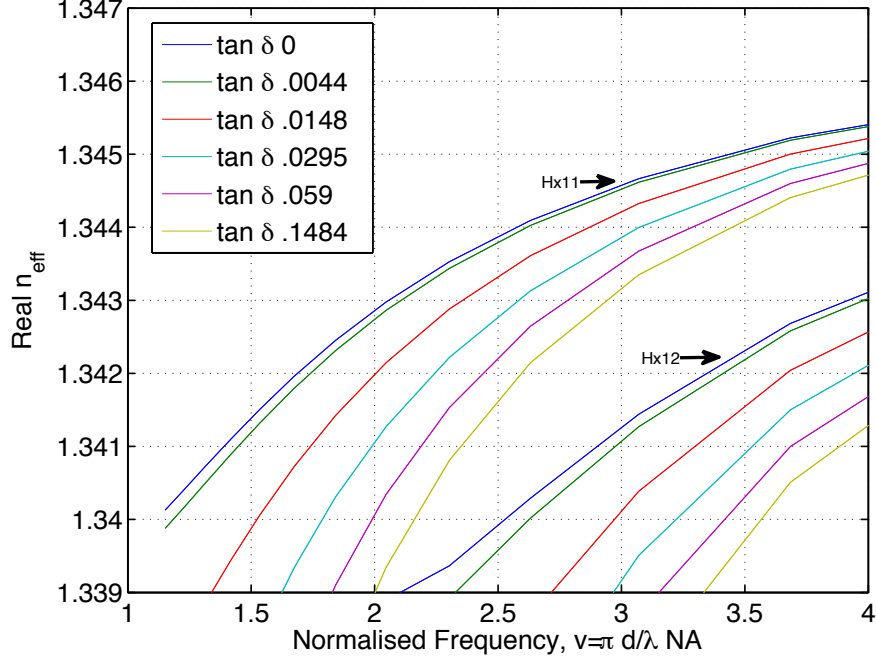


Figure 4.12: Effective index for the first 2 modes with different loss tangents

### Effects on Confinement Factor and Waveguide Loss

Several factors i.e. field confinement factor, material loss, field shapes, the magnitude of the evanescent field, etc., affects the loss experienced by a mode propagated through an Optical waveguide. For ideal case (no imperfections at the core-cladding interface, no bending) for a waveguide having lossless dielectric material, a supported mode does not suffer loss even though the evanescent field might be present in the cladding material. If the cladding material is lossy, the presence of the evanescent field present in the cladding introduces loss to the guided mode. In this case, the confinement factor (equation 4.4) plays a significant role in the Loss experienced by the propagating mode. Higher confinement factor means that more field to be confined to the core region, as the core is considered to be lossless in this study, the contribution to the Loss is only from the field that is propagating through the lossy cladding material, thereby higher

confinement tend to reduce the modal loss. Figure 4.13 shows the confinement factor and the waveguide loss against  $\tan \delta$  of the cladding material. The field confinement factor shows that it is increasing with increasing  $\tan \delta$ . This phenomenon can be explained considering the extreme case of a perfect conductor (if the cladding is considered to be a perfect metal, a metallic waveguide filled with dielectric core), where the conductivity,  $\sigma \rightarrow \infty$ , loss tangent,  $\tan \delta \rightarrow \infty$ , the field should be 100% confined in the dielectric core. The tangential components of the fields at the dielectric-metal interface according to [Rahman and Agrawal \[2013\]](#) should be zero. As the loss tangent increases, the field components of the at the core-cladding interface should decrease as we are approaching towards the metallic case. Consequently, the field confinement should increase. There is good agreement between our explanation on the confinement factor and the simulation results shown in Fig. 4.13.

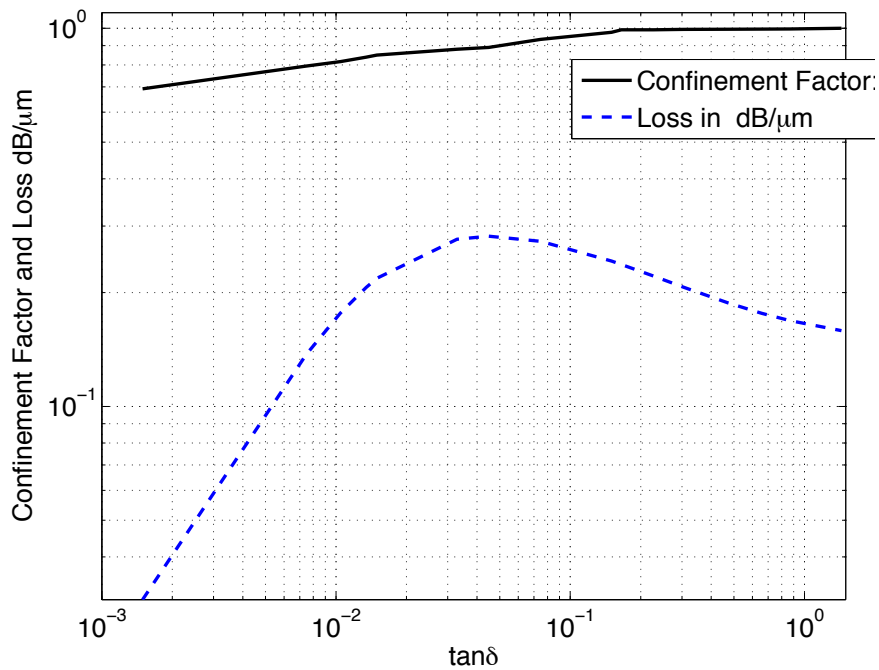


Figure 4.13: Confinement factor and Loss vs  $\tan \delta$

The Fig 4.13 also shows that when the cladding material is lossless, the propagating mode experiences no loss, as we continue to increase  $\tan \delta$  the guide

---

loss continue to rise to a certain value of the loss, beyond that point the guide loss starts to drop with further increase in the cladding material loss. The reason behind this phenomenon might be the fact that beyond the maximum loss point, the confinement factor starts to dominate over the loss contributed by the material-evanescent field interaction. It is possible set the waveguide to a point where, the propagating mode experiences same amount of loss to that of a less lossy cladding case, but we can achieve higher confinement factor that can be very useful in controlling the coupling amongst the neighbouring waveguides in case we have a waveguide array instead of a single waveguide.

$$\text{Confinement Factor} = \frac{\text{Power in the Core}}{\text{Total Mode Power}} \quad (4.4)$$

### 4.3 Waveguide Array

The most common form of optical waveguide in use at present in the world is the Optical fibre, unless it is a multicore fibre, it is generally composed of a core having higher refractive index ( $n_{core}$ ), a cladding having lower refractive index ( $n_{cladding}$ ), and it is considered that the field magnitude beyond the cladding region is zero, although theoretically a tiny value of the field can be present even at the infinity. So, for a single core optical fibre, or a waveguide having a single core and a thick cladding region, does not suffer interference of field from other structures. In case another core is introduced in the vicinity of the optical waveguide core, there is a possibility of power transfer between the waveguides and this phenomenon can be explained by coupled mode theory presented by Yariv [1973]. Even and odd supermode excited in the two waveguide cores interact with each other and the power transfer takes place from the one core to the other. The Coupling Length ( $L_c$ ) is referred to as the distance at which the entire power from one waveguide is transferred into the other core and is defined as,

$$L_c = \frac{\pi}{\beta_e - \beta_o} \quad (4.5)$$

where,  $\beta_e$  and  $\beta_o$  are the propagation constants of the even and odd supermodel respectively. Usually, a smaller separation between the waveguide core leads

to a smaller coupling length. This phenomenon of power transfer between the waveguides present at a short distance can be a catastrophe if it is required to send two different signals through the two waveguides. Lower  $L_c$  means lower guide length at which signals can be transferred successfully without being affected by the signal of the neighbouring guide. If the number of neighbouring guide increases, the impact would be more. If we consider an array of such waveguide where, similar guides surround each guide, it would be interesting to study the behaviour and the impacts on the propagation characteristics. The boundary condition suitable for studying these types of structures would be to consider a single guide with the periodic boundary condition at the computational boundary.

### Propagation Characteristics

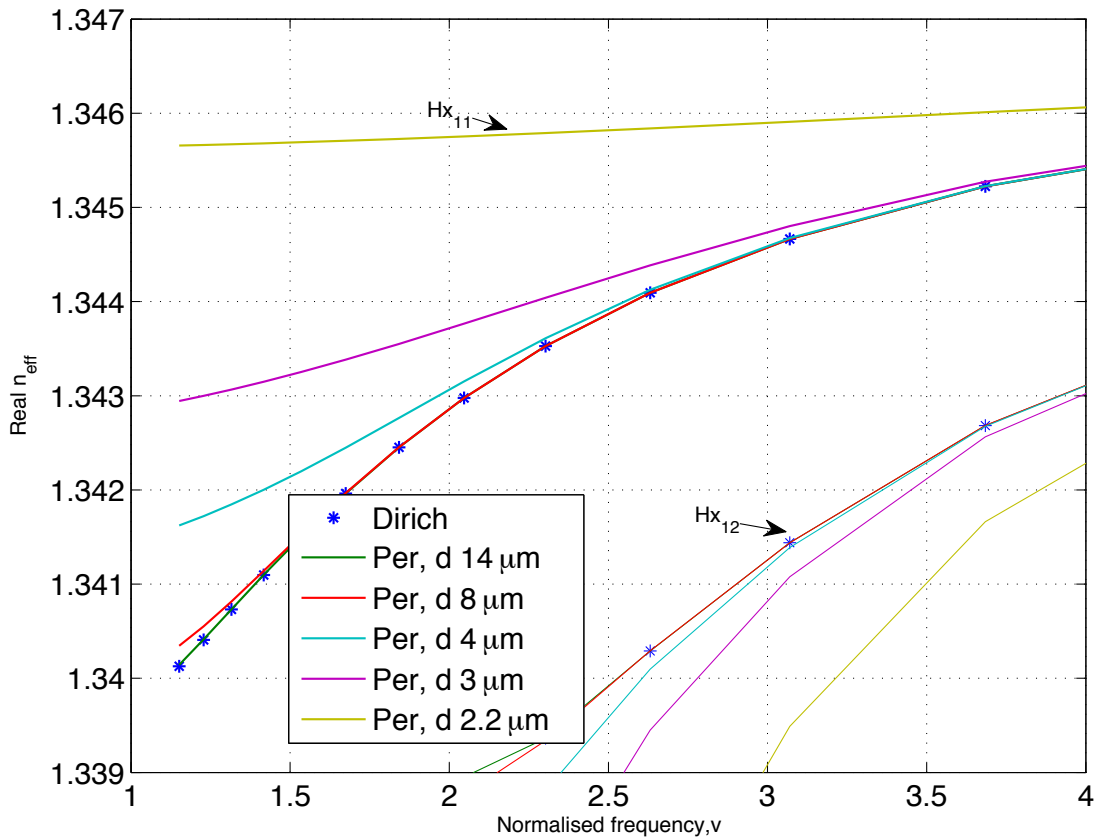


Figure 4.14: Effective index for the first 2 modes with different Guide separation,  $d$

The propagation characteristics of a rectangular waveguide using periodic

---

boundary condition are presented in Fig. 4.14. Here the parameter  $d$  is the distance between the edge of the waveguide core and the edge of the neighbouring guide core and is denoted by 'Per'. A very high value of  $d$  means the neighbouring guide is far away and the interaction between them can be considered negligible; it has been assumed that a 'Per'=14 (Guide dimension 2) as the condition for a single core guide with no surrounding guides. As can be seen in the figure, reducing the distance between the neighbouring guides results in an increase in the effective index of the lowest-order mode, while a decrease in the effective index of the second mode. This result indicates that the gap between the first and the second mode of being widens as we reduce the separation between the waveguide cores. Moreover, this implies also that the single mode cutoff wavelength ( $\lambda_c$ ) decreases, thereby we have a wider range of frequencies at which the guide remain single-moded. Decreasing  $d$  would make the coupling length ( $L_c$ ) be decreasing that would reduce the working length of the waveguide to some extent.

As the cladding material is considered lossy, a reduction in the guide separation distance, 'd', means the area where the field suffers loss is being reduced that in turns reduce the power loss of the propagating mode.

#### **Effects on Field Profile**

The presence of neighbouring guides has profound impacts not only upon the  $n_{eff}$  but also upon the field profiles of the guided modes. The field profiles of the  $H_{11}^x$  mode of a rectangular guide along the guide axis for the various guide to guide distance (Per,  $d$ ) has been presented in Fig. 4.15. It is evident from the figure that a reduction in the guide to guide distance results in a change of the field profile in the upward direction and at the outer boundary of the cladding the field value is found to be non-zero. So the neighbouring guides' presence pushes both the field value as well as the  $n_{eff}$  upward, indicating a reduction in the phase velocity of the propagating mode, especially the fundamental mode.

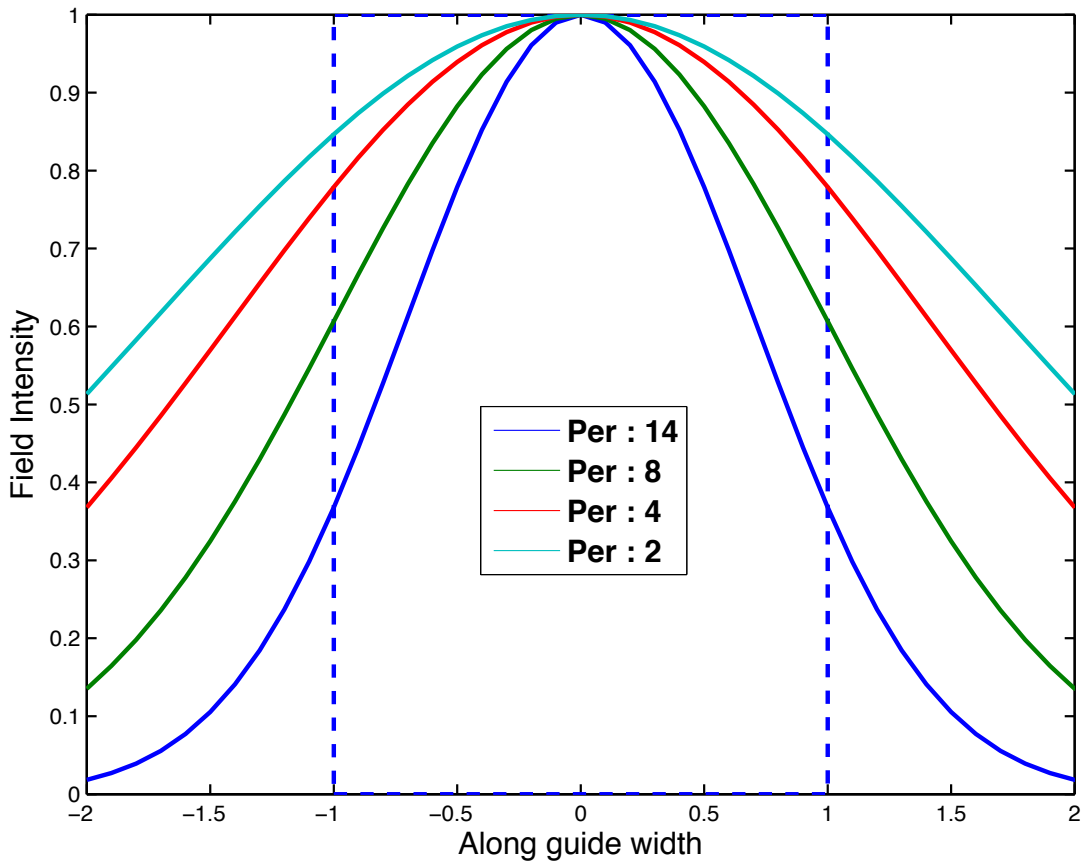


Figure 4.15: Field intensities of a Rectangular Guide along Guide axis for Different Per, d; loss-less cladding is considered

### Cutoff wavelength ( $\lambda_c$ )

Figure 4.16 shows that as we decrease the guide to guide distance the cutoff wavelength ( $\lambda_c$ ) for the second mode decreases. The implication of this result is that reducing the guide to guide distance of a waveguide array allows us a much wider frequency range to operate at the single-moded condition.

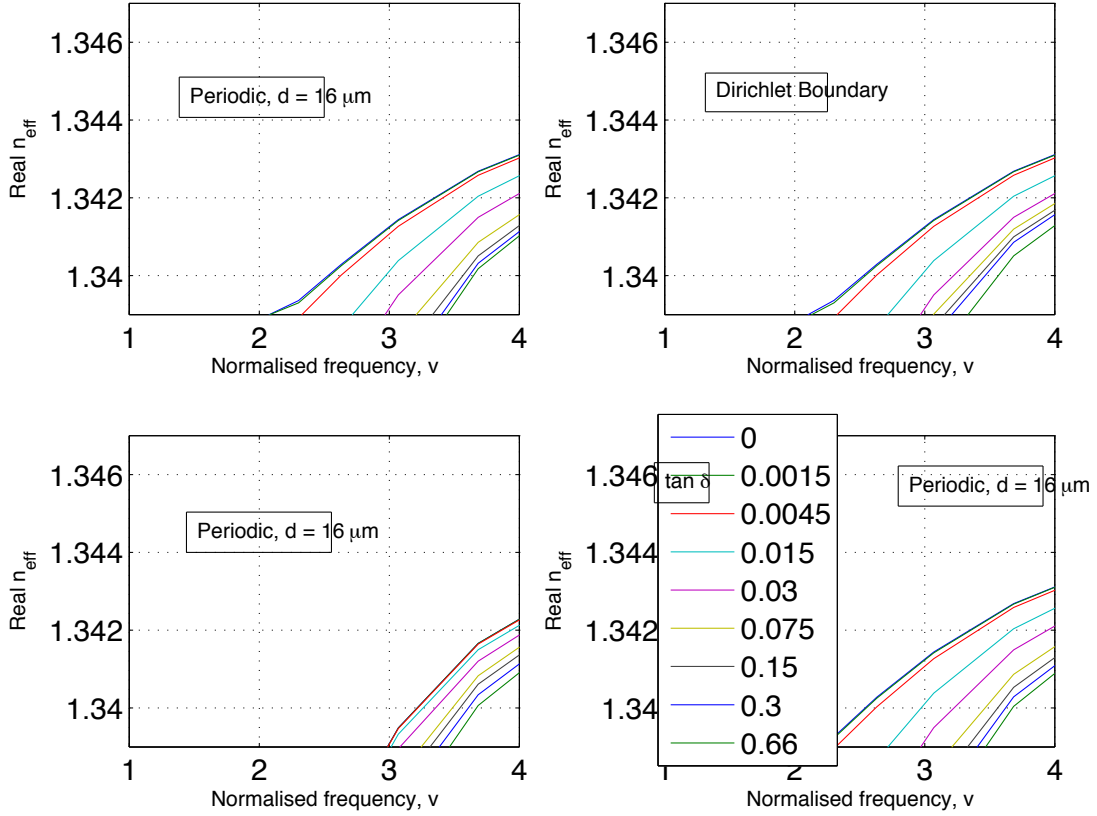


Figure 4.16: Mode 2 cutoff comparison with single guide and periodic guides with different periodicity

### Coupling Length

Figure 4.17 shows the schematics diagram of a typical directional coupler where the core materials as before have been considered lossless and the cladding material is taken as lossy. Simulations have been carried out to determine propagation characteristics to determine the Coupling Length ( $L_c$ ) defined in Eqn. 4.5 at  $\lambda = 550$  nm for various guide to guide separation  $d$ . The evaluated  $L_c$ s have been presented in Fig. 4.18. As the loss tangent ( $\tan \delta$ ) is increased, the coupling length initially decreased for a small loss values, as according to Chinni et al. [1995] for small loss values ( $\tan \delta < 10^{-4}$ ) increasing material loss decreases the coupling length, so our simulated results are in good agreement with the article. The coupling length reaches a minimum value for a particular  $\tan \delta$ , a further increase in material loss in the cladding tends to increase the  $L_c$ . A decrease in the

guide to guide distance ( $d$ ) increases the  $L_c$ . If transferring information through the waveguide at a larger distance is sought, the coupling length ( $L_c$ ) should be as high as possible to reduce signal contamination by the neighbouring guides. The use of lossy cladding material allows us to operate increase the coupling length even if we reduce the guide to guide separation to a small value.

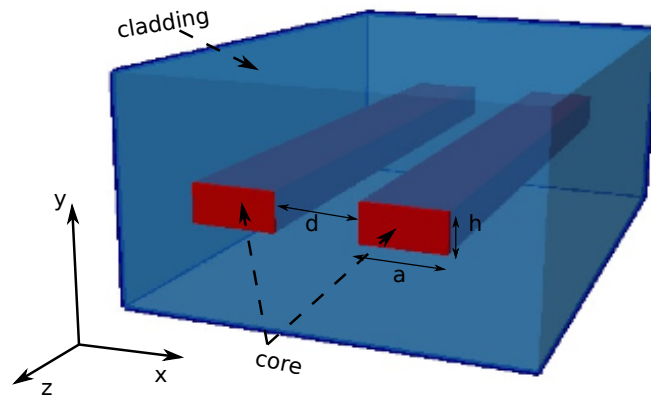


Figure 4.17: Schematics of a Directional Coupler

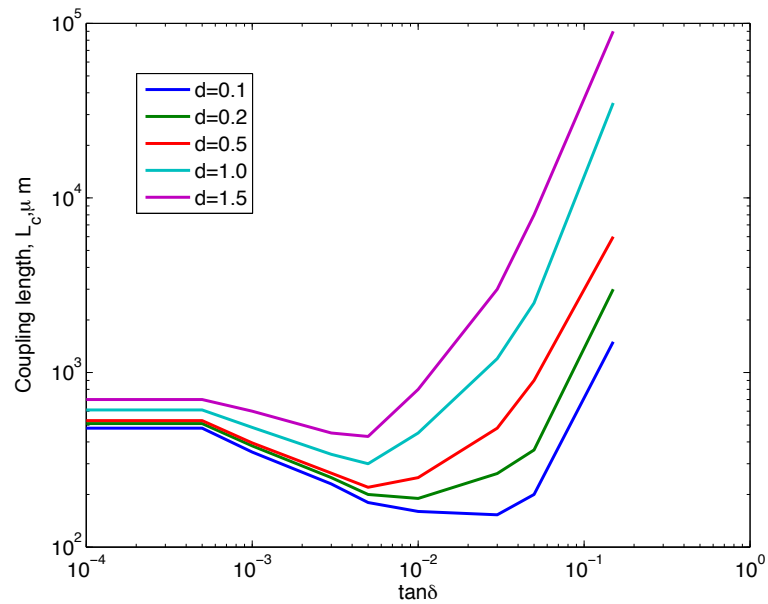


Figure 4.18: Coupling Length of a Directional Coupler with lossy cladding

---

## 4.4 Multi-layer Waveguide Structures

In Optical fibre communication dispersion plays a very crucial role as signals having multiple frequency components if passed through a dispersive fibre suffers pulse broadening that decreases the system performance Keiser [2003]. To overcome the difficulties introduced by the dispersion present in the system dispersion flattening fibres are widely being used. One of the most popular structures of fibre is the W-fibre Reeves et al. [2003] that has a special refractive index profile and a schematics diagram of such a waveguide has been presented in Fig. 4.19, where the core, inner cladding and the outer cladding have refractive indices  $n_1$ ,  $n_2$  and  $n_3$  respectively. Here  $n_1 > n_3 > n_2$  is assumed. The name of such fibres comes from the refractive index profiles, shown in Fig. 4.19, looks like capital 'W'.

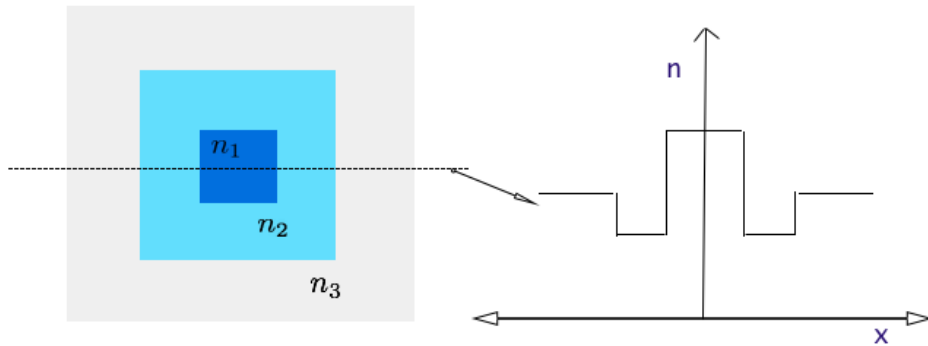


Figure 4.19: Schematics and the Refractive index ( $n$ ) profiles of a W-fibre like waveguide

The dispersion characteristics of a W-fibre like waveguide is determined numerically for various material loss values. At first a scattering boundary condition is considered at the outer border of the outer cladding, the dispersion curves for various  $\tan \delta$  is shown in Fig. 4.20. The simulation is performed over the visible spectrum and the result shows that for the higher frequencies (smaller wavelengths, bluish) the dispersion curve is flatter for the lower values of material loss. Figures 4.21 and 4.22 show the dispersion curves for 'Dirichlet' and 'Peri-

odic' boundary conditions respectively under the same parameters. The use of Dirichlet boundary condition seems to change the dispersion curve more flat at higher material loss values. Use of periodic boundary condition shows no significant improvement in flattening dispersion over the Dirichlet boundary condition. We can conclude from these results that multi-layer waveguide having W-fibre like refractive index profile helps to flatten the dispersion characteristics of such waveguides and the neighbouring guides have negligible effects on the dispersion characteristics.

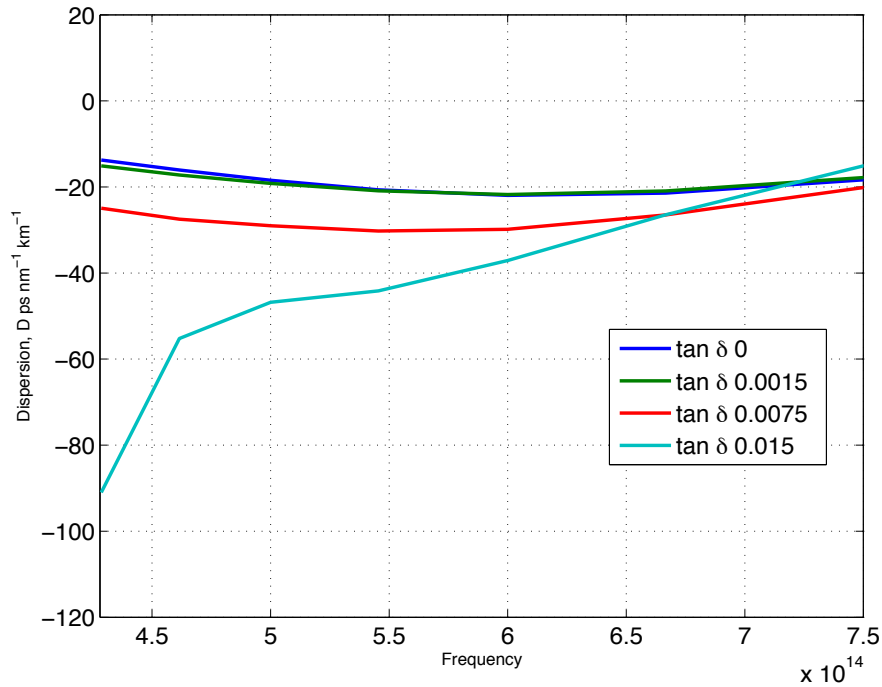


Figure 4.20: Dispersion for Circular insect ommatidium with 3 layers and scattering boundary condition

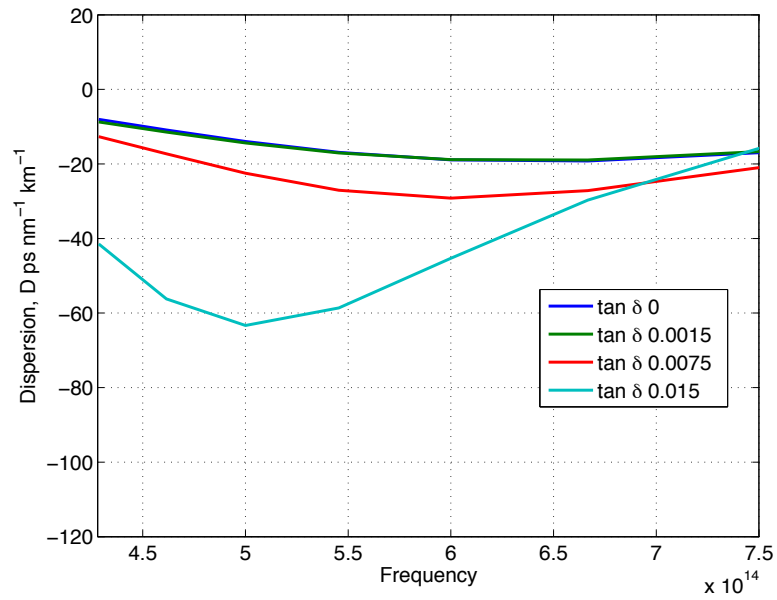


Figure 4.21: Dispersion for Circular insect ommatidium with 3 layers and Dirichlet boundary condition

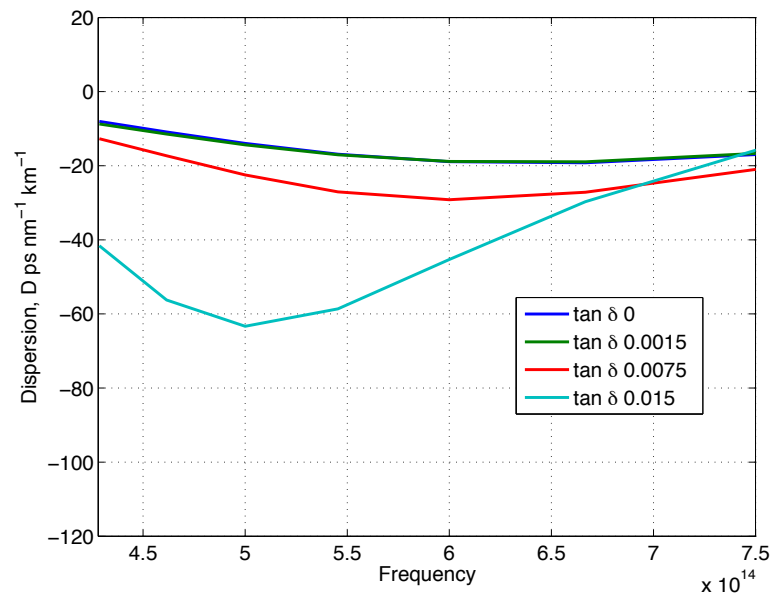


Figure 4.22: Dispersion for Circular insect ommatidium with 3 layers and Periodic boundary condition

---

## 4.5 *Drosophila Melanogaster* Ommatidium

Figure 4.23 shows the cross-section of the Ommatidium of a *Drosophila Melanogaster* Compound eye that shows the real refractive indices available in the literature for the different microstructures. The structure starts with a Cornea with refractive index  $n_{cornea} = 1.490$ . At the air-cornea interface, due to the high refractive index contrast, it is expected a strong reflection. Some external structures, however, reduce the reflection effect, in this, we are not considering the reflection management system as our principal focus is on the guiding mechanism present in the system and how the lossy materials affect the propagation characteristics through the structures. Right after the Cornea a cuticular lens is located with  $n_{lens} = 1.452$  at the beginning that gradually reduces to 1.435 at the second surface of the lens; the Lens diameter being  $\approx 15\mu$  m. A crystalline cone segment is found after the Lens having a refractive index of 1.348 that is surrounded by the long pigment cell layer ( $n = 1.311$ ). The cone segment is attached to the Lens end by an aperture having a dimension  $\approx 6\mu$  m. As the cone is surrounded by a lower index lossy material, there is little chance for the light entered from the Lens to the Cone section to leave the structure. The Lens is focusing light at the end of the cone section where the Rhabdom is located. Rhabdom has a refractive index of 1.347 that has little difference with the Cone refractive index of 1.348, indicating a tiny amount of reflection present at the Cone-Rhabdom interface. The Rhabdom has a hexagonal cross-section and is surrounded by a layer of lower refractive index (1.339) and absorbing material. The thickness of the first absorbing layer is about  $2\mu$  m. A second absorbing layer surrounds the Rhabdom and the first layer with a refractive index of 1.343 and with a thickness about  $2 - 3\mu$  m. The entire structure is then surrounded by a  $2\mu$  m thick long pigment cell layer (1.351). The finite aperture present after the Lens would produce the diffraction and the focused beam must be placed at the Rhabdom entrance. At the Rhabdom entrance, the field profile is thus the diffraction profile generated by the Lens-Aperture assembly that is shown in Fig. 4.24.

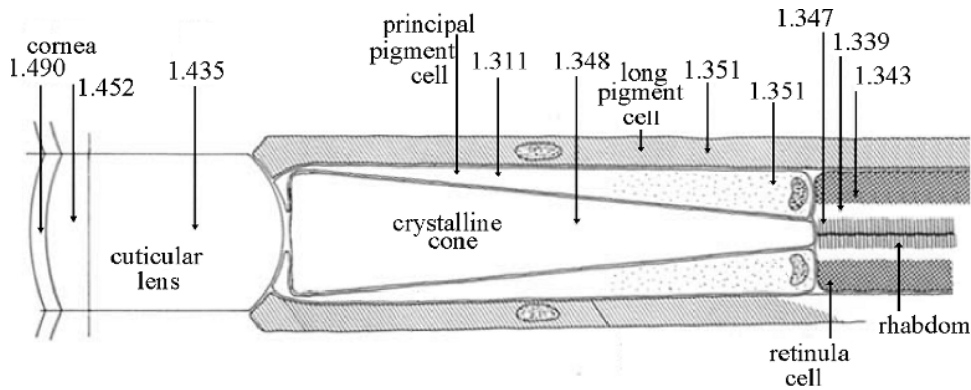


Figure 4.23: Cross section of a *Drosophila melanogaster* Ommatidium source: Photobiology

As the Rhabdom is surrounded by a lower refractive index material, it can be said in the context of the optical waveguide theory that it should act a waveguide.

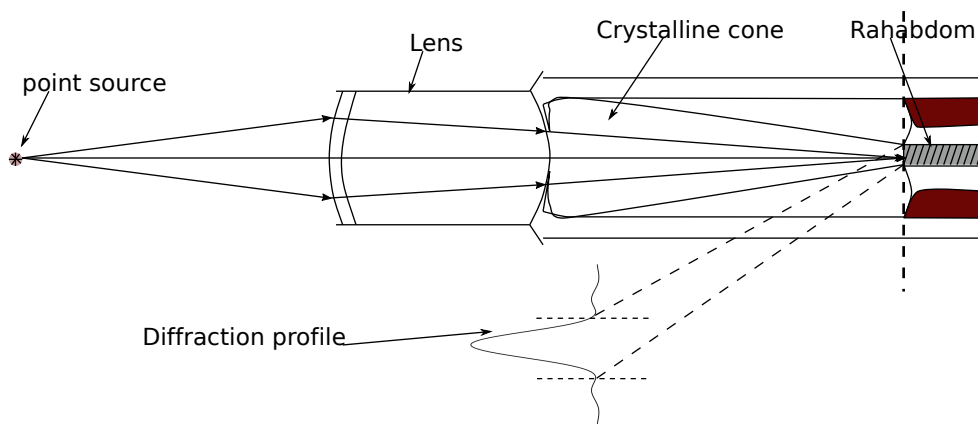


Figure 4.24: Impact of diffraction on the field profile at the Rhabdom entrance

As the surrounding materials of the guide are lossy, the modes propagated through the guide would be lossy and be reducing in magnitude as it propagated through the Rhabdom when it reached the end of the guide the remaining power would be tiny, and a small amount of reflection is expected from the end of the Rhabdom. As it propagates through the rhabdom, it is being absorbed by the Rhabdom that in results in the excitation to the photoreceptor. The exact amount of loss present in the surrounding material is not known, but an analysis

---

considering the length of the guide as  $80\mu$  m shows that if we expect no reflected power from the end, if  $-30dB$  loss over the length is considered the required value of the imaginary refractive index would be 0.005 ( $\tan \delta \approx 0.015$ ) for the wavelength  $\lambda = 400$  nm and 0.01 ( $\tan \delta \approx 0.015$ ) for  $\lambda = 800$  nm. From the propagation characteristics, it is evident that the guide remains single moded for the normalised frequency,  $v \approx 2.4$ , for a  $NA = 0.15$  and a guide dimension of  $2\mu$  m the corresponding wavelength  $\lambda = 391$  nm. For the wavelengths more than ( $\lambda > 390$  nm), this value will result in the guide to operate in single mode condition. As the visible spectrum spans the wavelength range of 390 nm-750 nm, the rhabdom as waveguide maintains the first mode for all wavelength in this range. As the angle of incidence required for the first mode with the axis of the waveguide is very small ( $\approx 5^\circ - 10^\circ$ ), only the point source present on the image directly ahead of the Ommatidium would excite the first mode in the waveguide, which would be propagated through the guide for the entire visible spectrum at ease. Any point source from which the RAY reaches the Ommatidium at a higher angle would excite the next higher order mode, would eventually be blocked by the Rhabdom waveguide. In this way, each Ommatidium transfers the information present directly ahead of it and the other surrounding points less corrupt the information as the information coming from them would try to excite the higher mode in the guide and are being blocked.

FDTD simulation has been performed on the structure of an insect ommatidium, where it is assumed that  $\Delta x = \Delta y = \Delta z = \Delta = 50$  nm and  $\Delta t = 9.62 \times 10^{-17}$  sec. is used by using equation 2.101, the operating wavelength  $\lambda = 550$  nm. It is assumed that the rhabdom has a refractive index of 1.347, the next layer has 1.339 and the third layer has 1.343. As the core (rhabdom) has a higher refractive index, it should act as a waveguide. The source is assumed to be far away from the structure, so it is assumed that the plane wave is reached as input.

Figure 4.25 shows the simulation results where it is assumed that the surrounding regions of the rhabdom are lossless. The result shows that the lens focuses the incoming waves at the rhabdom entrance but the wave is not well guided by the core, a considerable amount of power is lost to the cladding region. The power lost through the cladding region might interfere with the other

---

neighbouring guides.

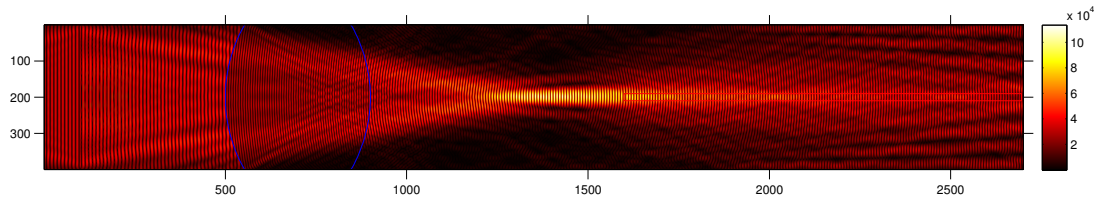


Figure 4.25: FDTD simulation of insect ommatidium, 3 layers, loss-less

Figure 4.26 shows that when the first cladding is highly lossy, the core is guiding the mode that is well confined, but dying out too soon along the core.

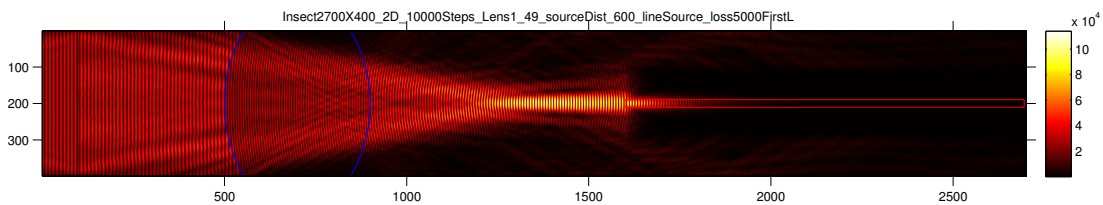


Figure 4.26: FDTD simulation of insect ommatidium, 3 layers, conductivity  $\sigma = 5000$  for the first cladding, the second cladding is loss-less

Figure 4.27 shows that when the second layer is considered highly lossy and the first layer is loss-less, the mode is guided by the core and the chances of interference to the neighbouring guide is lower than the loss-less case.

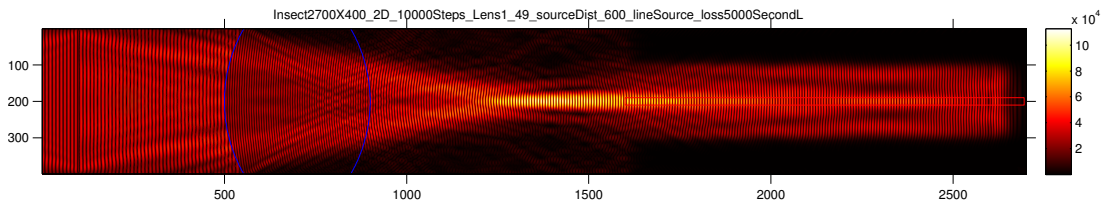


Figure 4.27: FDTD simulation of insect ommatidium, 3 layers, conductivity  $\sigma = 0$  for the first cladding,  $\sigma = 5000$  for the second cladding

Figure 4.28 shows that when a lower value of the loss is considered for the first layer and a higher value of the loss is envisaged for the second layer, the mode is well guided as well as well confined within the core.

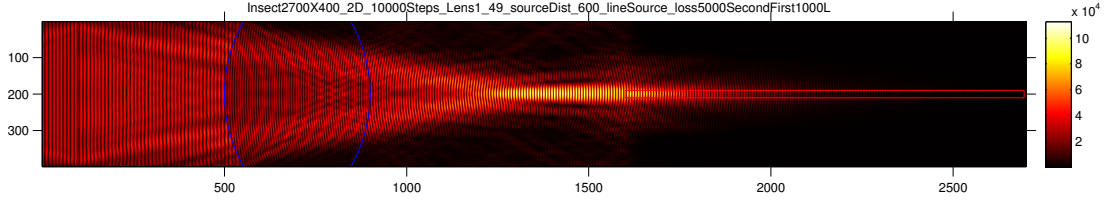


Figure 4.28: FDTD simulation of insect ommatidium, 3 layers, loss-less

The surrounding material of the Rhabdom is lossy, in light of our previous results we know that for a guide with lossy surroundings supports the fundamental mode having a pattern very similar to the diffraction pattern produced by the finite aperture, and if the same trend is projected at the Rhabdom entrance that would be guided by it without suffering any coupling and insertion loss. The finite aperture of the Lens-Pupil assembly present at the beginning of the Ommatidium is producing a field pattern at the Rhabdom entrance, which is the field pattern of the supported mode of the Rhabdom. The lossy surrounding is increasing the field confinement within the Rhabdom that might be helping to reduce the coupling between the surrounding other Ommatidium units. The lossy surrounding is thus playing a dual role in the performance of the waveguide firstly by moving the cutoff wavelength ( $\lambda_c$ ) to make the entire visible spectrum single moded and secondly by increasing the field confinement factor thereby reducing the interactions between the neighbouring guides. Wavelength  $\lambda < 390$  nm are considered as ultraviolet light, and the propagation characteristics suggests that at this region of the spectrum the guide would support the first as well as the second mode, indicating that each Rhabdom at these wavelengths would carry information not only about the point directly ahead of it but also some pieces of information from the surrounding points in the image plane as well. Operating in ultraviolet light would thus result in a slightly blurred vision. Theoretically, the Rhabdom should support the fundamental mode even at wavelength  $\lambda > 750$  nm or the IR spectrum, the field confinement factor becomes too small making the spot size of the supported mode too large compared to the waveguide dimension. At that case, the propagated mode would interfere with the other surrounding guides making a possible blurred vision. In a hexagonal arrangement, each waveguide (Rhabdom) is surrounded by six other neighbouring similar waveguides. As

we have shown that the presence of the surrounding guides increases the gap between the first mode with the second mode, the hexagonal guide array is thus making the single-moded operating range stronger. However, as we can see that the cutoff frequency is increased, means that the  $\lambda_c$  is decreased, we can conclude that the presence of the other surrounding guides makes the Rhabdom operate as single moded even in the Ultraviolet spectrum. It has been reported that some insect might see the ultraviolet frequencies, our result, strongly supports this claim. The waveguide (Rhabdom) is seemingly operating for a very wide frequency range (near ultraviolet - 750nm) and the waveguide array is acting as a communication channel, the waveguide dispersion is potentially affecting the operation. As we have shown before that the 3-layer W-fibre like structure flattens the dispersion characteristics of such guides. The Rhabdom, first absorbing layer and the second absorbing layer of the Ommatidium have refractive indices of 1.347, 1.339 and 1.343 respectively, indicating that the structure resemblance that of the W-fibre refractive index profile, thereby might be reducing the dispersion characteristics of the waveguide system significantly. Figure 4.29 shows a

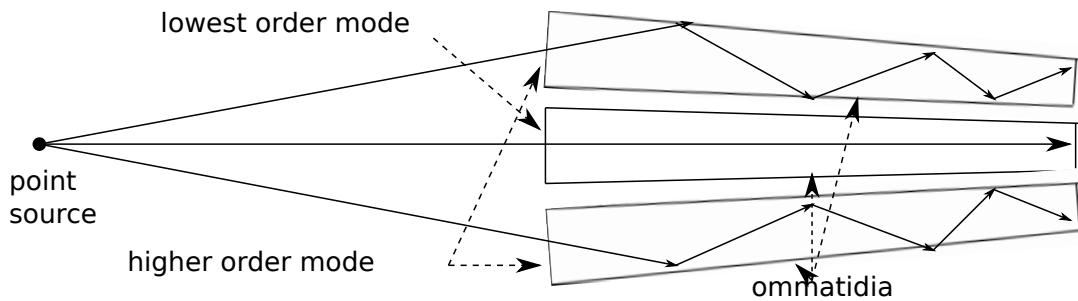


Figure 4.29: Schematics of the position of the point source and the excited modes in rhabdom of compound insect eye

schematics diagram of the relative position of the ommatidia units with respect to a point source located at a distance. The information from the point source reaches the Ommatidium entrance that is located straight ahead of it that makes a tiny angle with the waveguide axis; this would excite the fundamental mode in the core, and would be guided and absorbed by the photoreceptors, to produce visual stimuli. The information from the same point source reaches the other neighbouring Ommatidia, would excite the higher order modes in the code; in

the visible spectrum the core supports only the first mode, thereby the mode would eventually be radiated to the cladding region to be absorbed. It can be concluded that this way, each Ommatidium unit contributes to the visual stimuli that are coming straight ahead of it and discarding the information from the other neighbouring point sources.

## 4.6 Glial Cells of Human Retina

Figure 4.30 shows a typical Muller Glial cell of Human retina. Quantitative phase microscopy on enzymatically dissociated retinal neurons revealed a refractive index of 1.35 - 1.36 which is very close to earlier estimates for the retinal tissue ( $n \approx 1.36$ ) (Figure 4.30; Nordenson [1934]; Franze et al. [2007]). It should be noted that these values were measured on the somata of the neurones, i.e. the subcellular part with the densest architecture. Surprisingly, the refractive index of both Muller cell processes was shown to be significantly higher (1.376 - 1.380) and corresponds very well to that of light guiding photoreceptor outer segments ( $n \approx 1.40$ ; Sidman [1957]).

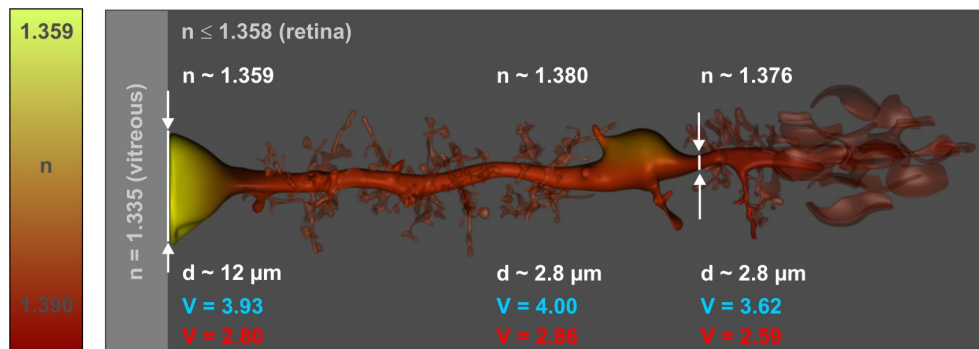


Figure 4.30: Muller Glial cell of Human retina source: Franze et al. [2007]

Besides, an observed decrease in the index of refraction towards the end foot region ( $n \approx 1.359$ ) was believed to reduce the reflection at the border to the low refractive vitreous ( $n \approx 1.335$ ). Guidance of light is not only dependent on the refractive index difference between the structure and its surrounding but also on the objects diameter and the wavelength or the normalised frequency,  $V$ . Despite

---

the complex morphology of Muller cells, the V-parameter, i.e. the light guiding capability, remains nearly constant along the entire length of the cell body.

As along the Glial cell the V-parameter (normalised frequency) is fairly constant over the entire visible spectrum and for the higher wavelengths (RED light) the V parameter is  $\approx 2.8$  that is slightly above the first mode cutoff of 2.405, indicates that at that wavelength the fundamental mode is being guided properly but along with that a fraction of the second mode should propagate as well. The required V parameters for allowing the third mode be 5.4 indicates that even at the BLUE end of the spectrum where the V-parameter is  $\approx 4.0$ , the guide would not support the third mode.

As discussed before that the light falls on the Retina surface is being guided by the Glial cell, reaches the photoreceptors located at the back of the retinal layers; the photoreceptors then absorb the light and the photocurrent is being produced; the photocurrent is then traveled in the upward direction through the bipolar, amacrine and horizontal cells to reach the Ganglion cell; Ganglion cells then transfers the collected information through the optic nerve to the brain. It indicates that the surrounding layers of the Glial cell are conductive and thus behave as lossy material for light. As the field profile of the modes supported by a waveguide surrounded by lossy material resemblance that of the field patterns generated by a finite aperture, to project the correct field profile at the guide entrance the presence of the finite aperture is necessary. The finite aperture, in this case, is the pupil of the human eye, which is considered to be a disadvantage as it limits the lowest resolution achievable by the system, but the system has exploited this phenomenon in its favour by introducing loss at the guide surrounding making the coupling between the diffraction pattern and the supported mode similar. Like the Rhabdom of insect Ommatidium, the Glial cells are embedded into a 3D Glial cell array. The presence of the other surrounding Glial cells might be affecting the propagation characteristics of the Glial cell by making the separation between the modes larger. We can conclude that unlike the Rhabdom of the insect Ommatidium, the Glial cells support up to the second mode indicate that in the human eye, each photoreceptor is not transferring the information only from the point directly ahead of it, but also some information from the surrounding points of the image plane.

---

## 4.7 Stiles-Crawford Effect

Stiles-Crawford (SC) effect refers to the directional sensitivity of the Cone photoreceptors of the Human eye. Since its discovery in 1933 by [Stiles and Crawford \[1933\]](#) several experimental verifications by numerous scientists over several decades have been performed. Despite being attempted by numerous studies [Snyder and Pask \[1973\]](#), [Moon and Spencer \[1944\]](#), [Gao et al. \[2008\]](#), [Atchison and Scott \[2002\]](#), a complete explanation of the effect is still not available in the literature. Recently in 2008 75th anniversary [Enoch and Lakshminarayanan \[2009\]](#) of the effect was observed. There are two types of SC effect, Stiles-Crawford effect of First kind (SC-1) and Stiles-Crawford effect of Second kind (SC-2). In this study, we shall try to explain the SC effect in the light of the results obtained from the combined Diffraction integral, FDTD and modal analysis.

### SC 1

The Stiles-Crawford effect of First kind is defined as follows,

“ Same intensity excitation of the same wavelength enters through the side of the aperture has less impact than the excitation enters through the centre of the aperture”

The light excitation that enters through the centre excites the fundamental mode that is more confined in the core and guided properly by the Glial cell of Human Retina and reaches the photoreceptors (Cone) present at the back of the Retinal layers. As the fundamental mode is more confined within the waveguide, more power is being carried by it, so the cone photoreceptor’s received power is more. As the first mode is well confined within the Glial cell, and the surrounding lossy material improves the confinement factor to some extent, the mode has subtle coupling effects with the surrounding other guides. Light entering through the edge of the pupil falls at the Glial cell entrance makes a higher incident angle, the excited mode is most likely be a higher order one. As the higher order mode has lower  $n_{eff}$ , as a results less confined than the first mode, is more likely to interact with the surrounding guides and would carry less power. The cone photoreceptor that receives power from a higher order mode would receive less

---

power as a consequence.

## **SC 2**

The Stiles-Crawford effect of Second kind is defined as follows,

”The observed colour of a monochromatic light entering the eye near the edge of the pupil is different compared to that for the same wavelength light entering near the centre of the pupil, regardless of the overall intensities of the two light”

Let us assume a monochromatic green light ray has entered through the edge of the pupil. On reaching the Glial cell entrance, it would be incident at an angle as a consequence would most likely excite a higher order mode. The higher order mode guided by the Glial cell would be less confined and would interact with the surrounding guides much more than the first mode would. At the end of the Glial cell, let us assume we have three Cone photoreceptors being sensitive to three colours RED, GREEN and BLUE. Blue light guided by the first mode would excite the BLUE cone more than the other two cone types; as a result, the perceived colour would have been BLUE. However, the Blue light guided as the second or higher order mode would enter at an angle to all three types of cone photoreceptors and would produce excitations not only in the BLUE cone but also in the other two types. As a consequence, the mixed responses from the three cone types would produce a perceived colour that would not be a perfect BLUE.

## **4.8 Summary**

This Chapter presents the results obtained for the waveguide structures studied in this thesis. Propagation characteristics of a planar waveguide considering lossy cladding are presented at the beginning. Impacts of the losses on the various aspects of the propagation characteristics have been discussed after that. Waveguides with 3D geometry are analysed then. Impacts of the presence of the neighbouring guides and 3-layer waveguide structure on the propagation characteristics have been discussed after that. The results obtained from the previous sections is applied to discuss the propagation characteristics of the Ommatid-

---

ium of insect Compound eye and the Glial cell of Mammal retina. An explanation of the Stiles-Crawford effect of Human retina is given at the end of this Chapter. This Chapter thus presents the key results and discusses the implications of the results.

# Chapter 5

## Conclusions

The primary objective of this thesis has been to analyse biological optical waveguides in optical frequencies incorporating various practical aspects present in the biological tissues such as lossy material, the presence of neighbouring waveguides, multi-layers structure and the impacts of finite apertures present in visual systems. The objective outlined at the beginning of the thesis has been achieved through detailed analysis throughout the thesis. As an analysis tool **H**-field based full vectorial finite element methods has been used in modal analysis, Finite Difference Time Domain (FDTD) has been used to investigate the time evolution of the signals through the structures under considerations and Rayleigh-Sommerfeld (RS) diffraction integral has been used to study the impacts of finite aperture on the field profile reached the waveguide entrance.

Chapter 1 shows that the assumption that the Rhabdom of insect ommatidium and the Glial cells of Human retina works as an optical waveguide and their surrounding materials are lossy at optical frequencies. The cross-section of these waveguides are found to be hexagonal or can be considered as a hexagon with some random variations.

In Chapter 2 comprehensive descriptions of the computational tools used in this study are provided. A detailed analysis of the development of the FEM method has been presented and the various technical aspects of implementing the method, such as discretization, shape function, boundary conditions, element and global matrices formulation, have also been presented in this Chapter. A comprehensive description of the FDTD algorithm and its various technical aspects

---

have been present in this Chapter. A brief description of the Diffraction integrals used in this work has been provided this Chapter as well.

As for the planar waveguide structure the analytical solution can be determined, in Chapter 3 an analytic solution for the planar waveguide has been derived as a solution of the Maxwell's equations. The analytic solution thus obtained is then used to benchmark the results found from the numerical simulations and it has been found that both the results matches with reasonable accuracies. It has been shown that there is a relationship between the angle between the power flow direction (Poynting vector) with the waveguide axis and the order of the propagating mode; the higher order mode makes more angle with the waveguide axis. So if the waveguide core receives power at an angle, depending upon the angle, the corresponding mode is excited within the core and being guided by it. The FDTD simulations have verified this phenomenon of angle dependence of the excited mode.

As one of the prime objectives of the study is to analyse the impacts of the material loss on the propagation characteristics of the biological optical waveguide where some exhibit material loss in optical frequencies, a theoretical derivation on the planar waveguide has been carried out. It has been found that as we increase the material loss in the cladding the analytic solution indicates that the field confinement increases, and the field profile shows a fluctuating behaviour that can be regarded as an exponentially varying sinusoidal variation. This field shape has paramount consequences in the analysis and the functionalities of the waveguides with lossy cladding that has been shown in the later parts of this work. Numerical simulations by modal analysis and FDTD confirms the fact that the field confinement increases as we increase the material loss in the cladding.

It has been found that the waveguide loss increases with increase in material loss ( $\tan \delta$ ) in the cladding, but the waveguide loss reaches a maximum value, further increase in  $\tan \delta$  results in a decrease in the waveguide loss. The fascinating finding is that the material loss present in the cladding material of the biological optical waveguide is present there on purpose, it is making the field more confined within the core and manages to keep the waveguide loss within a reasonable limit.

It has been shown that if we can launch a field profile that matches one of

---

the supported modes of the waveguide, that propagates through the waveguide unperturbed if the material is lossless; for a lossy cladding the shape of the modal field profiles remains unchanged although it loses power as it propagates through the waveguide.

It has been shown that when light passes through a finite aperture, it experiences diffraction, as a consequence on a screen a point source projects a diffraction pattern that resembles the field profile required for a waveguide with lossy cladding. The finite dimension of the Lens present at the beginning of the Ommatidium of insect Compound eye produces a diffraction pattern that is the field pattern required by the Rhabdom that has lossy surrounding material; so the projected field is propagated through the Rhabdom without experiencing much insertion loss. In the case of Human retina, the finite aperture of the pupil serves as the aperture that projects the diffraction pattern at the Glial cell entrance on the top retinal layer and the field profile matches with the field profile of the supported mode. It can be concluded that Nature has introduced the optical waveguides with lossy cladding that deals with the physical constraints of diffraction.

The results obtained from a planar waveguide can be used to get the propagation characteristics of the Rectangular waveguides when the modes are not near the mode cut-off. The results obtained for the planar waveguide can be extended to use for the rectangular waveguide. As the analytic solution of the waveguide with 2D cross-section is difficult, in some cases impossible, to obtain, we have to rely on the numerical solutions. The numerical simulations on Rectangular waveguide confirm that the fact that the field has a fluctuating pattern, confinement increases, and waveguide loss decreases beyond a certain point is valid for this case as well. As the waveguide under considerations has a hexagonal cross-section, in reality irregular in shape that can be approximated by hexagons, it is required to perform the analysis on an irregular structure. However, dealing with hexagonal or irregular structure is technically difficult, where dealing with Rectangular structure is much easier. Some analysis of the mode profiles of waveguides with Rectangular, Circular, Hexagonal, Elliptic and irregular with similar dimensions and material profiles have been carried out that shows that the mode profiles of the first two lowest order modes for all of them are similar.

---

That is why in most of the analysis, a waveguide with rectangular cross-section has been used. The hexagonal shape shows that it must be polarisation sensitive, and it has been reported that some of the insect eyes might be polarisation sensitive.

It has been found that the average refractive indices of biological materials in optical frequencies lies between 1.33 - 1.38, and the numerical aperture (NA) for the biological optical waveguides to be  $\approx 0.15$ . Under these conditions, the optimum waveguide width is  $\approx 2 \mu m$ , and interesting point to note that insect Rhabdom has an approximate diameter of  $2 \mu m$  and the Glial cell's average diameter is  $2.4 \mu m$ . In optical frequencies smaller than  $1 \mu m$  dimension waveguide would suffer severe waveguide loss.

It has been found that the increase in  $\tan \delta$  of the cladding material has positive impacts on the dispersion characteristics of biological optical waveguides. Increased  $\tan \delta$  flattens out the dispersion characteristics that indicates these waveguides can operate in a broad spectrum of frequencies in the presence of material loss.

It has been found that the higher  $\tan \delta$  allows a waveguide to operate under the single-moded condition for smaller wavelengths. This result indicates that the waveguides with lossy cladding increase its single mode operating range.

It has been found that the presence of the neighbouring guides widens the gap between the first mode and second mode, thereby increases the single mode operating wavelength range. The 3-layer (1.347-1.339-1.343) structure present in the insect Ommatidium is found to improve the dispersion characteristics of the waveguide.

Stiles-Crawford effect of Human Retina refers to the directional sensitivity of the cone photoreceptors and it has been found that these sensitivities can be explained in light of the results found from modal analysis and Diffraction Integrals.

In summary the loss present in the surrounding materials of biological optical waveguide increases the single mode operating wavelength range and makes these waveguides single-moded over the visible frequencies, increases the field confinement within the core in turn decreases the interference with the neighbouring guide, the presence of the neighbouring guides improves the single mode oper-

---

ating condition, and the 3-layer structure in insect ommatidium improves the dispersion characteristics.

## **5.1 Future works**

In this thesis, the impacts of scattering by the biological tissues on the propagation characteristics have been ignored. Future study can be carried out to determine the effects of scattering on the behaviour of these biological waveguides. It has been found that the Glial cell with its lossy surrounding acts as an optical waveguide, and the guided mode by the Glial cell has to be absorbed by the Rod and Cone Photoreceptors present at the back of the Mammal retina. Previous studies showed that the photoreceptors have waveguide properties in the optical frequencies. It would be interesting to explore the coupling between the Glial cells and the Photoreceptors that would require junction analysis, and this study has the potential to explain the Stiles-Crawford effect in greater details.

# References

- A Peyman, S Holden, C. G. (2000). measurement of the Dielectric Properties of Tissues at Microwave Frequencies.
- Atchison, D. A. and Scott, D. H. (2002). Contrast sensitivity and the stiles-crawford effect. *Vision research*, 42(12):1559–1569.
- Baker, O. (2010). Eye cells as light pipes. *Phys. Rev. Focus*, 25:15.
- Balanis, C. A. (1989). *Advanced engineering electromagnetics*, volume 20. Wiley New York.
- Bass, M., Van Stryland, E. W., Williams, D. R., and Wolfe, W. L. (2001). *Handbook of optics*, volume 2. McGraw-Hill.
- Bauer, L. and Reiss, E. L. (1978). Cutoff wavenumbers and modes of hexagonal waveguides. *SIAM Journal on Applied Mathematics*, 35(3):508–514.
- Berenger, J.-P. (1994). A perfectly matched layer for the absorption of electromagnetic waves. *Journal of computational physics*, 114(2):185–200.
- Biernson, G. and Kinsley, D. (1965). Generalized plots of mode patterns in a cylindrical dielectric waveguide applied to retinal cones. *Microwave Theory and Techniques, IEEE Transactions on*, 13(3):345–356.
- Buah, P., Rahman, B., and Grattan, K. (1997). Numerical study of soliton switching in active three-core nonlinear fiber couplers. *Quantum Electronics, IEEE Journal of*, 33(5):874–878.

## REFERENCES

---

- Burkardt, J. (2011). Distmesh: A simple mesh generator in matlab.
- Cangellaris, A. C., Lin, C., and Mei, K. K. (1987). Point-matched time domain finite element methods for electromagnetic radiation and scattering. *Antennas and Propagation, IEEE Transactions on*, 35(10):1160–1173.
- Chiang, K. (1994). Review of numerical and approximate methods for the modal analysis of general optical dielectric waveguides. *Optical and Quantum Electronics*, 26(3):S113–S134.
- Chinni, V., Huang, T., Wai, P., Menyuk, C., and Simonis, G. (1995). Crosstalk in a lossy directional coupler switch. *Lightwave Technology, Journal of*, 13(7):1530–1535.
- Cole, K. S. and Cole, R. H. (1941). Dispersion and absorption in dielectrics i. alternating current characteristics. *The Journal of Chemical Physics*, 9(4):341–351.
- Enoch, J. M. and Lakshminarayanan, V. (2009). 75th anniversary of the stiles–crawford effect (s): a celebratory special symposium: October 23 2008, rochester, new york. *Journal of Modern Optics*, 56(20):2164–2175.
- Feit, M. and Fleck, J. (1980). Computation of mode properties in optical fiber waveguides by a propagating beam method. *Applied Optics*, 19(7):1154–1164.
- Feliziani, M. and Maradei, E. (1994). Point matched finite element-time domain method using vector elements. *IEEE transactions on magnetics*, 30(5):3184–3187.
- Franze, K., Grosche, J., Skatchkov, S. N., Schinkinger, S., Foja, C., Schild, D., Uckermann, O., Travis, K., Reichenbach, A., and Guck, J. (2007). Müller cells are living optical fibers in the vertebrate retina. *Proceedings of the National Academy of Sciences*, 104(20):8287–8292.
- Gao, W., Cense, B., Zhang, Y., Jonnal, R. S., and Miller, D. T. (2008). Measuring retinal contributions to the optical stiles-crawford effect with optical coherence tomography. *Optics express*, 16(9):6486–6501.

## REFERENCES

---

- Gedney, S. D. and Navsariwala, U. (1995). An unconditionally stable finite element time-domain solution of the vector wave equation. *Microwave and Guided Wave Letters, IEEE*, 5(10):332–334.
- Goell, J. (1969). A circular-harmonic computer analysis of rectangular dielectric waveguides. *Bell Syst. Tech. J*, 48(7):2133–2160.
- Hayata, K., Koshiba, M., Eguchi, M., and Suzuki, M. (1986). Vectorial finite-element method without any spurious solutions for dielectric waveguiding problems using transverse magnetic-field component. *Microwave Theory and Techniques, IEEE Transactions on*, 34(11):1120–1124.
- Hesthaven, J. and T, W. (2001). High-order/spectral methods of unstructured grids i. time-domain solution of maxwell’s equations.
- Ishimaru, A. (1977). Theory and application of wave propagation and scattering in random media. *Proceedings of the IEEE*, 65(7):1030–1061.
- Johnson, C. C. and Guy, A. W. (1972). Nonionizing electromagnetic wave effects in biological materials and systems. *Proceedings of the IEEE*, 60(6):692–718.
- Katz, B. and Minke, B. (2009). Drosophila photoreceptors and signaling mechanisms.
- Keiser, G. (2003). *Optical fiber communications*. Wiley Online Library.
- Koshiba, M., Tsuji, Y., and Hikari, M. (2000). Time-domain beam propagation method and its application to photonic crystal circuits. *Journal of Lightwave Technology*, 18(1):102.
- Labin, A. and Ribak, E. (2010). Retinal glial cells enhance human vision acuity. *Physical review letters*, 104(15):158102.
- Land, M. F. (1997). Visual acuity in insects. *Annual review of entomology*, 42(1):147–177.
- Lax, M., Louisell, W. H., and McKnight, W. B. (1975). From maxwell to paraxial wave optics. *Physical Review A*, 11(4):1365.

## REFERENCES

---

- Lee, J.-F., Lee, R., and Cangellaris, A. (1997). Time-domain finite-element methods. *IEEE transactions on antennas and propagation*, 45(3):430–442.
- Mabaya, N., Lagasse, P., and Vandebulcke, P. (1981). Finite element analysis of optical waveguides. *IEEE Transactions on Microwave Theory Techniques*, 29:600–605.
- Manakov, S. (1973). Nonlinear fraunhofer diffraction. *Zh. Eksp. Teor. Fiz*, 65(4):10.
- Marcatili, E. A. (1969). Dielectric rectangular waveguide and directional coupler for integrated optics. *Bell System Technical Journal*, 48(7):2071–2102.
- Marchand, E. and Wolf, E. (1966). Consistent formulation of kirchhoff’s diffraction theory. *JOSA*, 56(12):1712–1721.
- Mendlovic, D., Zalevsky, Z., and Konforti, N. (1997). Computation considerations and fast algorithms for calculating the diffraction integral. *Journal of Modern Optics*, 44(2):407–414.
- Moon, P. and Spencer, D. E. (1944). On the stiles-crawford effect. *J. Opt. Soc. Am*, 34(6):319–329.
- Müller, K. (1851). *Synopsis muscorum frondosorum omnium hucusque cognitorum*, volume 1. sumptibus A. Foerstner.
- Mur, G. (1981). Absorbing boundary conditions for the finite-difference approximation of the time-domain electromagnetic-field equations. *Electromagnetic Compatibility, IEEE Transactions on*, (4):377–382.
- Nagashima, T., Taru, T., and Sasaki, T. (2013). Multi-core optical fibre. US Patent 8,433,166.
- Navarro, R. (2009). The optical design of the human eye: a critical review. *Journal of Optometry*, 2(1):3 – 18.
- Navarro, R., Méndez-Morales, J., and Santamaría, J. (1986). Optical quality of the eye lens surfaces from roughness and diffusion measurements. *JOSA A*, 3(2):228–234.

## REFERENCES

---

- Neumann, T. R. (2002). Modeling insect compound eyes: Space-variant spherical vision. In *Biologically Motivated Computer Vision*, pages 360–367. Springer.
- Ng, E. and Ooi, E.-H. (2006). Fem simulation of the eye structure with bioheat analysis. *Computer methods and programs in biomedicine*, 82(3):268–276.
- Nolting, H.-P. and März, R. (1995). Results of benchmark tests for different numerical bpm algorithms. *Journal of lightwave technology*, 13(2):216–224.
- Nordenson, J. (1934). Ophthalmology. *OPHTHALMOLOGY*.
- Osterberg, H. and Smith, L. W. (1961). Closed solutions of rayleigh’s diffraction integral for axial points. *JOSA*, 51(10):1050–1054.
- Papas, C. H. (2014). *Theory of electromagnetic wave propagation*. Courier Corporation.
- Rahman, A. and Agrawal, A. (2013). *Finite Element Modeling Methods for Photonics*. Artech House, Incorporated.
- Rahman, B. A., Fernandez, F. A., and Davies, J. B. (1991). Review of finite element methods for microwave and optical waveguides. In *IEEE Proceedings*, volume 79, pages 1442–1448.
- Rahman, B. M. A. and Davies, J. (1984). Finite-element solution of integrated optical waveguides. *Lightwave Technology, Journal of*, 2(5):682–688.
- Raiyan Kabir, S. M., Rahman, B., Agrawal, A., and Grattan, K. T. V. (2013). Elimination of numerical dispersion from electromagnetic time domain analysis by using resource efficient finite element technique. *Progress In Electromagnetics Research*, 137:487–512.
- Ramo, S., Whinnery, J. R., and Van Duzer, T. (2008). *Fields and waves in communication electronics*. John Wiley & Sons.
- Reeves, W., Skryabin, D. V., Biancalana, F., Knight, J. C., Russell, P. S. J., Omenetto, F., Efimov, A., and Taylor, A. (2003). Transformation and control of ultra-short pulses in dispersion-engineered photonic crystal fibres. *Nature*, 424(6948):511–515.

## REFERENCES

---

- Reichenbach, A., Savvinov, A., Wurm, A., Grosche, J., Guck, J., Franze, K., Skatchkov, S. N., Agte, S., and Junek, S. (2012). *Live cells as optical fibers in the vertebrate retina*. INTECH Open Access Publisher.
- Sebbah, P. (2012). *Waves and imaging through complex media*. Springer Science & Business Media.
- Senior, J. M. (1992). *Optical fiber communications: principles and practice*, volume 2. Prentice Hall UK.
- Senior, J. M. and Jamro, M. Y. (2009). *Optical fiber communications: principles and practice*. Pearson Education.
- Sidman, R. L. (1957). The structure and concentration of solids in photoreceptor cells studied by refractometry and interference microscopy. *The Journal of biophysical and biochemical cytology*, 3(1):15–30.
- Silvester, P. (1969). Finite element solution of homogeneous waveguide problems. *Alta Frequenza*, 38:313–317.
- Smith, K. (2013). *The science of photobiology*. Springer Science & Business Media.
- Snyder, A. W. and Pask, C. (1973). The stiles-crawford effect—explanation and consequences. *Vision research*, 13(6):1115–1137.
- Songoro, H., Vogel, M., and Cendes, Z. (2010). Keeping time with maxwell’s equations. *Microwave Magazine, IEEE*, 11(2):42–49.
- Stavenga, D. (1975). Waveguide modes and refractive index in photoreceptors of invertebrates. *Vision research*, 15(3):323–330.
- Stiles, W. and Crawford, B. (1933). The luminous efficiency of rays entering the eye pupil at different points. *Proceedings of the Royal Society of London. Series B, Containing Papers of a Biological Character*, pages 428–450.
- Taflove, A. and Hagness, S. C. (2005). *Computational electrodynamics: the finite-difference time-domain method*. Artech House, Norwood, 3rd edition.

## REFERENCES

---

- Talu, S. (2011). Mathematical models of human retina. *Oftalmologia*, 55:74–81.
- Yariv, A. (1973). Coupled-mode theory for guided-wave optics. *Quantum Electronics, IEEE Journal of*, 9(9):919–933.
- Yee, K. S. et al. (1966). Numerical solution of initial boundary value problems involving maxwell’s equations in isotropic media. *IEEE Trans. Antennas Propag*, 14(3):302–307.
- Yeh, C. and Shimabukuro, F. (2008). Circular dielectric waveguides. *The Essence of Dielectric Waveguides*, pages 137–178.
- Yevick, D. and Hermansson, B. (1989). New formulations of the matrix beam propagation method: application to rib waveguides. *Quantum Electronics, IEEE Journal of*, 25(2):221–229.